รายงานวิจัยฉบับสมบูรณ์

โครงการ ความสามารถในการโพลาไรซ์และเมตริกซ์เอลิเมนต์ของแคลเซียมและอิเทอเบี่ยมไอออน

โดย อ. ดร. จิรกานต์ นันแก้ว
มหาวิทยาลัยเชียงใหม่

1 มิถุนายน 2558

สัญญาเลขที่ MRG5680117

รายงานวิจัยฉบับสมบูรณ์

โครงการ ความสามารถในการโพลาไรซ์และเมตริกซ์เอลิเมนต์ของแคลเซียมและอิเทอเบี่ยมไอออน

อ. ดร. จิรกานต์ นันแก้ว มหาวิทยาลัยเชียงใหม่

สนับสนุนโดยสำนักงานกองทุนสนับสนุนการวิจัย

Abstract

Project Code : MRG5680117

Project Title : Polarizabilities and matrix elements of Ca^+ and Yb^+

Investigator : Dr. Jirakan Nunkaew Chiang Mai University

E-mail Address : jn8h@virginia.edu

Project Period : 2 years

In the first experiment, we observe the microwave transitions of calcium from the *4snf* states to the *4s(n+1)d*, *4sng*, *4snh*, *4sni*, and *4snk* states for $18 \le n \le 23$ using delayed field ionization as the state selective detection technique. The observed intervals between the $l \ge 5$ states can be analyzed to extract the Ca^+ ionic dipole (α_d) and quadrupole (α_q) polarizabilities using two non-adiabatic core polarization models. Using these two models we determine the ionic dipole and quadrupole polarizabilities to be $75.3a_0^3 \le \alpha_d \le 76.9a_0^3$ and $206a_0^5 \le \alpha_q \le 1590a_0^5$, respectively.

In the second experiment, we use selective laser excitation to an autoionizing state to observe the microwave transitions of Ba from the *6sng* Rydberg states to the *6snh*, *6sni* and *6snk* states for $15 \le n \le 18$. We extract the dipole and quadrupole polarizabilities of Ba^+ from the measured Δl intervals of the Ba *6snl* states of $l \ge 5$ using a nonadiabatic core polarization model. The values we determine for the dipole and quadrupole polarizabilities are α_d =124.81(25) a_0^3 and α_q =2478(50) a_0^5, respectively.

Keywords: Rydberg atoms, autoionization, indirect spin-orbit coupling, Stark states, isolated core excitation

บทคัดย่อ

รหัสโครงการ : MRG5680117

ชื่อโครงการ : ความสามารถในการโพลาไรซ์และเมตริกซ์เอลิเมนต์ของแคลเซียมและอิเทอเบี่ยมไอออน

ชื่อนักวิจัย : อ.ดร. จิรกานต์ นันแก้ว มหาวิทยาลัยเชียงใหม่

E-mail Address : jn8h@virginia.edu

ระยะเวลาโครงการ : 2 ปี

ในงานวิจัยชิ้นแรกเราวัดการเปลี่ยนสถานะในช่วงคลื่นไมโครเวฟของแคลเซี่ยมจากสถานะ $4snf$ ไปยังสถานะ $(n+1)d$, $4sng$, $4snh$, $4sni$, และ $4snk$ สำหรับค่าเลขควอนตัมหลักระหว่าง 18 ถึง 23 โดยใช้เทคนิคการหน่วงเวลาของสนามไฟฟ้าในการทำให้อะตอมแตกตัวเป็นไอออน ความต่างของระดับพลังงานระหว่างสถานะควอนตัมโมเมนตัมเชิงมุมมากกว่า 5 ได้ถูกนำมาวิเคราะห์เพื่อหาค่าความสามารถในการโพลาไรซ์แบบไดโพล (α_d) และควอดดรูโพล (α_q) ของแคลเซี่ยมไอออนโดยใช้แบบจำลองโพลาไรซ์แก่นไอออนแบบไม่แอเดียบาติก 2 แบบ จากแบบจำลองเรากำหนดค่าความสามารถในการโพลาไรซ์แบบไดโพลของแคลเซี่ยมไอออนอยู่ระหว่าง $75.3\,a_0^3 \le \alpha_d \le 76.9\,a_0^3$ และความสามารถในการโพลาไรซ์แบบควอดดรูโพลของแคลเซี่ยมไอออนอยู่ระหว่าง 206 $a_0^5 \le \alpha_q \le$ 1590 a_0^5

ในงานวิจัยชิ้นที่สองเราใช้เทคนิคการเลือกสถานะการแตกตัวเป็นไอออนแบบอัตโนมัติโดยใช้เลเซอร์ในการกระตุ้นในการวัดการเปลี่ยนแปลงสถานะในช่วงคลื่นไมโครเวฟของแบเรี่ยมจากสถานะริดเบิร์ก $6sng$ ไปยังสถานะ $6snh$, $6sni$ และ $6snk$ สำหรับค่าเลขควอนตัมหลักระหว่าง 15 ถึง 18 เราวิเคราะห์ค่าความสามารถในการโพลาไรซ์แบบไดโพลและค่าความสามารถในการโพลาไรซ์แบบควอดดรูโพลของแบเรี่ยมไอออนจากการวัดความต่างของระดับพลังงานระหว่างสถานะควอนตัมโมเมนตัมเชิงมุมมากกว่า 5 โดยใช้แบบจำลองโพลาไรซ์แก่นไอออนแบบไม่แอเดียบาติก ค่าความสามารถในการโพลาไรซ์แบบไดโพลของแบเรี่ยมไอออนที่วิเคราะห์ได้เท่ากับ α_d =124.81(25) a_0^3 และค่าความสามารถในการโพลาไรซ์แบบควอดดรูโพลของแบเรี่ยมไอออนที่วิเคราะห์ได้เท่ากับ α_q =2478(50) a_0^5

คำหลัก : อะตอมริดเบิร์ก, การแตกตัวเป็นไอออนโดยอัตโนมัติ, การคู่ควบสปิน-ออร์บิทโดยอ้อม, สถานะสตาร์ค, การกระตุ้นแก่นไอออนแบบโดดเดี่ยว

I. EXECUTIVE SUMMARY

In recent years, many Nobel Prizes in Physics have been awarded to physicists in the field of Atomic, Molecular and Optical Physics (AMO) for their efforts in studying and controlling the dynamics of atomic systems such as the Bose-Einstein Condensation (BEC) and the optical frequency comb technique. In 2012, the Nobel Prize in Physics was awarded to Serge Haroche and David J. Wineland for ground-breaking experimental methods that enable measuring and manipulation of individual quantum systems. Haroche uses Rydberg atoms to control and measure the microwave photon in the cavity. While the success of controlling and manipulating the atomic systems is very exciting, many basic atomic measurements are still needed to further improve or create new ideas and experimental techniques. We will focus our interests on the dynamics and the properties of Rydberg atoms. The properties and interactions of Rydberg atoms have implications in many scientific fields. Rydberg atoms are candidates for realizing a quantum computer due to their strong interactions with each other. In interstellar space and in plasmas, atoms are commonly found in Rydberg states. Therefore, Rydberg atoms properties are important in determining the properties of plasma and radiation sources for astronomers [1].

In this project, the elements we study are calcium and barium. Due to the difficulty in optically accessing the high angular momentum Rydberg states of ytterbium, we have changed the element from ytterbium to barium. We measure the dipole α_d and quadrupole α_q polarizabilities of barium ion, Ba^+, using the selective photo-excitation to autoionizing states technique. We also measure the dipole α_d and quadrupole α_q polarizabilities of calcium ion, Ca^+, using delayed field ionization (DFI) technique.

It is possible to extract the dipole α_d and quadrupole α_q polarizabilities from the intervals between high ℓ Rydberg states of the atom, states of high enough ℓ that the Rydberg electron does not penetrate the ionic core [2–5]. We follow the usual convention that n and ℓ are the principal and orbital angular momentum quantum numbers of the Rydberg electron. In these non-penetrating states, the energy shifts from the hydrogenic levels arise from polarization of the core by the field from the Rydberg electron. In Rydberg states of lower ℓ, the electron comes closer to the core at the inner turning point of its orbit, and the energy shift is larger. Thus, measuring the $\Delta\ell$ intervals yields the polarizabilities of the ionic core. An excellent recent summary of core polarization analysis has been given by Lundeen [5].

Objective

1. Measure the energy intervals between the high angular momentum Rydberg states.

2. Use the measured energy intervals between the high angular momentum Rydberg states to determine the dipole (α_d) and quadrupole (α_q) polarizabilities of barium ion, Ba^+, and calcium ion, Ca^+.

3. Continue the study of the properties and dynamics of Rydberg atoms.

II. THE IONIC DIPOLE AND QUADRUPOLE POLARIZABILITIES OF CALCIUM

A. Experimental Approach

We excite neutral Ca atoms in a thermal beam from the ground state to a Rydberg state using three laser beams. The Ca beam intersects the laser beams at a 90 degree angle between two parallel horizontal copper plates separated by 1.2-cm long ceramic standoffs. The laser beams are focused to 1 mm diameters where they intersect the Ca beam. Ground state $4s^2$ atoms are excited to the $4s4p$, $4s4d$, and $4snf$ states by 422.791 nm, 732.816 nm, and $\sim$ 850 nm laser pulses, respectively, as shown in Fig. 1. The last laser is tunable over the range from 847 to 857 nm to excite the $4snf$ states of $18 \leq n \leq 23$. A 1-μs long microwave pulse starts 50 ns after the last laser pulse to excite the $4snf$ state to the $4sng$ and $4snh$ states by the one-photon and two-photon transitions, respectively. The $4snf \rightarrow 4sni$ and $4snf \rightarrow 4snk$ transitions are the three-photon and four-photon transitions. To drive the three-photon and four-photon excitations, in addition to a 1-μs microwave pulse, we use a continuous wave (cw) radio frequency (RF) field of frequency between 3.5 and 5 GHz. The RF and microwave fields are generated by a Hewlett-Packard (HP) 8257D analog signal generator and 83620A synthesized sweep generator, respectively. The microwave sweep generator produces a cw output from 10 MHz to 20 GHz, which is formed into pulses by a General Microwave DM862D switch. The required microwave frequencies to drive the transitions range from 23 to 75 GHz. Therefore, several frequency multipliers; a Narda DBS 2640X220 active doubler, a Narda DBS 4060X410 active quadrupler and a Pacific Millimeter V2W0 passive doubler are used to multiply the synthesizer frequency to the

desired frequency. The power output of the frequency multipliers ranges from 5 mW to 100 mW. The microwaves propagate through WR28 waveguide and a waveguide feedthrough to a WR28 horn inside the vacuum chamber. The cw RF propagates through a coaxial cable and a SMA feedthrough to the coaxial-to-waveguide adapter and is launched by a WR187 horn inside the chamber.

To discriminate between the $4sn\ell$ states of $\ell > 3$ and the $4snf$ state, we take advantage of the ℓ dependence of the lifetimes of Ca Rydberg atoms. The higher angular momentum Rydberg states live longer than the lower ones [6], and we use the technique of delayed field ionization (DFI). The lifetime of the $4s25f$ state has been measured to be $\sim$2.5(5) μs [6], and using the n^3 scaling law we find that the lifetimes of the $4snf$ states of $18 \leq n \leq 23$ fall in the range from 0.9 to 1.9 μs. Therefore, if we wait long enough after the microwave pulse, more than 5μs, atoms in the $4snf$ states decay significantly compared to atoms in the $4sn\ell$ states of $\ell > 3$. Typically, we apply a negative high voltage pulse to the bottom plate 8 to 10 μs after the microwave pulse to field ionize the surviving Rydberg atoms and drive the resulting electrons to the microchannel plate (MCP) detector. The timing of the experiment is shown in Fig. 2. Using this approach a large increase in the number of detected atoms is observed when the microwave field drives the transition from the $4snf$ state at resonance. To detect transitions from the $4snf$ states to the $4s(n+1)d$ states we take advantage of the fact that the lifetimes of the $4s(n+1)d$ states are an order of magnitude shorter than those of the $4snf$ states. A delay of only 2 μs is used, and a decrease in signal is observed at resonance. Frequency shifts due to the stray electric field are minimized by observing the microwave resonance with different bias voltages on the plates and fitting the resonant frequencies to a quadratic bias voltage dependence. We then set the bias voltage to the minimum frequency shift. In this experiment, the frequency shift due to the stray electric field is in all cases less than 1 MHz. The experiment is repeated every 50 ms, and the signals are averaged over many laser shots.

B. Experimental Observations

1. *One Photon $4snf \rightarrow 4sng$ Intervals*

For the one-photon transition, $4snf \rightarrow 4sng$, the microwave power was attenuated until the power broadening was eliminated. We observed one resonant peak for each n. Since the optical excitation is to the $4snf\ ^1F_3$ state we assign the states we observe in the microwave transitions as $^1G_4$ states. A typical resonance is shown in Fig. 3, and the observed intervals are given in Table I. We did not attempt to eliminate the Earth's magnetic field. In the Earth's magnetic field one might expect linewidths of $\sim 2-3$ MHz. However, the typical linewidth of a $^1F_3 -^1 G_4$ resonance is $\sim$1 MHz, the transform limited linewidth of a 1 μs microwave pulse. The narrow linewidths occur because the one photon transitions are between the two singlet states, which have the same Landé g_j factors. Hence, all the $\Delta m_j = 0$ transitions occur at the same frequency, resulting in the narrow lines [7].

TABLE I. $nf - ng$ observed frequencies

n	Observed Frequency (MHz)
18	72 891.40(1)
19	62 222.19(1)
20	53 150.84(2)
21	46 053.01(25)
22	40 147.03(1)
23	35 462.65(5)

2. *Two Photon $4snf \rightarrow 4snh$ Intervals*

For the two-photon transition, $4snf \rightarrow 4snh$, we observed two resonant peaks for each n suggesting that the higher ℓ states, $\ell \geq 5$, are not singlets and triplets. The states are described by coupling the total angular momentum of the core $\vec{j_c}$ to the orbital angular momentum $\vec{\ell}$ of the Rydberg electron to form $\vec{K}$. Explicitly,

$$\vec{K} = \vec{j_c} + \vec{\ell}. \tag{1}$$

The splitting between the two K levels is due to the indirect spin orbit splitting [8, 9]. We ignore the spin of the Rydberg electron. For the Ca $4sn\ell$ states, $j_c = 1/2$, therefore $K = \ell \pm 1/2$. Hence, for each ℓ state we observe two transitions from the $4snf$ to the $4sn\ell$ states, corresponding to $K = \ell + 1/2$ and $K = \ell - 1/2$. To correct for the small AC Stark shift due to the microwave field, 1.8 MHz at the highest power we used, the resonances were observed at different microwave powers, and the resonance frequencies were extrapolated linearly to zero microwave power to obtain unshifted $4snf - 4snh$ intervals. Typical resonances for the two-photon transitions are shown in Fig. 4, and the observed intervals are given in Table II. The typical linewidth of the resonances is 2-3 MHz. The linewidth is due to the Earth's magnetic field since the $4snh$ states are no longer singlets and triplets.

TABLE II. $nf - nh$ observed intervals and nh K splittings

n	K =9/2 (MHz)	K =11/2 (MHz)	K splitting (MHz)
18	95 296.36(6)	95 312.53(9)	16.17(11)
19	81 300.49(6)	81 314.41(3)	13.92(7)
20	69 905.16(18)	69 917.62(13)	12.46(22)
21	60 536.07(10)	60 546.51(9)	10.44(13)
22	52 761.38(96)	52 770.12(12)	8.74(97)
23	46 261.65(18)	46 269.19(5)	7.54(19)

3. Three Photon $4snf \rightarrow 4sni$ Intervals

For the three-photon transitions, a single microwave field does not have enough power to drive the three photon $4snf \rightarrow 4sni$ transitions. Therefore, the three-photon transitions were driven by using two microwave photons and one RF photon. The RF frequency of 3.5-5 GHz frequency was fixed near the $4snh - 4sni$ frequency, and the microwave frequency was swept. We verified that the observed resonances were indeed the $4snf \rightarrow 4sni$ transitions by varying the RF frequency within ± 5 MHz and sweeping the microwave frequency for each RF frequency. For each RF frequency, the $4snf \rightarrow 4sni$ interval, given by twice the microwave frequency plus the RF frequency, was approximately constant, with only a slight

difference in frequency due to the AC Stark shift. A typical three-photon resonance is shown in Fig. 6. In Fig. 6, we do not see the K splitting, because the K splitting in the $4sni$ states is not resolvable. Since most of the K splitting is from the dipole term, we can estimate the K splitting in the $4sni$ states using the adiabatic dipole term of Eqs. (37) and (38a) and ignoring the quadrupole term of Eq. (38b) of Ref. [8]. Explicitly,

$$K_{n\ell} = \frac{2(2\ell+1)\Delta_{4p}\langle r^{-6}\rangle_{n\ell}\langle 4s|r|4p\rangle^2}{9(W_{4s}-W_{4p})^3}, \tag{2}$$

where Δ_{4p} is the fine structure splitting of the Ca^+ $4p$ state, $\langle r^{-6}\rangle_{n\ell}$ is the expectation value of $1/r^6$ of the $n\ell$ Rydberg state, $\langle 4s|r|4p\rangle$ is the Ca^+ radial matrix element, W_{4s} is the energy of the Ca^+ $4s$ state and W_{4p} is the energy of the Ca^+ $4p$ state. Since we have measured the K splitting in the $4snh$ states, we can use Eq. (2) to estimate the K splitting in the $4sni$ states. The ratio between the K splitting in the $4sni$ and $4snh$ states is the ratio $\langle r^{-6}\rangle_{ni}/\langle r^{-6}\rangle_{nh} = 0.2$. Therefore, the K splitting in the $4sni$ states varies from 4 to 2 MHz as n increases from 18 to 23, which is not resolvable in our experiment due to the Earth's magnetic field.

In the three-photon transitions there are both RF and microwave power shifts. To eliminate the AC Stark shift from both fields, we observed the resonances at different RF and microwave powers. For a given microwave power, we observed resonances at different RF powers. We extrapolated the observed frequencies linearly to obtain the resonance frequency at zero RF power for a given microwave power. We repeated the same procedure for several microwave powers. The resonance frequencies at zero RF power of several microwave powers were extrapolated to obtain the resonance frequencies at zero RF and microwave powers. Typical power extrapolations are shown in Fig. 5, a typical resonance is shown in Fig. 6, and the unshifted intervals are given in Table III.

4. Four Photon $4snf \rightarrow 4snk$ Intervals

The $4snf \rightarrow 4snk$ four-photon transitions were excited using two microwave photons and two RF photons. The RF frequency was fixed near the $4snh \rightarrow 4snk$ resonance while the microwave frequency was swept in the vicinity of the $4snf \rightarrow 4snh$ resonance. Similar to the three-photon excitation, we verified that the observed resonances were the $4snf \rightarrow 4snk$ transitions by varying the RF frequency within ± 5 MHz and sweeping the microwave

TABLE III. $nf - ni$ observed intervals

n	Observed Frequency (MHz)
18	102 558.95(54)
19	87 488.41(40)
20	75 223.05(15)
21	65 141.32(78)
22	56 766.61(69)
23	49 771.37(26)

frequency for each RF frequency. For each RF frequency, the $4snf \rightarrow 4snk$ interval was given by twice the microwave frequency plus twice the RF frequency and was approximately constant. We eliminated the AC Stark shifts using the process discussed for the three-photon transitions. Typical signals for four-photon transitions are shown in Fig. 7, and the unshifted intervals are given in Table IV. Using Eq. (2), we estimate the K splitting in the $4snk$ states to be on the order of 1 MHz for $18 \leq n \leq 20$, which cannot be resolved in this experiment.

TABLE IV. $nf - nk$ observed intervals

n	Observed Frequency (MHz)
18	105 362.90(52)
19	89 879.91(7)
20	77 278.61(15)

5. One Photon $4snf \rightarrow 4s(n+1)d$ Intervals

We have observed the $4snf \rightarrow 4s(n+1)d$ transitions for n =19, 20, and 21. In this region the $4snd\ ^1D_2$ Rydberg states are perturbed by their interaction with the $3d^2\ ^1D_2$ state [10]. The perturbation results in shorter lifetimes and rapidly changing quantum defects. For $19 \leq n \leq 21$ the $4snd\ ^1D_2$ states lie close enough in energy to the $4snf\ ^1F_3$ states that the $4snf \rightarrow 4s(n+1)d$ frequencies are within the microwave frequency range that we can generate. A typical resonance is shown in Fig. 8, and the observed intervals are presented

in Table V.

TABLE V. $nf - (n+1)d$ observed intervals

n	Observed Frequency (MHz)
19	84 377.04(4)
20	49 143.13(12)
21	24 542.36(4)

C. Discussion

We use the adiabatic expansion method [11] and direct calculation method to determine the values of α_d and α_q [13]. Tables XIII and XIV show values of α_d and α_q from this work and other experimental and theoretical work. The uncertainties for our values represent the uncertainties from the fits of the data to the two models. The values labelled $_{ae}$ are from the adiabatic expansion method and the values are from the direct calculation method. There are three experimental results for α_d to which we can compare ours. The value of ref. [6] is based on the measurement of the $4snf \rightarrow 4sng$ intervals. The analysis of these data relied heavily on a more complex theoretical model, which was probably inadequate to represent the $4sng$ states. The value of α_d given in ref. [14] was obtained by assuming that the $4snh$ quantum defects arise solely from the dipole polarizability and applying the adiabatic core polarization model. Since the quadrupole polarizability is small and the nonadiabatic effect on the dipole polarization cancels its effect to some extent, this approach yields a value for α_d close to the value we obtained by analyzing our data using the adiabatic approximation method of Mayer and Mayer [3]. In ref. [15] lifetime measurements of the Ca^+ $4p_j$ states were used to obtain the oscillator strengths of the $4s - 4p_j$ transitions, taking into account the small branching ratios for decay to the $3d_j$ states. The oscillator strengths of the $4s-4p_j$ transitions were then used to calculate the value of α_d. The resulting value of α_d is too small due to the neglect of higher lying Ca^+ Np states and the dipole polarizability of Ca^{++}, but when this omission is taken into account it is consistent with our value for α_d. The theoretical values for α_d from refs. [12] and [16] fall within our experimental bounds given in Eq. (3), while the theoretical value of ref. [17] is clearly outside the bounds.

To our knowledge, our values of α_q are the first experimental values. As shown in Table XIV, our value obtained by the adiabatic expansion method is twice the theoretical value, and the value obtained by the direct calculation method is a factor of four smaller than the theoretical value. Since a large fraction, two thirds, of the quadrupole polarizability is due to the Ca^+ $3d$ states, an alternative check of the calculated quadrupole polarizability is the lifetime of the Ca^+ $3d$ state, which decays by quadrupole radiation. The measured lifetime is in good agreement with the calculated lifetime, supporting the validity of the calculation of α_q. It is worth noting that if the value of k_d for the $4snh$ states is reduced to 98.35% of the current k_d value we would obtain $\alpha_d = 75.3(1)$ a_0^3 and $\alpha_q = 878(15)$ a_0^5, in excellent agreement with the recent theoretical values. In view of the sensitivity of the direct calculation approach to the numerical calculations of k_d and the large discrepancy between our value of α_q and the theoretical values, we view the direct calculation values of Tables XIII and XIV as upper and lower bounds for α_d and α_q, respectively. As a consequence, we report bounds for α_d and α_q. Explicitly,

$$75.3\ a_0^3 < \alpha_d < 76.9\ a_0^3 \tag{3}$$

and

$$206\ a_0^5 < \alpha_q < 1590\ a_0^5. \tag{4}$$

Our ability to specify α_d and α_q is limited by our confidence in the core polarization models. Two experimental avenues can be explored to minimize this problem. The first is measuring higher ℓ intervals in which the non adiabatic corrections are not as large, as done by Lundeen et al. for other atoms [5]. The second is high resolution laser spectroscopy of the Ca $4snd\ ^1D_2$ states. Absolute measurements of their energies, good to 10 MHz, would locate the $4snd$ levels relative to the hydrogenic $n\ell$ levels. The microwave measurements reported here could then be used to locate the Ca $4sn\ell$ levels relative to the H $n\ell$ levels, and the present data could then be analyzed in terms of the displacements of the energies from the hydrogenic levels, instead of the differences in the displacements. The $4snh$ states could be dropped from the analysis, substantially reducing the uncertainty due to the non-adiabatic corrections.

Making measurements involving higher ℓ states should minimize the non adiabatic effects, allowing a better determination of the polarizabilities. However, it is not obvious that the discrepancy between the theoretical and experimental values will disappear. Intervals

TABLE VI. The Ca^+ 4s dipole polarizability (α_d) obtained from this work and other theoretical and experimental results.

	α_d (a_0^3)
This work$_{ae}$	75.32(4)
This work$_{dc}$	76.9(3)
Expt. [6]	87(2)
Expt. [14]	75.3(4)
Expt. [15]	70.89(15)
Theory [12]	76.1(5)
Theory [17]	73.0(1.5)
Theory [16]	75.49

TABLE VII. The Ca^+ 4s quadrupole polarizability (α_q) obtained from this work and other theoretical results.

	α_q (a_0^5)
This work$_{ae}$	1590(40)
This work$_{dc}$	206(9)
Theory [12]	871(4)
Theory [16]	875.1

between the high ℓ Ba $6sn\ell$ levels have been measured, but the value of α_q extracted by the direct calculation method is a factor of two smaller than the theoretical value, a similar discrepancy to that reported here for Ca [19]. Determining the source of these discrepancies is a worthy theoretical challenge. The output and the detailed data analysis of the experiment can be found at [18].

D. Conclusion

We have measured $\Delta\ell$ intervals of Ca $4snf \rightarrow 4sn\ell$, $18 \leq n \leq 23$ and $4 \leq \ell \leq 7$ using a microwave and RF resonance approach. We have used these measurements to place bounds on the Ca^+ dipole and quadrupole polarizabilities. The Ca^+ $4s$ dipole and quadrupole

polarizabilities are 75.3 $a_0^3 < \alpha_d < 76.9\ a_0^3$ and 206 $a_0^5 < \alpha_q < 1590\ a_0^5$. The Ca^+ $4s$ dipole polarizability agrees well with recent theoretical values. However, we are not able to place tight bounds on the Ca^+ $4s$ quadrupole polarizability due to uncertainties in the core polarization analyses. We hope this work will motivate theoretical work to reexamine the problem of core polarization analysis and, more generally, the source of the discrepancy between the experimental and theoretical values of α_q.

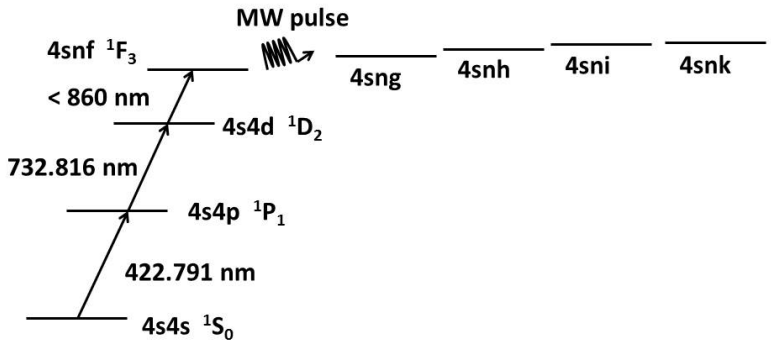

FIG. 1. Laser excitation scheme of the experiment.

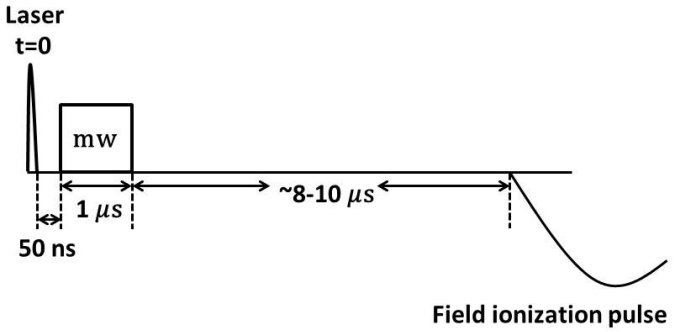

FIG. 2. The timing sequence of the experiment.

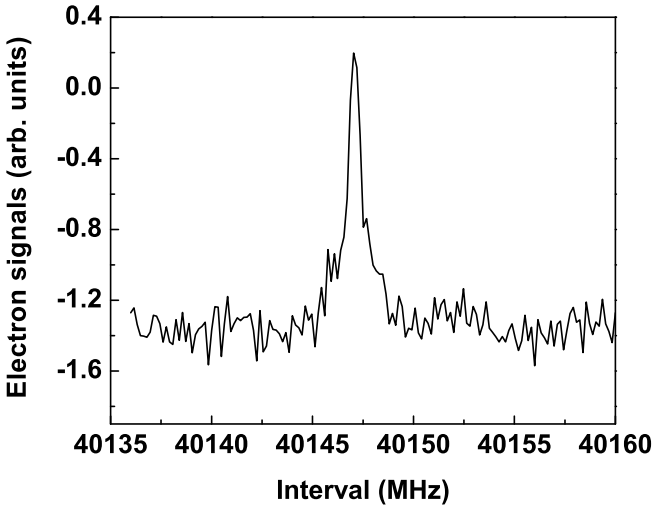

FIG. 3. One-photon $4s22f \rightarrow 4s22g$ resonance. The linewidth of the resonance is $\sim$1 MHz which is a transform limited linewidth of a 1 μs microwave pulse.

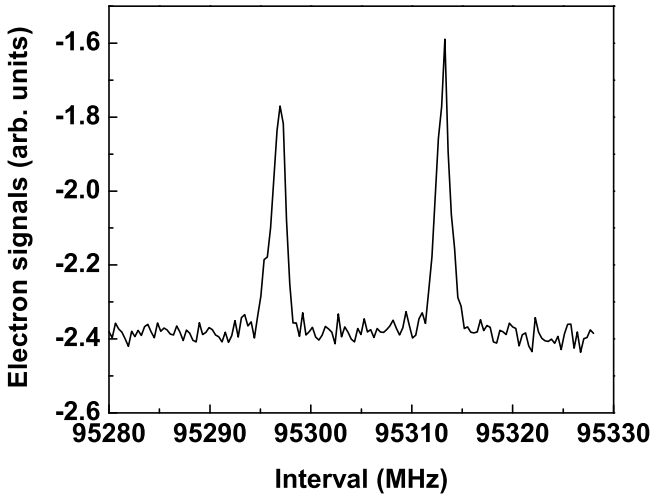

FIG. 4. Two-photon $4s18f \rightarrow 4s18h$ resonances. The two resonances are separated by the K splitting of the $4s18h$ state.

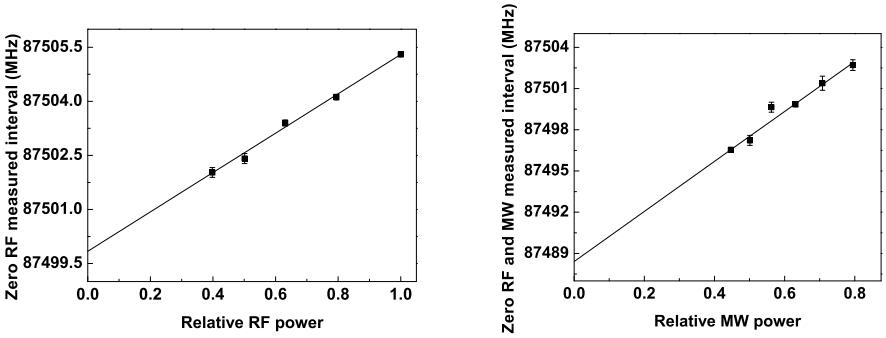

(a) (b)

FIG. 5. The extrapolation of the three photon $4s19f \rightarrow 4s19i$ transition to zero RF and microwave powers. (a) At relative microwave power 0.63, resonances were observed at different RF powers to obtain the resonance frequency at zero RF power. (b) Several zero RF power resonances were obtained at different microwave powers and extrapolated to zero RF and microwave powers.

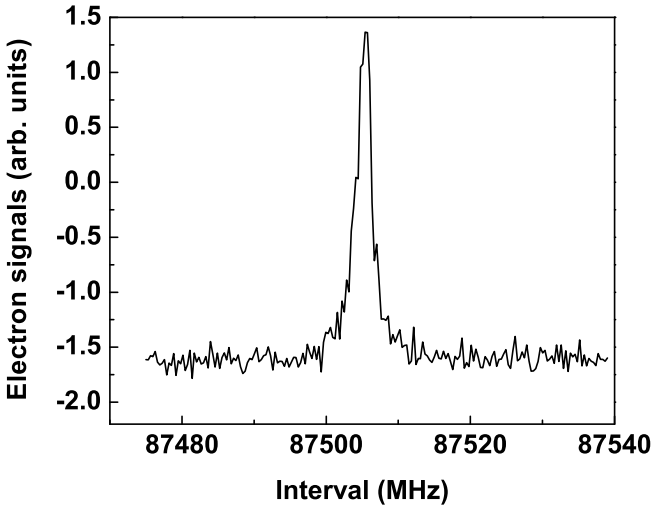

FIG. 6. Three-photon $4s19f \rightarrow 4s19i$ resonance at relative microwave power 0.63 and at relative RF power 1.0. The K splitting of the $4s19i$ states cannot be resolved due to the Earth's magnetic field broadening.

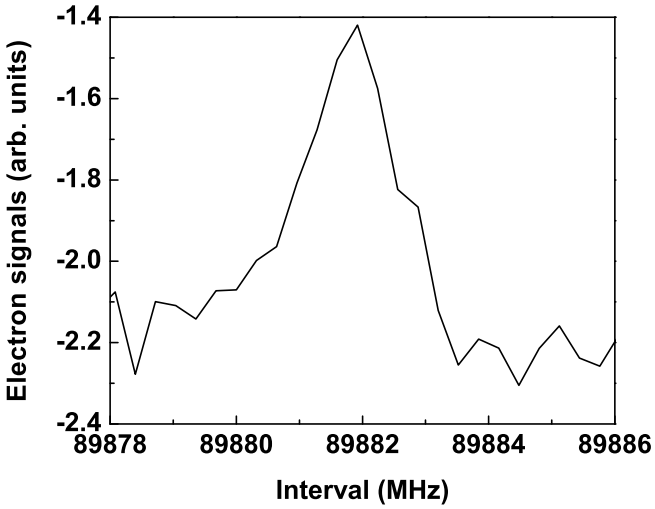

FIG. 7. Four-photon $4s19f \rightarrow 4s19k$ resonance at 0.178 relative microwave power and 0.794 relative RF power. The K splitting of the $4s19k$ states is on the order of 1 MHz and cannot be resolved.

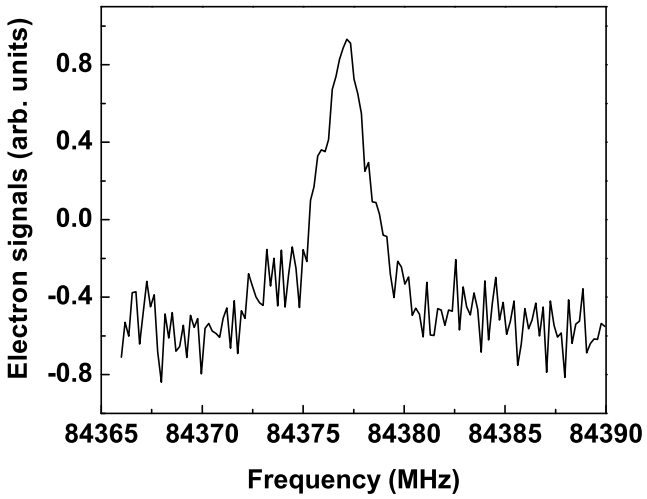

FIG. 8. One-photon $4s19f \rightarrow 4s20d$ resonance.

III. THE IONIC DIPOLE AND QUADRUPOLE POLARIZABILITIES OF BARIUM

A. The microwave $\Delta\ell$ transitions and their detection using isolated core excitation (ICE)

The $\Delta\ell$ microwave transitions we observe are shown in Fig. 9. The $6sng\ ^1G_4$ state is populated by laser excitation, and we drive the microwave transitions to the $6sn\ell$ states of $5 \leq \ell \leq 7$. The higher ℓ states are not singlets and triplets. Rather, the total angular momentum of the core $\vec{j_c}$ is coupled to the orbital angular momentum $\vec{\ell}$ of the Rydberg electron to form $\vec{K}$. Explicitly,

$$\vec{K} = \vec{j_c} + \vec{\ell}. \tag{5}$$

We ignore the spin of the Rydberg electron. Since $j_c = 1/2$, $K = \ell \pm 1/2$, and for each ℓ state we observe two transitions, as shown in Fig. 9. The splitting between the two K levels is due to the indirect spin orbit splitting [8, 9].

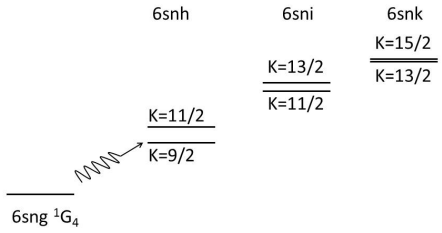

FIG. 9. The Ba $6sn\ell$, $\ell \geq 4$ states showing the microwave transitions and the K splittings due to the indirect spin orbit coupling of the $6sn\ell$, $\ell \geq 5$, Rydberg states.

Detection of the Ba $6sn\ell \rightarrow 6sn\ell'$ transitions ($\ell' > \ell$) is based on the difference in the optical cross sections of the $6sn\ell \rightarrow 6p_{1/2}n\ell$ and $6sn\ell' \rightarrow 6p_{1/2}n\ell'$ ICE transitions. Previously, Cooke and Gallagher used the substantial difference in the wavelengths of the Sr $5snd \rightarrow 5pnd$ and $5snf \rightarrow 5pnf$ ICE transitions to detect the Sr $5s(n+2)d \rightarrow 5snf$ microwave transitions [25]. In ICE of the $6sn\ell$ state, the $6s$ electron absorbs the photon while the $n\ell$ electron is a spectator. The $6s \rightarrow 6p_{1/2}$ transition of the inner electron is

essentially the Ba^+ $6s \rightarrow 6p_{1/2}$ transition, with an oscillator strength of 1/3. The oscillator strength is spread over the spectral width of the $6p_{1/2}n\ell$ state, which is determined by its autoionization rate. In this case, the peak optical cross section is given by

$$\sigma_{\rm peak} = \frac{\lambda^2 A}{8\pi\Gamma_{n\ell}}, \tag{6}$$

where A is the Einstein A coefficient for the Ba^+ $6s \longrightarrow 6p_{1/2}$ transition, $\Gamma_{n\ell}$ is the autoionization rate of the $6p_{1/2}n\ell$ state, and λ is the wavelength of the transition, 493.5 nm in this case. We have implicitly assumed that the autoionization rates of the $6p_{1/2}n\ell$ states exceed their radiative decay rates, which is in all cases simply the radiative decay rate of the Ba^+ $6p_{1/2}$ state. For the $6p_{1/2}n\ell$ states of interest this condition is easily met. However, for $n \geq 30$ the autoionization rate of a $6p_{1/2}n\ell$ state of $\ell = 7$ is less than the radiative decay rate, and this method of detection will no longer work [26].

The autoionization rates of the Ba $6p_{1/2}n\ell$ states of $\ell \geq 4$ decrease by roughly a factor of five with each increase in ℓ of one [27]. Accordingly, the cross section for the $6sn\ell \rightarrow 6p_{1/2}n\ell$ ICE transition increases by a factor of five for each increase in ℓ of one. Even if the center frequencies of the ICE transitions are the same, approximately the ionic $6s \rightarrow 6p_{1/2}$ frequency, it is possible to observe transitions between the $6sn\ell$ and $6sn\ell'$ states, as shown in Fig. 10. Fig. 10 is drawn assuming the two ICE transitions occur at the ionic frequency and that $\ell' = \ell + 1$, so the ICE cross sections and widths differ by a factor of five. The linewidth of the laser driving the ICE transition must be less than the width of the $6p_{1/2}n\ell$ state, and the power of the laser must also be kept below saturation of the $6sn\ell' \rightarrow 6p_{1/2}n\ell'$ transition. If the laser linewidth is less than the $6p_{1/2}n\ell'$ linewidth and the $6sn\ell' \rightarrow 6p_{1/2}n\ell'$ transition is not saturated, an atom in the $6sn\ell'$ state is five times as likely as one in the $6sn\ell$ state to undergo the ICE transition when the ICE laser is tuned to the peak of the cross sections, at the ionic frequency. In short, with the ICE laser tuned to the peak of the cross sections, driving the $6sn\ell \rightarrow 6sn\ell'$ microwave transition can result in a fivefold increase in the autoionization signal at the $6sn\ell - 6sn\ell'$ microwave resonance. Alternatively, the ICE laser can be tuned to the wing of the $6sn\ell \rightarrow 6p_{1/2}n\ell$ transition, in which case the microwave $6sn\ell \rightarrow 6sn\ell'$ transition results in a decrease in the autoionization signal.

In Ba, the $6sn\ell \rightarrow 6p_{1/2}n\ell$ transition frequencies depend on both n and ℓ. Fig. 11 shows the ℓ-dependence of the $6s17\ell \rightarrow 6p_{1/2}17\ell$, ℓ=4 and 5, ICE cross sections. We do not show the $6s17\ell \rightarrow 6p_{1/2}17\ell$ ICE cross sections for $\ell > 5$ since the peak cross sections are so much

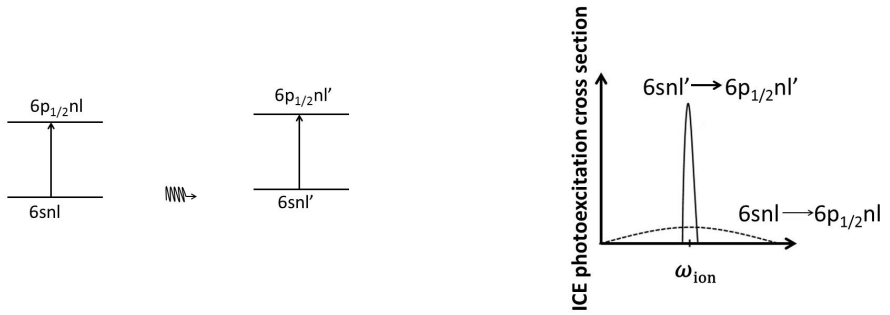

(a) (b)

FIG. 10. (a) The $6snl \rightarrow 6snl'$ microwave transition can be detected using the difference in the two ICE cross sections. (b) The ICE cross sections of the $6snl \rightarrow 6p_{1/2}nl$ and $6snl' \rightarrow 6p_{1/2}nl'$ transitions. With the ICE laser tuned to the peak of the cross sections, driving the $6snl \rightarrow 6snl'$ microwave transition can result in a fivefold increase in the autoionization signal at the $6snl - 6snl'$ microwave resonance if $\ell' = \ell + 1$.

higher. We do, however, show the location of the $\ell = 6$ ICE transition. The higher ℓ ICE transitions lie closer to the ion $6s - 6p_{1/2}$ transition at 20261.56 cm^{-1}. Since the $6s17g$ and $6s17h$ ICE transitions are not superimposed, at the peak of the $6s17h$ ICE transition the ratio of the cross sections is not five, but ten. While the increased selectivity is attractive, the displacement of the ICE transitions with ℓ does complicate finding the ICE transitions for higher ℓ states. In this case the most straightforward approach might be to set the ICE laser to the high frequency side of the $6s17g \rightarrow 6p_{1/2}17g$ transition and look for a decrease in the autoionization signal to detect the $6s17g \rightarrow 6s17\ell$ microwave transitions. However, we have used a different approach. Since the frequencies of the transitions from the Ba $6s18g$ state to the $6s18h$, $6s18i$, and $6s18k$ states are known [21], we set the microwave frequency to the $6s18g \rightarrow 6s18\ell$ resonance and scanned the ICE laser to find the $6s18\ell \rightarrow 6p_{1/2}18\ell$ ICE transition, which occurs at the frequency ν_ℓ, given by

$$\nu_\ell = \nu_{ion} + \frac{\delta_{\ell_s} - \delta_{\ell_p}}{n^3}, \tag{7}$$

where ν_{ion} is the Ba$^+$ $6s - 6p_{1/2}$ frequency, and δ_{ℓ_s} and δ_{ℓ_p} are the quantum defects of the $6snl$ and $6p_{1/2}n\ell$ states, respectively. When n is decreased by one the change in the ICE

frequency, $\Delta\nu_\ell$, is given by

$$\Delta\nu_\ell = 3\frac{\delta_{\ell_s} - \delta_{\ell_p}}{n^4}. \tag{8}$$

For $n = 18$ and $\ell = 5$, $\Delta\nu_\ell = 2.5$ GHz, which is small compared to the 10 GHz width of the $6p_{1/2}18h$ state. In short, knowing the $\ell = 5$, 6, and 7 ICE frequencies for $n = 18$ allows us to predict them accurately enough to make the $n = 17$, 16, and 15 measurements.

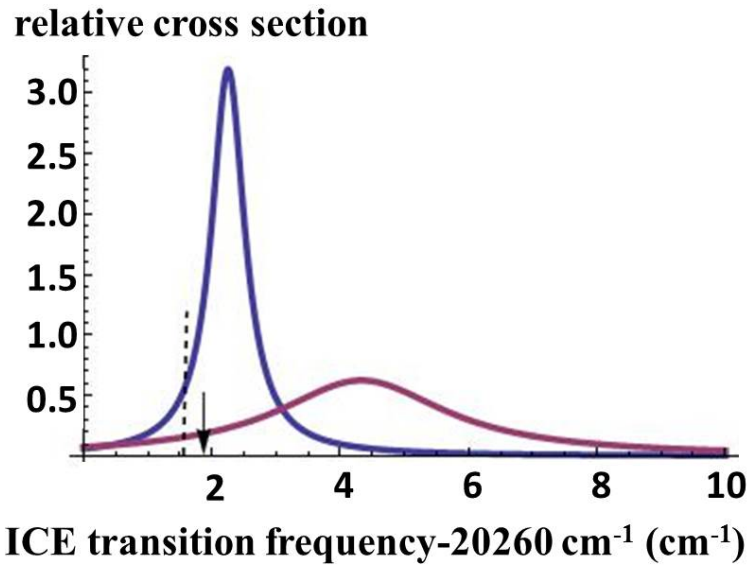

FIG. 11. (Color online) The ICE cross sections for the $6s17g$ and $6s17h$ states. The wider ICE cross section is the $6s17g \rightarrow 6p_{1/2}17g$ transition. The narrower ICE cross section is the $6s17h \rightarrow 6p_{1/2}17h$ transition. The arrow shows the location of the $6s17i \rightarrow 6p_{1/2}17i$ ICE transition. The dashed line shows the location of the ionic $6s \rightarrow 6p_{1/2}$ transition frequency.

B. Experimental Approach

We prepare $6sng$ barium Rydberg states by exciting neutral barium atoms in a beam with four laser pulses. The excitation scheme from the ground state $6s^2$ to the $6sng$ state is shown in Fig.12. Photo-ions and electrons are produced, so the excitation is performed in a small electric field, less than 100 V/cm, to remove them.

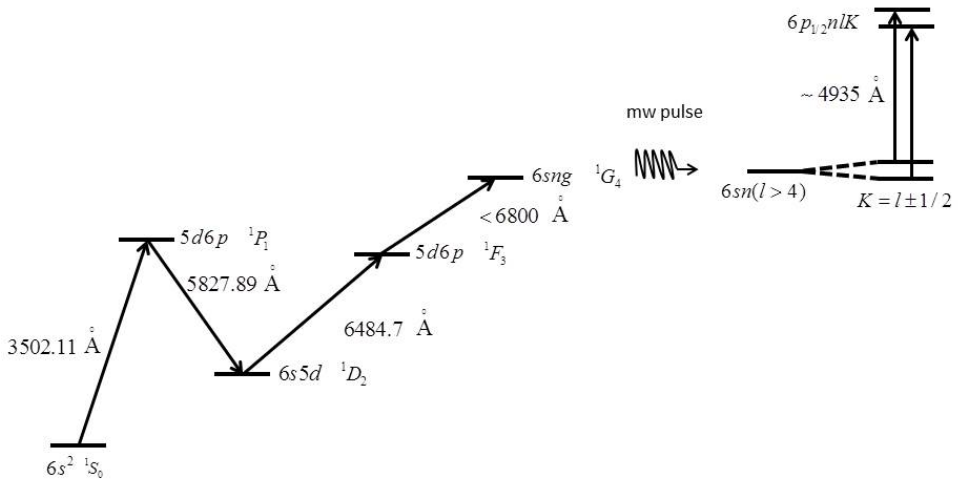

FIG. 12. Laser excitation scheme of the experiment.

As shown by the timing diagram of Fig. 13 after the four laser pulses, we turn off the electric field and wait 200 ns for any ringing from the electronics to dissipate. It is important that there be no stray electric field on the Rydberg atoms during the microwave pulse to avoid Stark shifts of our observed intervals. To drive the $6sng \rightarrow 6snh$ and $6sng \rightarrow 6sni$ transitions, we apply a single 1 μs pulse of microwaves; while for the $6sng \rightarrow 6snk$ transitions, we use a continuous radio frequency (RF) field in addition to a 1 μs microwave pulse. When the microwave pulse ends, we immediately apply a ∼493.5 nm frequency doubled, dye-amplified diode laser pulse, which excites the $6sn\ell$ atoms to the autoionizing $6p_{1/2}n\ell$ states. The $6p_{1/2}n\ell$ atoms autoionize quickly, and we apply an electric field ramp to drive the resulting ions to the microchannel plate detector. The peak of the field ramp is high enough to ionize bound $6sn\ell$ atoms of $n > 16$, but the signal from bound state atoms arrives 1 μs later than the signal from autoionizing atoms. The two signals are temporally well resolved, and we set the gate of the gated integrator on the autoionization signal.

This excitation and detection cycle is repeated every 50 ms, and our signals are averaged over many laser shots.

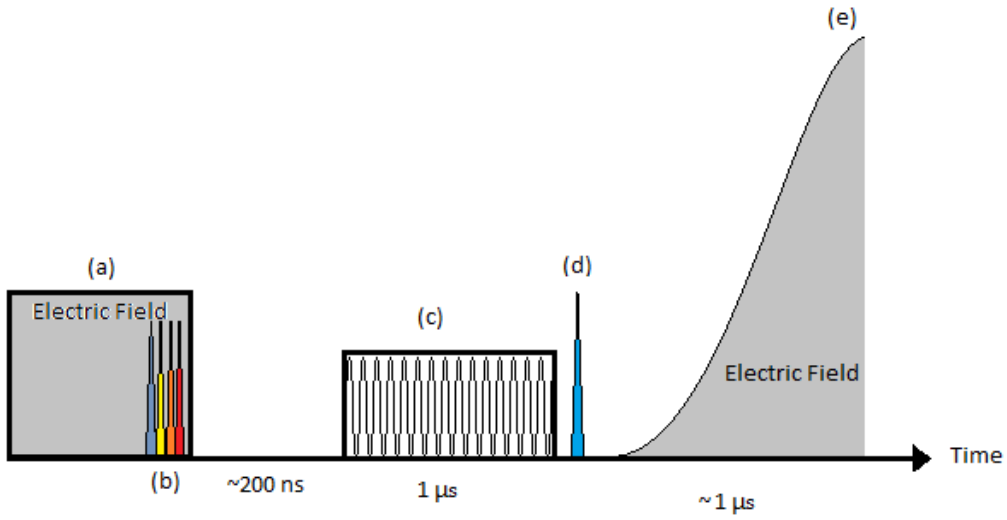

FIG. 13. The timing sequence for the lasers, microwaves, and RF signals. (a) Small electric field to clear photo-ions (b) Four laser pulses to drive the $6s^2 \rightarrow 6sng$ transition (c) 1 μs MW pulse (d) ICE laser pulse (e) Electric field ramp

C. Experimental Observations

1. *One Photon Intervals*

To obtain the single photon intervals, we started from the known $6s18g - 6s18h$ transitions. We used a high microwave power at the $6s18g - 6s18h$ resonance to equilibrate the populations, and we swept the diode laser frequency to find the frequency of the $6s18h \rightarrow 6p_{1/2}18h$ ICE transition. With the laser set to the ICE frequency we then attenuated the microwave power and scanned the microwave frequency to repeat the earlier measurements. To find the $6sng - 6snh$ transitions of $n < 18$, we changed the diode laser frequency from its $n = 18$ value using Eq. (7) and scanned the microwave frequency at high power to find a small resonance signal. We then optimized the signal by adjusting the diode laser frequency with the microwave frequency set to the $6sng - 6snh$ frequency. Once we found the optimal diode laser frequency, we performed our microwave scans at reduced microwave power.

Typical resonances, for $n = 15$, are shown in Fig. 14. There are two resonances, corresponding to the two possible values of K for the $6s15h$ state. The one-photon transition

frequencies for $6sng$ to $6snh$, $15 \leq n \leq 18$ are shown in Table VIII.

TABLE VIII. $ng - nh$ observed frequencies and K splittings

n	K =9/2 (MHz)	K =11/2 (MHz)	K splitting (MHz)
18	40 180.0(6)	41 147.4(7)	967.4(9)
17	47 367.4(6)	48 547.2(6)	1179.8(8)
16	56 489.4(6)	57 959.0(5)	1469.6(8)
15	68 185.8(5)	70 063.6(5)	1877.8(7)

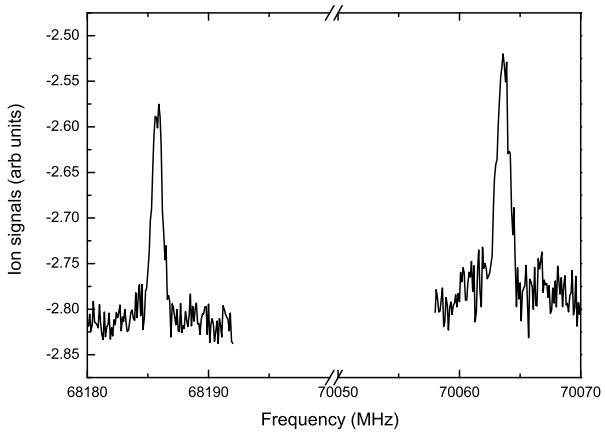

FIG. 14. The single photon $6s15g \rightarrow 6s15h$ transitions. The two peaks are separated by the K splitting.

2. Two Photon Intervals

The procedure used for the two photon transitions from $6sng$ to $6sni$ was similar to that used for the one photon transitions. Using the known $6s18g - 6s18i$ transition frequencies we found the ICE wavelength for $6s18i$, which could then be adjusted for lower n using Eq. (7). The two photon $6sng - 6sni$ transition occurs via a virtual intermediate state, and there is a small but measurable AC Stark shift due to the microwave field. To obtain the unshifted intervals, we took measurements at multiple microwave powers and extrapolated

our results to zero microwave power. With the available microwave power the maximum AC Stark shift was 1.65 MHz. The uncertainties are those given by the statistical fits to the power extrapolations. Typical two photon resonances, for $n = 15$, are shown in Fig. 15.

TABLE IX. $ng - ni$ observed intervals and K splittings

n	K =11/2 (MHz)	K =13/2 (MHz)	K splitting (MHz)
18	51 422.9(3)	51 654.6(3)	231.7(4)
17	60 667.8(6)	60 926.7(8)	258.9(10)
16	72 375.6(3)	72 669.2(3)	293.6(4)
15	87 359.8(4)	87 691.3(3)	331.5(5)

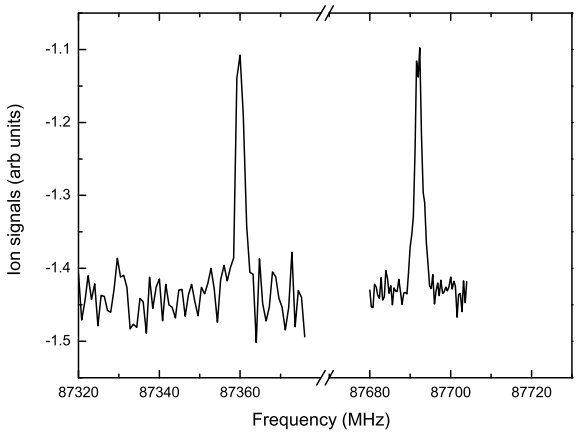

FIG. 15. The two photon transitions $6s15g \rightarrow 6s15i$. The two resonances are separated by the K splitting of the $6s15i$ state.

3. Three Photon Intervals

We located the $6snk \rightarrow 6p_{1/2}nk$ ICE transitions in essentially the same manner used to find the $6snh \rightarrow 6p_{1/2}nh$ and $6sni \rightarrow 6p_{1/2}ni$ ICE transitions. We do not have enough

TABLE X. $ng - nk$ frequencies and intervals

n	K	approximate RF frequency (MHz)	approximate microwave frequency (MHz)	extrapolated interval(MHz)
18	13/2	4920	25 750	56 388.0(20)
	15/2	4640	25 895	56 424.5(30)
17	13/2	5750	30 390	66 521.1(12)
	15/2	5750	30 400	66 562.4(17)
16	13/2	7050	36 125	79 351.4(17)
	15/2	7050	36 150	79 393.0(20)
15	13/2	8300	43 720	95 739.1(20)
	15/2	8100	43 875	95 798.9(20)

microwave power to drive the three photon $6sng - 6snk$ transitions using a single microwave field. Instead, we use two frequencies. One is close to the two photon $6sng - 6sni$ microwave frequency, and the other is close to the $6sni - 6snk$ frequency, which, for clarity, we term a radio frequency (RF), even though it can be as high as 8.3 GHz. In all cases, the RF frequency was fixed and the microwave frequency swept. We verified that if we changed the RF frequency the $6sng - 6snk$ intervals were given by twice the microwave frequency plus the RF frequency, indicating that the resonance was due to two microwave photons and one RF photon.

There are now two AC Stark shifts, due to the microwave and RF fields. We performed microwave frequency sweeps at different microwave powers and constant RF power, allowing us to extrapolate the observed resonance frequencies to zero microwave power for a given RF power. We repeated this procedure for several different RF powers to extrapolate to zero microwave and RF power. Our fit for the $6s17g \rightarrow 6s17k$, $K = 15/2$ transition is shown in Fig. 16. As expected, the RF power shift is more important since the RF field is nearly resonant with a one photon transition. In Table III we give the measured intervals after extrapolation, as well as the approximate microwave and RF frequencies used. The uncertainties in our reported intervals correspond to the uncertainties of the power extrapolations.

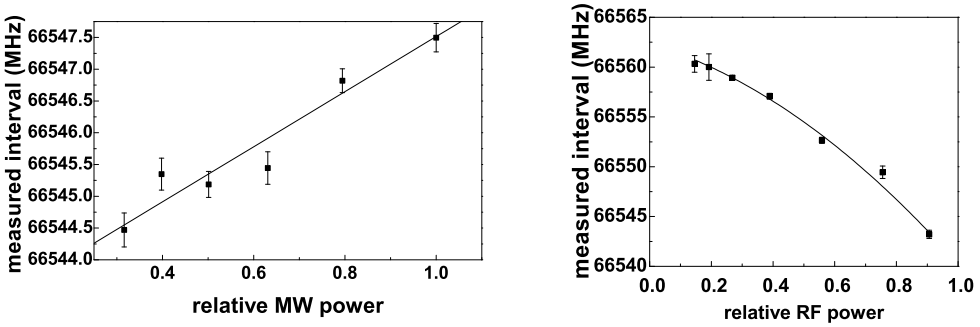

(a) (b)

FIG. 16. The extrapolation of the three photon $6s17g \rightarrow 6s17k$ $K = 15/2$ transition to zero power. (a) Resonances were recorded for multiple microwave powers at each RF power to determine the zero microwave power resonance frequency for each RF power. (b) These zero microwave power frequencies were then extrapolated to find the zero power interval, assuming a linear plus quadratic RF power shift, as shown.

IV. CORE POLARIZATION ANALYSIS OF THE DATA

The adiabatic core polarization model of Mayer and Mayer provides an instructive starting point for the analysis. In it, the energy by which a Ba $6sn\ell$ Rydberg state lies below the hydrogenic energy of $-1/2n^2$ is given by [3]

$$W_{\mathrm{pol},n\ell} = -\frac{1}{2}\alpha_d \langle r^{-4}\rangle_{n\ell} - \frac{1}{2}\alpha_q \langle r^{-6}\rangle_{n\ell}, \tag{9}$$

where α_d and α_q are the dipole and quadrupole polarizabilities of the Ba^+ ionic core, and $\langle r^{-4}\rangle_{n\ell}$ and $\langle r^{-6}\rangle_{n\ell}$ are the expectation values of the squares of the $n\ell$ Rydberg electron's field and field gradient at the core. The model is termed adiabatic because it is based on the assumption that the Rydberg electron is slowly moving compared to the electrons in the core, providing an essentially static field.

For comparison to experimental data, it is convenient to use Edlen's form of Eq (9) [4]:

$$W_{\mathrm{pol},n\ell} = -\alpha_d P_{n\ell} - \alpha_q P_{n\ell} Q_{n\ell}, \tag{10}$$

where

$$P_{n\ell} = R\langle r^{-4}\rangle_{n\ell}, \tag{11}$$

$$Q_{n\ell} = \frac{\langle r^{-6}\rangle_{n\ell}}{\langle r^{-4}\rangle_{n\ell}}, \tag{12}$$

and R is the Rydberg constant for Ba; $R = 109736.88$ cm^{-1}. Experimentally, we observe the $\Delta\ell$ energy intervals, $\Delta W_{\mathrm{pol},n\ell'\ell} = W_{\mathrm{pol},n\ell'} - W_{\mathrm{pol},n\ell}$, between Ba $6sn\ell$ and $6sn\ell'$ states of the same n, and we can express the observed intervals in terms of Eq. (10) using

$$\frac{\Delta W_{\mathrm{pol},n\ell'\ell}}{\Delta P_{n\ell\ell'}} = \alpha_d + \alpha_q \frac{\Delta PQ_{n\ell\ell'}}{\Delta P_{n\ell\ell'}}. \tag{13}$$

Here $\Delta P_{n\ell\ell'} = P_{n\ell} - P_{n\ell'}$, and $\Delta PQ_{n\ell\ell'} = P_{n\ell}Q_{n\ell} - P_{n\ell'}Q_{n\ell'}$. The $\Delta\ell$ intervals are largely determined by the dipole polarizability, and in Eq. (13) we have removed the variation due to the dipole polarizability by dividing by $\Delta P_{n\ell\ell'}$. Plotting the left hand side of Eq. (13) vs $\Delta PQ_{n\ell\ell'}/\Delta P_{n\ell\ell'}$ yields a graph with intercept α_d and slope α_q. In Fig. 17, we have plotted Eq. (13) for the Ba $6sn\ell$ $\ell \to \ell + 1$ intervals of $\ell \geq 5$. The experimental intervals are taken from Gallagher et al [21], Snow and Lundeen [22], and this work. The $\ell \to \ell + 1$ intervals of $\ell > 6$, n=17 and 20, the high ℓ intervals, at $\Delta PQ_{n\ell\ell'}/\Delta P_{n\ell\ell'} < 0.002$ fall on a line, as expected, but the $\ell = 6 \to \ell = 7$, $ni - nk$, intervals at $\Delta PQ_{n\ell\ell'}/\Delta P_{n\ell\ell'} \approx 0.0025$ lie distinctly above the line, and the $\ell = 5 \to \ell = 6$, $nh - ni$, intervals, at $\Delta PQ_{n\ell\ell'}/\Delta P_{n\ell\ell'} \approx 0.0053$, lie well below the line. The latter two sets of data are displaced from the line due to the breakdown of the adiabatic assumption implicit in Eq. (9).

Almost immediately after the appearance of the paper by Mayer and Mayer van Vleck and Whitelaw pointed out that Eq. (9) is valid only in the limiting case in which the excited states of the ionic core are far above its ground state. Furthermore, the polarization shifts are are not first order shifts, as implied by Eq. (9), but second order shifts. To understand their approach, it is useful to think of the Ba atom as consisting of an inert, but polarizable Ba^{++} core and two valence electrons. In this case the dipole and quadrupole polarization shifts of the $6sn\ell$ state are due to the dipole and quadrupole couplings of the $6sn\ell$ state to the doubly excited $NLn\ell'$ states. Here NL is the state of Ba^{+}, and $n\ell'$ is the state of the Rydberg electron. The energy shifts are readily calculated in second order perturbation theory by summing the contributions of all the coupled $NLn\ell'$ states, including continua. For example, the quadrupole polarization energy of the Ba $6s20i$ state comes from the quadrupole couplings to doubly excited Ba $Ndn\ell'$ states with ℓ' =4, 6, and 8, as shown schematically in Fig. 18. Summing over all the coupled $Ndn\ell'$ states yields the quadrupole polarization shift. As shown in Fig. 18 for the specific case of $N = 6$, Δ is the energy range

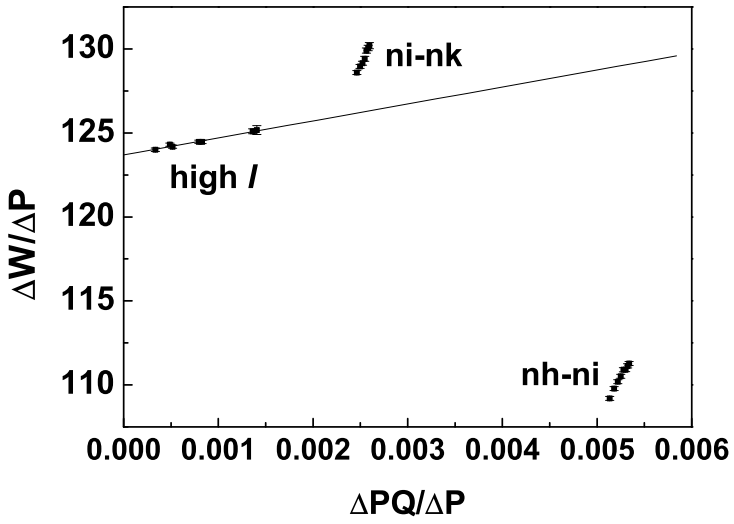

FIG. 17. The adiabatic plot of the measured $\Delta\ell$ intervals using Eq. (13).

spanned by the $n\ell'$ states associated with an Nd ion state, and Ω is the energy difference between the Ba^+ $6s$ and Nd states. If $\Delta \ll \Omega$ for all N, the sum reduces to $\alpha_q\langle r^{-6}\rangle_{20i}/2$, as in Eq. (9). Thus, a more precise statement of the adiabatic requirement is $\Delta \ll \Omega$ for all NL. For the Ba $Ndn\ell'$ states of $N > 5$ the adiabatic requirement is reasonably well satisfied, but for $N = 5$ it is not.

The most important quadrupole couplings by far are those between the $6sn\ell$ and $5dn'\ell'$ states. As an example we consider the $6s20i$ state, which is coupled to the $5dng$, $5dni$, and $5dn\ell$ states. These states are not energetically removed from the $6s20i$ state by the Ba^+ $6s-5d$ interval of ~ 5000 cm^{-1}, as assumed in the adiabatic model, but by a range of energies comparable to the ion interval. In this case $\Delta \cong \Omega$, and the adiabatic model fails, as shown graphically in Fig. 17. Nonetheless, using hydrogenic wavefunctions it is straightforward to calculate the energy shift due to the quadrupole coupling to the $5dn\ell'$ states and compare it to that expected from the adiabatic model, yielding the ratio, or correction factor, k_q. Thus we can write the quadrupole polarization shift of the $6s20i$ states due to the $5dn\ell'$ states as $k_q\alpha'_q\langle r^{-6}\rangle_{20i}/2$, where α'_q is the part of the quadrupole polarizability due to the Ba^+ $5d$ state. An analogous procedure can be carried out for the dipole polarization shift, leading to the correction factor k_d. An important point to keep in mind is that k_d and k_q correct for the

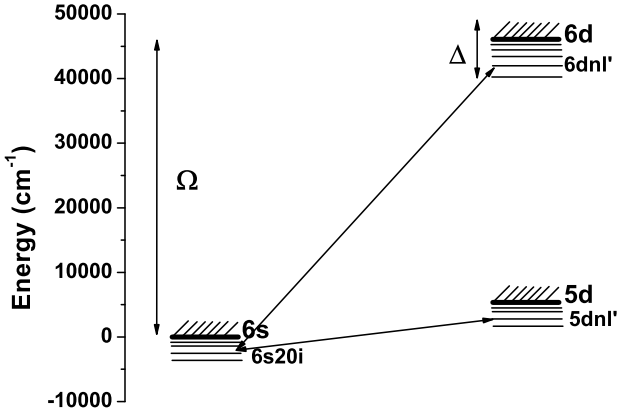

FIG. 18. Energy level diagram showing the quadrupole coupling of the $6s20i$ state to $Ndn\ell'$ states ($\ell' = 4, 6$ and 8). The Ba^+ $6s$ ground state energy is set to zero. Δ is the energy spread of the $n\ell'$ states, and Ω is the $6s - Nd$ ion energy spacing, shown here for $N = 6$. The adiabatic requirement, $\Delta \ll \Omega$, is clearly not satisfied for $N = 5$.

non adiabatic effects in the dipole and quadrupole polarization energy shifts, respectively. They are not corrections to the polarizabilities. Thus, for example, the non adiabatic effect in the dipole polarization energy affects both α_d and α_q.

With the realization that the polarization energy shifts are simply derived from second order perturbation theory we can understand why the $ni - nk$ and $nh - ni$ intervals are displaced as they are in Fig. 17. A $6sni$ state has a very strong quadrupole interaction with the low lying $5d5g$ state which is only ~ 1000 cm^{-1} above the $6sni$ state. For this reason, the quadrupole polarization energy shift is greater than expected from the adiabatic model, and the $ni - nk$ points lie above the line in Fig 17. The $nh - ni$ intervals lie below the line in Fig. 17 because the $6snh$ states have a strong quadrupole interaction with the $5d4f$ state which lies ~ 1000 cm^{-1} below the $6s20h$ state. The quadrupole interaction shifts the $6s20h$ state up in energy, changing the sign of the quadrupole polarization shift.

The high ℓ points in Fig. 17 at $\Delta PQ_{n\ell\ell'}/\Delta P_{n\ell\ell'} < 0.001$ fit a straight line fairly well, and we can extract values for α_d and α_q from the intercept and slope of the line through these points, which we term the apparent polarizabilities. The values we obtain are $\alpha_d^{\rm app}$=123.67(6) a_0^3 and $\alpha_q^{\rm app}$=1047(63) a_0^5. These values are too small, due to neglect of the nonadiabatic corrections, and for this reason we term the extracted values the apparent polarizabilities.

To extract the correct values of α_d and α_q for Ba^+ from the $\Delta\ell$ intervals of the Ba $6sn\ell$ states, we must account for the nonadiabatic effects, which are prominent in Fig. 17. There are several approaches, and we first describe our approach. We start by noting that the contributions to the Ba^+ $6s$ polarizabilities from Ba^+ states above the $6p$ and $5d$ states are essentially adiabatic, as are those from Ba^{++}. We assume the nonadiabatic effects to arise only from the $6p$ and $5d$ states of Ba^+, as done by Snow and Lundeen [23]. Accordingly, we write the analog to Eq. (9) as

$$W_{\mathrm{pol},n\ell} = -\frac{1}{2}(\alpha'_d k_d + \alpha''_d)\langle r^{-4}\rangle_{n\ell} - \frac{1}{2}(\alpha'_q k_q + \alpha''_q)\langle r^{-6}\rangle_{n\ell}, \tag{14}$$

where α'_d is the part of the dipole polarizability due to the $6p$ state of the Ba^+ ion, α'_q is the part of the quadrupole polarizability due to the $5d$ state of the Ba^+ ion, α''_d is the part of the dipole polarizability due to the higher p states of the Ba^+ ion and the dipole polarizability of Ba^{++}, and α''_q is the part of the quadrupole polarizability due to the higher d states of the Ba^+ ion and the quadrupole polarizability of Ba^{++}. The nonadiabatic effects are taken into account by introducing the correction factors k_d and k_q [21, 23]. In principle, the k_d and k_q factors completely eliminate the nonadiabatic effects. It is straightforward to calculate k_d and k_q if we assume the outer electron to be hydrogenic. Our calculated values of k_d are given in Table XI, and to three significant digits there is no n dependence. The n dependent k_q values are presented in Table XII.

TABLE XI. k_d calculated values

n	$\ell=5$	$\ell=6$	$\ell=7$	$\ell=8$	$\ell=9$	$\ell=10$	$\ell=11$
15	0.955278	0.969324	0.979127				
16	0.955326	0.969248	0.978992				
17	0.955494	0.969194	0.978904	0.984568	0.987537	0.989361	
18	0.955404	0.969168	0.978870				
19	0.955470	0.969141	0.978841				
20	0.955510	0.969136	0.978841	0.981743	0.984323	0.985240	0.987553
21	0.955543	0.969128	0.978847				
22	0.955584	0.969126					
23	0.955619						

If we define the quantities $P'_{n\ell}$ and $Q'_{n\ell}$ as follows

$$P'_{n\ell} = k_d P_{n\ell}, \tag{15}$$

and

$$Q'_{n\ell} = \frac{k_q}{k_d} Q_{n\ell}, \tag{16}$$

the energy difference between the ℓ states of the same n can be written as

$$\Delta W_{\mathrm{pol},n\ell'\ell} = \alpha'_d \Delta P'_{n\ell\ell'} + \alpha''_d \Delta P_{n\ell\ell'} + \alpha'_q \Delta P' Q'_{n\ell\ell'} + \alpha''_q \Delta P Q_{n\ell\ell'} \tag{17}$$

where $\Delta W_{\mathrm{pol},n\ell'\ell}$, $\Delta P_{n\ell\ell'}$, and $\Delta P Q_{n\ell\ell'}$ are as defined earlier, $\Delta P'_{n\ell\ell'} = P'_{n\ell} - P'_{n\ell'}$ and $\Delta P' Q'_{n\ell\ell'} = P'_{n\ell} Q'_{n\ell} - P'_{n\ell'} Q'_{n\ell'}$. If we group the α''_d and α''_q terms with the observed energy intervals and divide Eq. (17) by $\Delta P'_{\ell\ell'}$, we obtain the following expression:

$$\frac{\Delta W_{\mathrm{pol},n\ell'\ell} - \alpha''_d \Delta P_{n\ell\ell'} - \alpha''_q \Delta P Q_{n\ell\ell'}}{\Delta P'_{n\ell\ell'}} = \alpha'_d + \alpha'_q \frac{\Delta P' Q'_{n\ell\ell'}}{\Delta P'_{n\ell\ell'}}, \tag{18}$$

which is the nonadiabatic analog of Eq. (13).

If we know α''_d and α''_q, we can extract α'_d and α'_q from their linear relationship with the measured $\Delta\ell$ intervals, using the center of gravity of each $6sn\ell$ state. From Ref. [29], $\alpha''_d = 10.15(53)\ a_0^3$, and $\alpha''_q = 814(11)\ a_0^5$. Fig. 19(a) shows the fit of the experimental data to Eq. (18) using our calculated $\Delta P_{n,\ell\ell'}$, $\Delta P Q_{n,\ell\ell'}$, $\Delta P'_{n,\ell\ell'}$ and $\Delta P' Q'_{n,\ell\ell'}$. In Fig. 11 and in all similar plots, for the $nh - ni$ and $ni - nk$ intervals n increases from 15 to 21 as $\Delta P' Q' / \Delta P'$

TABLE XII. k_q calculated values

n	$\ell = 5$	$\ell = 6$	$\ell = 7$
15	-0.982	1.439	1.032
16	-0.889	1.473	1.039
17	-0.818	1.503	1.044
18	-0.761	1.531	1.050
19	-0.715	1.555	1.054
20	-0.678	1.577	1.058
21	-0.647	1.596	1.061
22	-0.620	1.614	
23	-0.598		

increases. Unlike Fig. 17, the experimental data can be fit reasonably well by a straight line, and from Fig. 19(a), we obtain $\alpha'_d = 114.47(7)\ a_0^3$ and $\alpha'_q = 1725(14)\ a_0^5$. While Fig. 19(a) is an enormous improvement over Fig. 17, the data clearly do not fit the model, as shown by the residuals in Fig. 19(b).

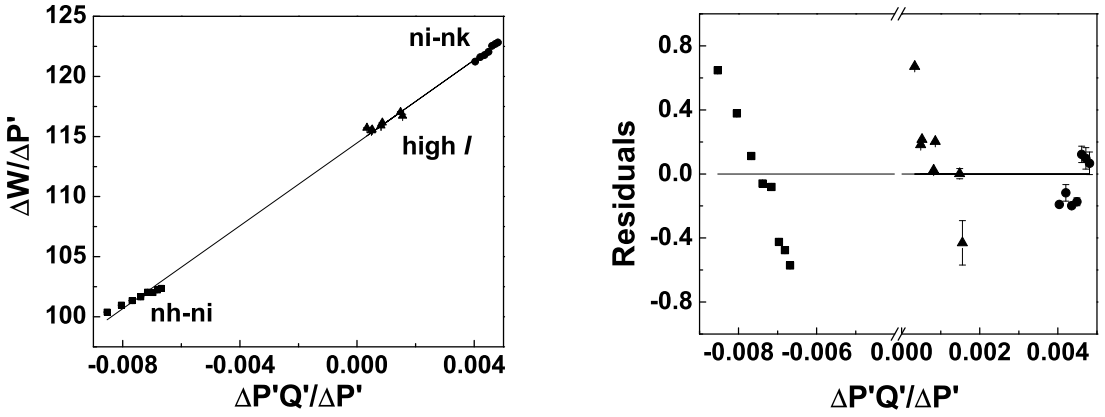

(a) (b)

FIG. 19. (a) Graph of $\frac{\Delta W_{\mathrm{pol},n\ell'\ell} - \alpha''_d \Delta P_{n\ell\ell'} - \alpha''_q \Delta P Q_{n\ell\ell'}}{\Delta P'_{n\ell\ell'}} vs \frac{\Delta P' Q'_{n\ell\ell'}}{\Delta P'_{n\ell\ell'}}$. The symbols ■, •, and ▲ are the data points presenting the $nh - ni$, $ni - nk$ and high ℓ intervals, respectively. For the $nh - ni$ and $ni - nk$ intervals n increases monotonically from 15 to 21 as $\Delta P'Q'/\Delta P'$ increases. The high ℓ intervals are for $n = 17$ and 20. The linear fit yields the y-intercept and the slope which are the values of α'_d and α'_q, respectively. From the graph, we obtain $\alpha'_d = 114.47(7)\ a_0^3$ and $\alpha'_q = 1725(14)\ a_0^5$, and (b) the plot displays the residuals relative to the fit, which is the zero line.

Due to the obvious systematic variations of the residuals, shown in Fig. 19(b), the uncertainties of the values of α'_d and α'_q are larger than the uncertainties from the fit. To understand these uncertainties we have fit the data in other ways. The first is to remove the lower ℓ intervals, which have larger nonadiabatic corrections, from the fit. In Fig. 20(a) we show the fit obtained by removing the $nh - ni$ intervals from Fig. 19(a). The resulting values, $\alpha'_d = 114.66(12)\ a_0^3$ and $\alpha'_q = 1664(36)\ a_0^5$, are not very different from those extracted from Fig. 19(a). The residuals are shown in Fig. 20(b). There are several points to note about Fig. 20(b). First, we note that there is a discontinuity between $n = 18$ and $n = 19$ in the $ni - nk$ points, which may be due to a perturbation of the energy levels, which we

can not hope to fit. Second, we believe the $n = 20$ $\ell = 7 \rightarrow \ell = 8$ and $\ell = 10 \rightarrow \ell = 11$ points to be in error. We shall return to this point. Finally, if the two $n = 20$ points and the discontinuity at $n = 18$ are ignored, the systematic variation of the residuals is essentially gone. If we remove the $ni - nk$ intervals from Fig. 20(a), leaving only the high ℓ intervals from Snow and Lundeen, we obtain the plot of Fig. 21, which yields $\alpha'_d = 115.08(16)\ a_0^3$ and $\alpha'_q = 1160(170)\ a_0^5$. With this restricted set of data the scatter is now clearly more important than any systematic variation. Inspection of the $\ell = 7 \rightarrow \ell = 8$ points of Fig. 13 shows why we believe the $n = 20$ points to be suspect. The two $\ell = 7 \rightarrow \ell = 8$ points by themselves imply an impossible negative quadrupole polarizability, as do the $\ell = 10 \rightarrow \ell = 11$ and either of the $\ell = 9 \rightarrow \ell = 10$ points.

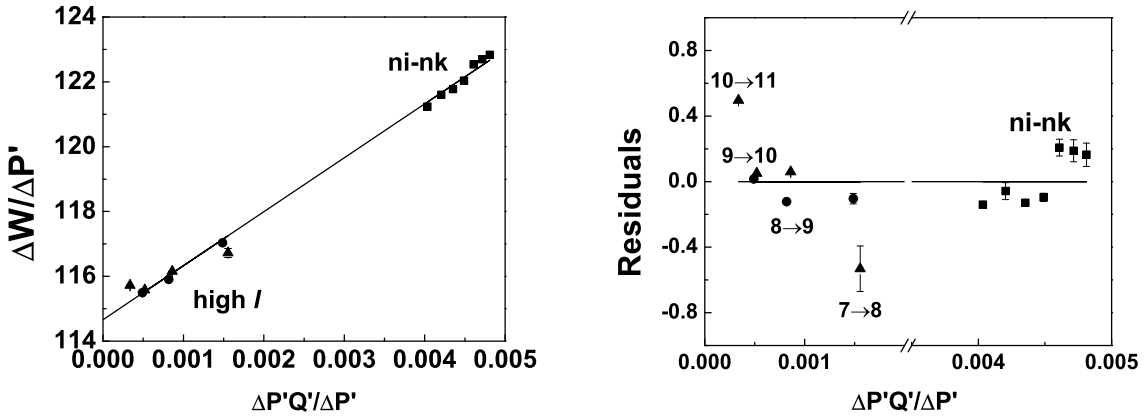

(a) (b)

FIG. 20. (a) Plot obtained by removing the $nh - ni$ intervals from the data in Fig. 19(a). For the $ni - nk$ intervals n increases monotonically from 15 to 21 as $\Delta P'Q'/\Delta P'$ increases. The high ℓ points are for $n = 17$ (•) and $n = 20$ (▲). From the graph, we obtain $\alpha'_d = 114.66(12)\ a_0^3$ and $\alpha'_q = 1664(36)\ a_0^5$. (b) The residuals of (a). There is far less systematic variation of the residuals than in Fig. 19(b).

An alternative approach is to fit the $\Delta\ell$ intervals for each n state separately, and in Fig. 22 we show the values of α'_d and α'_q extracted from the data shown in Fig. 19(a). Only for $n = 17$ and 20 are there more than two $\Delta\ell$ intervals, so only in those two cases can we show uncertainties for the fits. We expect that if we had more points the uncertainties of the other n states would be similar. If we disregard the obvious outliers at $n = 18$ and 21, there is no

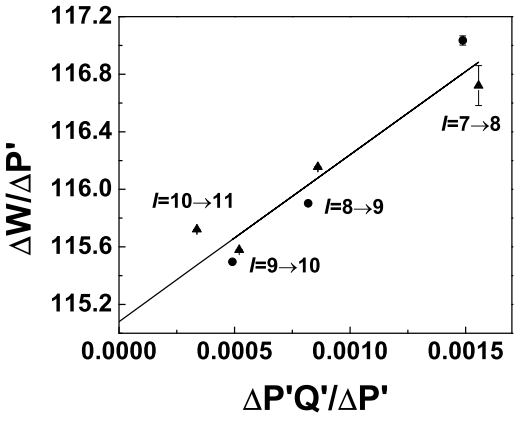

FIG. 21. Plot of high ℓ intervals from Fig. 19(a) for $n = 17$ (•) and $n = 20$ (▲). From the graph, we obtain $\alpha'_d = 115.08(16)\ a_0^3$ and $\alpha'_q = 1160(170)\ a_0^5$.

monotonic increase or decrease in the value of α'_d, and the average value, $\alpha'_d = 114.51(2)\ a_0^3$, is similar to the value extracted from Fig. 19(a). The $n = 18$ intervals were measured in two different experiments, so we do not think the $n = 18$ points are displaced from the others due to an experimental problem, but for a physical reason. As already noted, the $ni - nk$ residuals of Fig. 20(b) exhibit a discontinuity at $n = 18$, which might be a sign of a series perturbation. The $n = 21$ points in Fig. 22 probably reflect experimental error.

In contrast to the relatively constant values of α'_d shown in Fig. 22, the extracted values of α'_q show a clear n dependence, and we suspect that its origin lies in our calculation of k_q, especially for $\ell = 5$. There are several sources of error in calculations of k_d and k_q. We have ignored the spin orbit splittings of the Ba^+ $6p$ and $5d$ states, and we have assumed the outer electron to be hydrogenic. The latter assumption leads to incorrect energies, and more important, incorrect wavefunctions. For this problem, matrix elements of inverse powers of r are required, which in turn requires wavefunctions accurate at small r. Unfortunately, there is no simple method to generate non hydrogenic wavefunctions which are accurate at small r.

Irrespective of the source of the variation in α'_q seen in Fig. 22, it is clear that we can not extract a value of α'_q from these data, and the value of α'_d is also suspect. Accordingly, we have fit the $ni - nk$ and higher ℓ intervals of Fig. 20(a) for $n = 17$ and 20, the only n values

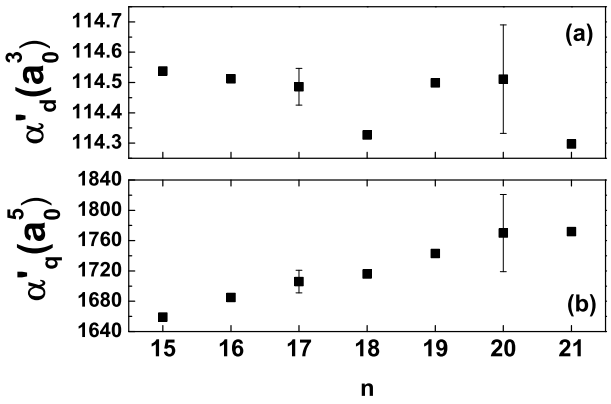

FIG. 22. Graph showing the values of (a) α'_d and (b) α'_q extracted from $\Delta\ell$ intervals for each n. Disregarding the obvious outliers at $n = 18$ and 21, there is no monotonic increase or decrease in the value of α'_d, and the average value is $\alpha'_d = 114.51(2)\ a_0^3$. A value of α'_q cannot be extracted from (b). Only $n = 17$ and 20 have more than two data points (the $nh - ni$, $ni - nk$ and high ℓ intervals), and therefore only their uncertainties can be shown.

for which we have more than one $\Delta\ell$ interval. For $n = 17$ we obtain $\alpha'_d = 114.62(5)\ a_0^3$ and $\alpha'_q = 1640(23)\ a_0^5$, and for $n = 20$ $\alpha'_d = 114.73(27)\ a_0^3$ and $\alpha'_q = 1650(120)\ a_0^5$. The $n = 17$ data lie almost perfectly on a straight line, while the $n = 20$ data are more scattered. The important point is that α'_q exhibits no n dependence. Thus we conclude that the fit of Fig. 20(a) provides the best values for α'_d and α'_d. The high ℓ data shown in Fig 21 exhibit no systematic problem, but the high ℓ intervals are more susceptible to Stark shifts and are not as sensitive to the quadrupole polarizability as are the lower ℓ intervals.

To account for possible systematic effects in the determination of α'_d and α'_q we increase their uncertainties from the fit shown in Fig. 20(a) to encompass the residuals shown in Fig. 20(b) except the two $n = 20$ points mentioned previously. The results are $\alpha'_d = 114.66(25)$ a_0^3 and $\alpha'_q = 1664(50)$. Adding them to α''_d and α''_q to obtain the ionic Ba^+ dipole and quadrupole polarizabilities $\alpha_d = 124.81(25)\ a_0^3$ and $\alpha_q = 2478(50)\ a_0^5$, respectively.

It is useful to compare our values to those obtained from other measurements and theory. In Table XIII we present the values obtained for α_d, and in Table XIV, we present the values for α'_q and α_q. Our value for α_d agrees with the theoretical value to within the

TABLE XIII. The Ba^+ 6s dipole polarizability (α_d) obtained from this work and other theoretical and experimental results.

	α_d (a_0^3)
Core polarization	
This work	124.81(25)
Expt. [21]	125.5(10)
Expt. [23]	124.30(16)
Expt. [11]	123.88(5)
K splitting	
Expt. [8]	121.3(66)
Expt. [28]	123.88(5)
Theory [29]	124.15

theoretical uncertainty, but our value for α_q is half the theoretical value. It is perhaps more interesting to compare the experimental results. Two methods have been used to extract the polarizabilities, polarization analysis of the $\Delta\ell$ intervals and analysis of the K splittings. Analysis of the K splittings yields the Ba^+ $6s-6p$ and $6s-5d$ radial matrix elements, from which α_d' and α_q' are easily computed. To the values of α_d' and α_q' given in ref. [8] we have added the theoretical values $\alpha_d'' = 10.15\ a_0^3$ and $\alpha_q'' = 814\ a_0^5$ yielding the values of α_d and α_q given in Tables XIII and XIV. While it is possible to make good measurements of the K splittings, they arise completely from the nonadiabatic effects, and their analysis is much more complicated than a polarization analysis of $\Delta\ell$ intervals. For this reason, we choose to compare our results to those of Snow and Lundeen, ref. [11].

Using essentially the same data as we have used here, Snow and Lundeen [11] arrived at a value of α_d distinctly smaller than ours and a value of α_q almost twice ours. To understand the origin of the differences it is useful to use four different methods to analyze the data. Specifically, we consider ignoring the non adiabatic effects, using the adiabatic expansion method, introducing k_q and using the adiabatic expansion method to account for nonadiabatic effect in the dipole polarization energy, and finally introducing both k_q and k_d. For simplicity, we label these methods I, II, III, and IV, respectively. Method III is similar to that used by Snow and Lundeen, and IV is similar to ours.

TABLE XIV. The Ba^+ 6s quadrupole polarizability (α_q) and the contribution of the Ba^+ 5d state (α'_q) to it.

	α'_q (a_0^5)	α_q (a_0^5)
Core polarization		
This work	1664(50)	2478(50)
Expt. [21]		2050(100)
Expt. [11]	1524(8)	4420(250)
Expt. [23]	1828(88)	2462(361)
K splitting		
Expt. [8]	1562(93)	2376(93)
Expt. [28]	3606(250)	4420(250)
Theory [29]	3368(34)	4182(34)

If we restrict our attention to only the high ℓ intervals, it is not unreasonable to think that the data can be fit by ignoring the non adiabatic effects, method I, and using Eq. (13). The straight line through the high ℓ points of Fig. 17 is precisely this fit. It yields $\alpha_d = \alpha_d^{app} = 123.67$ a_0^3 and $\alpha_q = \alpha_q^{app} = 1047$ a_0^5.

In the adiabatic expansion method, method II, the polarization energy of Eq. (9) is replaced by

$$W_{\mathrm{pol},n\ell} = -\frac{1}{2}\alpha_d\langle r^{-4}\rangle_{n\ell} - \frac{1}{2}(\alpha_q - 6\beta_1)\langle r^{-6}\rangle_{n\ell}...., \tag{19}$$

where the ellipsis indicates terms containing expectation values of higher inverse powers of r. The most important difference, from our present point of view, is the presence of $6\beta_1$ in the $\langle r^{-6}\rangle$ term, which is due to the non adiabatic effect in the dipole polarization energy. It appears in the same way as the quadrupole polarizability, and for Ba $\beta_1 = 605(25)$ a_0^5. The higher inverse powers of r represent higher order terms due to the nonadiabatic effect in the dipole polarization energy, the nonadiabatic effect in the quadrupole polarization energy, and higher multipole terms. As Snow and Lundeen have shown, these terms can be represented by higher order terms in $\langle r^{-6}\rangle/\langle r^{-4}\rangle$, or equivalently, in $\Delta PQ/\Delta P$, so that the data points of Fig. 17 no longer need to be fit by a straight line. Application of the adiabatic expansion method is based on the assumption that the expansion is convergent. Inspection of Fig. 17 suggests that very high order terms in $\Delta PQ/\Delta P$ will be required to

fit the data, indicating that the adiabatic expansion is almost certainly not convergent in this case. However, it should be applicable if we again restrict our attention to the high ℓ states. Fitting the high ℓ data of Fig. 17 to the first two terms of Eq. (19) leads to $\alpha_d = \alpha_d^{app} = 123.67$ a_0^3 and $\alpha_q = \alpha_q^{app} + 6\beta_1 = 4677$ a_0^5.

The deviation of the factors k_d and k_q from unity is an indication of the severity of the nonadiabatic effects. Inspection of Tables XI and XII shows that $0.955 < k_d < 0.990$ while k_q ranges from -.0982 to 1.614, suggesting that the non adiabatic effect in the quadrupole polarization energy is by far the worse problem. Accordingly, we treat the data using method III, treating the non adiabatic effects in the quadrupole and dipole polarization energies by k_q and an adiabatic expansion, respectively. This approach is approximately that used by Snow and Lundeen. It differs in that Snow and Lundeen, and we as well, separated the polarizabilities into two parts, for example $\alpha_q = \alpha_q' + \alpha_q''$. To display most clearly the effect of introducing first k_q and then k_d we here assume that α_d'' and α_q'' both vanish, so that $\alpha_d' = \alpha_d$ and $\alpha_q' = \alpha_q$. Since $\alpha_d' = 0.92\alpha_d$, this approximation is excellent for α_d, and it is not unreasonable for α_q. In Fig. 23 using solid circles (•) we use method III to plot the high ℓ and $ni - nk$ intervals using the values of k_q given in Table XII. Since we are now introducing k_q, and later shall introduce k_d, as the horizontal and vertical axes we use $\Delta P' Q'_{n\ell'\ell}/\Delta P'_{n\ell\ell}$ and $\Delta W_{pol,n\ell'\ell}/\Delta P'_{n\ell\ell'}$. From the definitions of P' and Q' it is evident that P and Q are simply the special cases of P' and Q' for $k_d = k_q = 1$. The dominant effect of the introduction of k_q is to move points horizontally on the plot, which removes the glaring problem due to the non adiabatic effects, the seemingly random distribution of points in Fig. 17. Now in Fig. 23 the solid circles (•) all line along a straight line. In method III the adiabatic expansion only needs to account for the nonadiabatic effect on the dipole polarization. Accordingly, we fit the solid circles (•) to

$$\frac{\Delta W_{\mathrm{pol},n\ell'\ell}}{\Delta P'_{n\ell\ell'}} = \alpha_d + (\alpha_q - 6\beta_1)\frac{\Delta P' Q'_{n\ell\ell'}}{\Delta P'_{n\ell\ell'}}. \tag{20}$$

The intercept of the fit line is $\alpha_d = 123.33(11)$ a_0^3, and the slope $s_q = 1430(35)$ a_0^5. The quadrupole polarizability, $\alpha_q = s_q + 6\beta_1 = 5060$ a_0^5, is the slope of the broken line in Fig. 23.

To show the effect of using k_d as well as k_q, method IV, in Fig. 23 we also plot, as solid squares (■), the high ℓ and $ni - nk$ intervals. The introduction of k_d has two effects, both of which are evident in Fig. 23. First, it raises all the points by 1-3%, since $k_d < 1$ and $\Delta P' < \Delta P$. The effect is to raise the value of α_d; $\alpha_d = 125.28(8)$ a_0^3. Second, since

TABLE XV. The Ba^+ 6s dipole (α_d) and quadrupole polarizabilities (α_q) extracted from different methods of data analysis.

Analysis method	α_d (a_0^3)	α_q (a_0^5)
Method I: ignore non adiabatic	123.67(6)	1047(63)
Method II: adiabatic expansion	123.67(6)	4680(160)
Method III: k_q and adiabatic expansion	123.33(11)	5060(150)
Method IV: k_d and k_q	125.28(8)	2138(23)
Snow and Lundeen [11]	123.88(5)	4420(250)
This work	124.81(25)	2478(50)

k_d falls further below one as ℓ is decreased, the slope of the line through the points is increased. In this method the slope (of the line through the square points) is $\alpha_q = 2138(23)$ a_0^5. The nonadiabatic effect in the dipole polarization energy on α_q is the difference between the slopes of the lines through the squares and circles in Fig. 23, 708 a_0^5, much less than $6\beta_1 = 3630$ a_0^5.

In Table XV we have collected the results from the four analyses and presented them together with the values of Snow and Lundeen and ourselves. Methods I, II, and III yield essentially the same value of α_d, which implies that the adiabatic expansion method, or a modification which does not introduce k_d, has almost no effect on the value of α_d extracted. These values are also very close to the value obtained by Snow and Lundeen. The introduction of k_d, in method IV, vertically displaces the points in Fig. 23 and increases the value of α_d extracted to very nearly match our value. The quadrupole polarizabilities extracted by methods II and III are both much larger than those obtained by methods I and IV, due to the inclusion of $6\beta_1$ in the extracted value. These values are close to the value obtained by Snow and Lundeen. Method IV yields a value of α_q similar to our value and much smaller than methods II and III. From Table XV it is evident that the difference between the values of both α_d and α_q extracted by Snow and Lundeen and ourselves is due almost entirely to the treatment of the non adiabatic effect in the dipole polarization.

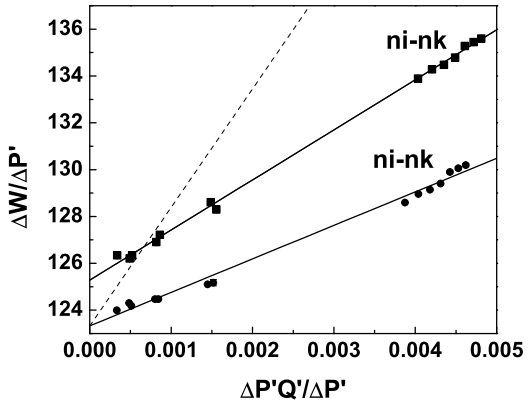

FIG. 23. Comparison between the use of method III to treat the $ni - nk$ and the high ℓ intervals (•) and method IV to treat the intervals (■). Here we assume α_d'' and α_q'' both vanish. The introduction of k_q in method III removes the nonadiabatic effect in the quadrupole polarization energy, and all the data points fall on a line, unlike the plot of Fig. 9. The intercept of the fit line gives $\alpha_d = 123.33(11)$ a_0^3. Adding $6\beta_1$ from the nonadiabatic correction to the dipole polarization energy to the slope of the fit line give the broken line, which has slope $\alpha_q = 5060$ a_0^5. The introduction of k_d as well as k_q in method IV both raises the points and increases the slope of the fit line. the resulting intercept and slope are $\alpha_d = 125.28(8)$ a_0^3 and $\alpha_q = 2138(24)$ a_0^5.

A. Conclusion

We have demonstrated that ICE laser excitation to autoionizing states can be used to detect microwave transitions between high angular momentum Rydberg states of alkaline-earth atoms, even though the ICE transitions are badly overlapped. We have used this technique to measure $\Delta\ell$ intervals between Ba $6sn\ell$ states of $15 \leq n \leq 18$ and $5 \leq \ell \leq 7$. Combining these measurements with other measurements of Ba $\Delta\ell$ intervals, we have extracted the Ba^+ polarizabilities $\alpha_d = 124.81(25)$ a_0^3 and $\alpha_q = 2478(50)$ a_0^5. These values disagree with recently reported experimental values due to the difference in the treatment of the nonadiabatic effects. In principle, the model we have used exactly accounts for the nonadiabatic effects by the introduction of the correction factors k_d and k_q, which are calculated numerically. The calculations can be improved by better numerical techniques, the inclusion of spin-orbit coupling, and the use of non hydrogenic wavefunctions where

required. We hope this work will stimulate theoretical activity along these lines.

---

[1] G. Vitrant, J. M. Raimond, M. Gross, and S. Haroche, J. Phys. B: At. Mol. Phys. 15, L49 (1982).

[2] J. H. Van Vleck and N. G. Whitelaw, Phys. Rev. **44**, 551 (1933).

[3] J. E. Mayer and M. G. Mayer, Phys. Rev. **43**, 605 (1933).

[4] B. Edlen in Handbuch der Physik (Springer, Berlin, 1964).

[5] S. R. Lundeen, in Advances in Atomic, Molecular, and Optical Physics, P. R. Berman and C. C. Lin eds, vol. 52 (Academic Press, New York, 2005).

[6] A. G. Vaidyanathan, W. P. Spencer, J. R. Rubbmark, H. Kuiper, C. Fabre, D. Kleppner, and T. W. Ducas, Phys. Rev. A **26**, 3346 (1982).

[7] E. S. Shuman, J. Nunkaew and T. F. Gallagher, Phys. Rev. A **75**, 044501 (2007).

[8] E. S. Shuman and T. F. Gallagher, Phys. Rev. A **74**, 022502 (2006).

[9] E. L. Snow, R. A. Komara, M. A. Gearba, and S. R. Lundeen, Phys. Rev. A **68**, 022510 (2003).

[10] Thomas R. Gentile, Barbara J. Hughey, Daniel Kleppner and Theodore W. Ducas, Phys. Rev. A **42**, 440 (1990).

[11] E. L. Snow, and S. R. Lundeen, Phys. Rev. A **76**, 052505 (2007).

[12] M. S. Safronova, and U. I. Safronova, Phys. Rev. A **83**, 012503 (2011).

[13] T. F. Gallagher, *Rydberg Atoms* (Cambridge University Press, Cambridge, England, 1994).

[14] E. S. Chang, J. Phys. B: At. Mol. Phys. **16**, L539 (1983).

[15] C. E. Theodosiou, L. J. Curtis, and C. A. Nicolaides, Phys. Rev. A **52**, 3677 (1995).

[16] J. Mitroy and J. Y. Zhang, Eur. Phys. J. D **46**, 415-424 (2008).

[17] B. K. Sahoo, B. P. Das, and D. Mukherjee, Phys. Rev. A **79**, 052511 (2009).

[18] J. Nunkaew and T. F. Gallagher, Phys. Rev. A **91**, 042503 (2015).

[19] E. G. Kim, J. Nunkaew, and T. F. Gallagher, Phys. Rev. A **89**, 062503 (2014).

[20] M. Chwalla, J. Benhelm, K. Kim, G. Kirchmair, T. Monz, M. Riebe, P. Schindler, A. S. Villar, W. Hänsel, C. F. Roos, R. Blatt, M. Abgrall, G. Santarelli, G. D. Rovera, and Ph. Laurent, Phys. Rev. Lett. **102**, 023002 (2009).

[21] T. F. Gallagher, R. Kachru, and N. H. Tran, Phys. Rev. A **26**, 2611 (1982).

[22] E. L. Snow and S. R. Lundeen, Phys. Rev. A **77**, 052501 (2008).

[23] E. L. Snow, M. A. Gearba, R. A. Komara, S. R. Lundeen, and W. G. Sturrus, Phys. Rev. A **71**, 022510 (2005).

[24] W. E. Cooke, T. F. Gallagher, S. A. Edelstein, and R. M. Hill, Phys. Rev. Lett. **40**, 178 (1978).

[25] W. E. Cooke and T. F. Gallagher, Opt. Lett. **4**, 173 (1979).

[26] J. Nunkaew and T. F. Gallagher, Phys. Rev. A **81**, 023417 (2010).

[27] R. R. Jones and T. F. Gallagher, Phys. Rev. A **38**, 2846 (1988).

[28] Shannon L. Woods, S. R. Lundeen, and Erica L. Snow, Phys. Rev. A **80**, 042516 (2009).

[29] E. Iskrenova-Tchoukova, and M. S. Safronova, Phys. Rev. A **78**, 012508 (2008).

[30] Shannon L. Woods, M. E. Hanni, S. R. Lundeen, and Erica L. Snow , Phys. Rev. A **82**, 012506 (2010).

Output จากโครงการวิจัยที่ได้รับทุนจาก สกว.

1. ผลงานตีพิมพ์ในวารสารวิชาการนานาชาติ

   - J. Nunkaew* and T. F. Gallagher, “Microwave spectroscopy of the calcium 4*snf* → 4*s*(*n*+1)*d*, 4*sng*, 4*snh*, 4*sni*, and 4*snk* transitions”, Phys. Rev. A **91**, 042503 (2015). (Impact factor 2013 = 2.991)
   - E. G. Kim, J. Nunkaew*, and T. F. Gallagher, “ Detection of barium 6*sng* → 6*snh*, 6*sni*, and 6*snk* microwave transitions using selective excitation to autoionizing states”, Phys. Rev. A 89, 062503 (2014). (Impact factor 2013 = 2.991)

*Corresponding author

**ผลงานตีพิมพ์ดังแนบในภาคผนวก

2. การนำผลงานวิจัยไปใช้ประโยชน์
   - เชิงพาณิชย์
     ไม่มี
   - เชิงนโยบาย
     ไม่มี
   - เชิงสาธารณะ
   - ไม่มี
   - เชิงวิชาการ (มีการพัฒนาการเรียนการสอน/สร้างนักวิจัยใหม่)
     ผลจากการทดลองใช้ในการยืนยันการคำนวณความคลาดเคลื่อนของนาฬิกาอะตอม (Atomic clock) ที่เกิดจาก Blackbody radiation shift

3. อื่นๆ (เช่น ผลงานตีพิมพ์ในวารสารวิชาการในประเทศ การเสนอผลงานในที่ประชุมวิชาการ หนังสือ การจดสิทธิบัตร)

- J. Nunkaew, E. G. Kim and T. F. Gallagher, " Detection of barium 6*sng* → 6*snh*, 6*sni*, and 6*snk* microwave transitions using selective excitation to autoionizing states", 45th Annual Meeting of the American Physical Society Division of Atomic, Molecular and Optical Physics, Madison, WI, USA June 2 - June 6, 2014. (Oral presentation).

- J. Nunkaew and T. F. Gallagher, "Microwave spectroscopy of the calcium 4*snf* → 4*s*(*n*+1)*d*, 4*sng*, 4*snh*, 4*sni*, and 4*snk* transitions", 46th Annual Meeting of the American Physical Society Division of Atomic, Molecular and Optical Physics, Columbus, OH, USA June 8 - June 12, 2015. (Oral presentation).

ภาคผนวก

Detection of barium 6*sng* → 6*snh*, 6*sni*, and 6*snk* microwave transitions using selective excitation to autoionizing states

E. G. Kim,[1] J. Nunkaew,[2,*] and T. F. Gallagher[1]

[1]*Department of Physics, University of Virginia, Charlottesville, Virginia 22904, USA*

[2]*Department of Physics and Materials Science, Faculty of Science, Chiang Mai University, Chiang Mai 50200, Thailand*

(Received 4 October 2013; revised manuscript received 9 April 2014; published 5 June 2014)

We use selective laser excitation to an autoionizing state to observe the microwave transitions of Ba from the 6*sng* Rydberg states to the 6*snh*, 6*sni*, and 6*snk* states for $15 \leqslant n \leqslant 18$. We extract the dipole and quadrupole polarizabilities of Ba^+ from the measured $\Delta\ell$ intervals of the Ba 6*sn*ℓ states of $\ell \geqslant 5$ using a nonadiabatic core polarization model. The values we determine for the dipole and quadrupole polarizabilities are $\alpha_d = 124.81(25)a_0^3$ and $\alpha_q = 2478(50)a_0^5$, respectively.

DOI: 10.1103/PhysRevA.89.062503 PACS number(s): 32.10.Dk, 32.80.Zb, 32.80.Ee

I. INTRODUCTION

One of the largest frequency shifts in present-day atomic clocks is the blackbody radiation shift [1–4]. Since 300 K blackbody radiation is low in frequency, the blackbody shift is predominantly determined by the static polarizability of the atom or ion used in the clock. For many alkaline-earth-metal ions used in atomic clocks, there are no measurements of the ionic dipole and quadrupole polarizabilities to serve as benchmarks for calculations of the blackbody shifts. It is possible to extract these polarizabilities from the intervals between high-ℓ Rydberg states of the atom, states of high enough ℓ that the Rydberg electron does not penetrate the ionic core [5–8]. We follow the usual convention that n and ℓ are the principal and orbital angular momentum quantum numbers of the Rydberg electron. In these nonpenetrating states, the energy shifts from the hydrogenic levels arise from polarization of the core by the field from the Rydberg electron. In Rydberg states of lower ℓ, the electron comes closer to the core at the inner turning point of its orbit, and the energy shift is larger. Thus, measuring the $\Delta\ell$ intervals yields the polarizabilities of the ionic core. An excellent recent summary of core polarization analysis has been given by Lundeen [8].

Several methods have been employed to detect transitions between the high-ℓ states of alkaline-earth-metal atoms. Selective field ionization has been used by Gentile *et al.* to measure the 4*sn*ℓ intervals in Ca [9]. Gallagher *et al.* and Nunkaew *et al.* have used delayed field ionization to detect the Ba 6*sn*ℓ and Sr 5*sn*ℓ intervals [10,11]. Snow and Lundeen have used resonant excitation Stark ionization spectroscopy (RESIS) to measure the Ba 6*sn*ℓ and Mg 3*sn*ℓ intervals [12,13]. Field ionization is useful for states of $n \sim 20$, and RESIS can be used for states which can be populated by driving transitions from $n = 9$ and 10 using a CO_2 laser. Here we point out that the optical excitation to an autoionizing state by isolated core excitation (ICE) can be used to detect $\Delta\ell$ intervals of alkaline-earth-metal atoms over a much wider range of n [14]. The basis of this notion is that the rapid increase in the ICE cross section with ℓ allows the microwave $\Delta\ell$ transitions between the bound states to be detected, even when the ICE transitions for different ℓ states occur at essentially the same wavelength. Here we report the use of this technique to measure the Ba 6*sng*-6*snh*-6*sni*-6*snk* intervals for $15 \leqslant n \leqslant 18$. This technique should be applicable for all Ba states of $n \leqslant 30$.

II. THE MICROWAVE $\Delta\ell$ TRANSITIONS AND THEIR DETECTION USING ICE

The $\Delta\ell$ microwave transitions we observe are shown in Fig. 1. The 6*sng* $^1G_4$ state is populated by laser excitation, and we drive the microwave transitions to the 6*sn*ℓ states of $5 \leqslant \ell \leqslant 7$. The higher-$\ell$ states are not singlets and triplets. Rather, the total angular momentum of the core $\vec{j}_c$ is coupled to the orbital angular momentum $\vec{\ell}$ of the Rydberg electron to form $\vec{K}$. Explicitly,

$$\vec{K} = \vec{j}_c + \vec{\ell}. \tag{1}$$

We ignore the spin of the Rydberg electron. Since $j_c = 1/2$, $K = \ell \pm 1/2$, and for each ℓ state we observe two transitions, as shown in Fig. 1. The splitting between the two K levels is due to the indirect spin-orbit splitting [15,16].

Detection of the Ba 6*sn*$\ell \rightarrow$ 6*sn*ℓ' transitions ($\ell' > \ell$) is based on the difference in the optical cross sections of the 6*sn*$\ell \rightarrow 6p_{1/2}n\ell$ and 6*sn*$\ell' \rightarrow 6p_{1/2}n\ell'$ ICE transitions. Previously, Cooke and Gallagher used the substantial difference in the wavelengths of the Sr 5*snd* → 5*pnd* and 5*snf* → 5*pnf* ICE transitions to detect the Sr $5s(n+2)d \rightarrow 5snf$ microwave transitions [17]. In ICE of the 6*sn*ℓ state, the 6*s* electron absorbs the photon while the $n\ell$ electron is a spectator. The $6s \rightarrow 6p_{1/2}$ transition of the inner electron is essentially the Ba^+ $6s \rightarrow 6p_{1/2}$ transition, with an oscillator strength of 1/3. The oscillator strength is spread over the spectral width of the $6p_{1/2}n\ell$ state, which is determined by its autoionization rate. In this case, the peak optical cross section is given by

$$\sigma_{\text{peak}} = \frac{\lambda^2 A}{8\pi\Gamma_{n\ell}}, \tag{2}$$

where A is the Einstein A coefficient for the Ba^+ $6s \rightarrow 6p_{1/2}$ transition, $\Gamma_{n\ell}$ is the autoionization rate of the $6p_{1/2}n\ell$ state, and λ is the wavelength of the transition, 493.5 nm in this case. We have implicitly assumed that the autoionization rates of the $6p_{1/2}n\ell$ states exceed their radiative decay rates, which is in all cases simply the radiative decay rate of the Ba^+ $6p_{1/2}$ state.

*jn8h@virginia.edu

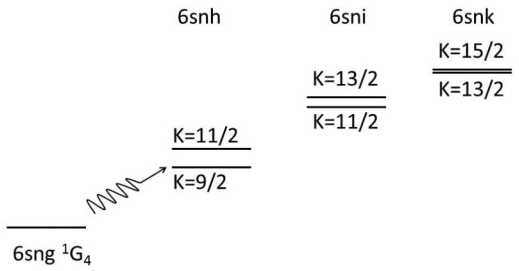

FIG. 1. The Ba $6s n\ell$, $\ell \geqslant 4$, states showing the microwave transitions and the K splittings due to the indirect spin-orbit coupling of the $6s n\ell$, $\ell \geqslant 5$, Rydberg states.

For the $6p_{1/2}n\ell$ states of interest this condition is easily met. However, for $n \geqslant 30$ the autoionization rate of a $6p_{1/2}n\ell$ state of $\ell = 7$ is less than the radiative decay rate, and this method of detection will no longer work [18].

The autoionization rates of the Ba $6p_{1/2}n\ell$ states of $\ell \geqslant 4$ decrease by roughly a factor of 5 with each increase in ℓ of 1 [19]. Accordingly, the cross section for the $6sn\ell \rightarrow 6p_{1/2}n\ell$ ICE transition increases by a factor of 5 for each increase in ℓ of 1. Even if the center frequencies of the ICE transitions are the same, approximately the ionic $6s \rightarrow 6p_{1/2}$ frequency, it is possible to observe transitions between the $6sn\ell$ and $6sn\ell'$ states, as shown in Fig. 2. Figure 2 is drawn assuming the two ICE transitions occur at the ionic frequency and that $\ell' = \ell + 1$, so the ICE cross sections and widths differ by a factor of 5. The linewidth of the laser driving the ICE transition must be less than the width of the $6p_{1/2}n\ell$ state, and the power of the laser must also be kept below saturation of the $6sn\ell' \rightarrow 6p_{1/2}n\ell'$ transition. If the laser linewidth is less than the $6p_{1/2}n\ell'$ linewidth and the $6sn\ell' \rightarrow 6p_{1/2}n\ell'$ transition is not saturated, an atom in the $6sn\ell'$ state is five times as likely as one in the $6sn\ell$ state to undergo the ICE transition when the ICE laser is tuned to the peak of the cross sections, at the ionic frequency. In short, with the ICE laser tuned to the peak of the cross sections, driving the $6sn\ell \rightarrow 6sn\ell'$ microwave transition can result in a fivefold increase in the autoionization signal at the $6sn\ell$-$6sn\ell'$ microwave resonance. Alternatively, the ICE laser can be tuned to the wing of the $6sn\ell \rightarrow 6p_{1/2}n\ell$ transition, in which case the microwave $6sn\ell \rightarrow 6sn\ell'$ transition results in a decrease in the autoionization signal.

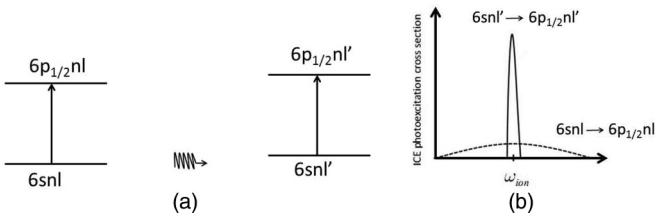

FIG. 2. (a) The $6sn\ell \rightarrow 6sn\ell'$ microwave transition can be detected using the difference in the two ICE cross sections. (b) The ICE cross sections of the $6sn\ell \rightarrow 6p_{1/2}n\ell$ and $6sn\ell' \rightarrow 6p_{1/2}n\ell'$ transitions. With the ICE laser tuned to the peak of the cross sections, driving the $6sn\ell \rightarrow 6sn\ell'$ microwave transition can result in a fivefold increase in the autoionization signal at the $6sn\ell$-$6sn\ell'$ microwave resonance if $\ell' = \ell + 1$.

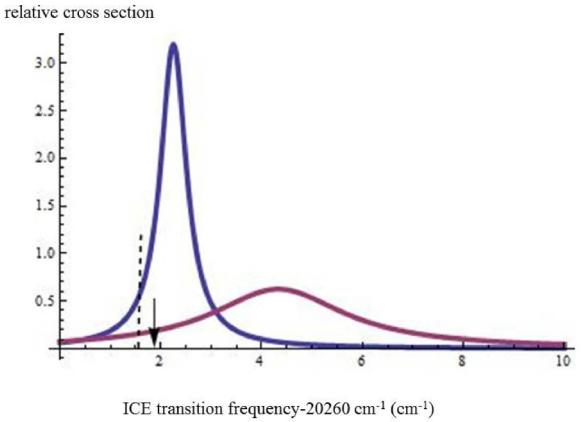

FIG. 3. (Color online) The ICE cross sections for the $6s17g$ and $6s17h$ states. The wider ICE cross section is the $6s17g \rightarrow 6p_{1/2}17g$ transition. The narrower ICE cross section is the $6s17h \rightarrow 6p_{1/2}17h$ transition. The arrow shows the location of the $6s17i \rightarrow 6p_{1/2}17i$ ICE transition. The dashed line shows the location of the ionic $6s \rightarrow 6p_{1/2}$ transition frequency.

In Ba, the $6sn\ell \rightarrow 6p_{1/2}n\ell$ transition frequencies depend on both n and ℓ. Figure 3 shows the ℓ dependence of the $6s17\ell \rightarrow 6p_{1/2}17\ell$, $\ell = 4$ and 5, ICE cross sections. We do not show the $6s17\ell \rightarrow 6p_{1/2}17\ell$ ICE cross sections for $\ell > 5$ since the peak cross sections are so much higher. We do, however, show the location of the $\ell = 6$ ICE transition. The higher-ℓ ICE transitions lie closer to the ion $6s$-$6p_{1/2}$ transition at 20 261.56 cm^{-1}. Since the $6s17g$ and $6s17h$ ICE transitions are not superimposed, at the peak of the $6s17h$ ICE transition the ratio of the cross sections is not 5, but 10. While the increased selectivity is attractive, the displacement of the ICE transitions with ℓ does complicate finding the ICE transitions for higher-ℓ states. In this case the most straightforward approach might be to set the ICE laser to the high-frequency side of the $6s17g \rightarrow 6p_{1/2}17g$ transition and look for a decrease in the autoionization signal to detect the $6s17g \rightarrow 6s17\ell$ microwave transitions. However, we have used a different approach. Since the frequencies of the transitions from the Ba $6s18g$ state to the $6s18h$, $6s18i$, and $6s18k$ states are known [10], we set the microwave frequency to the $6s18g \rightarrow 6s18\ell$ resonance and scanned the ICE laser to find the $6s18\ell \rightarrow 6p_{1/2}18\ell$ ICE transition, which occurs at the frequency ν_ℓ, given by

$$\nu_\ell = \nu_{\rm ion} + \frac{\delta_{\ell_s} - \delta_{\ell_p}}{n^3}, \tag{3}$$

where $\nu_{\rm ion}$ is the Ba^+ $6s$-$6p_{1/2}$ frequency, and δ_{ℓ_s} and δ_{ℓ_p} are the quantum defects of the $6sn\ell$ and $6p_{1/2}n\ell$ states, respectively. When n is decreased by 1 the change in the ICE frequency, $\Delta\nu_\ell$, is given by

$$\Delta\nu_\ell = 3\frac{\delta_{\ell_s} - \delta_{\ell_p}}{n^4}. \tag{4}$$

For $n = 18$ and $\ell = 5$, $\Delta\nu_\ell = 2.5$ GHz, which is small compared to the 10 GHz width of the $6p_{1/2}18h$ state. In short, knowing the $\ell = 5$, 6, and 7 ICE frequencies for $n = 18$ allows us to predict them accurately enough to make the $n = 17$, 16, and 15 measurements.

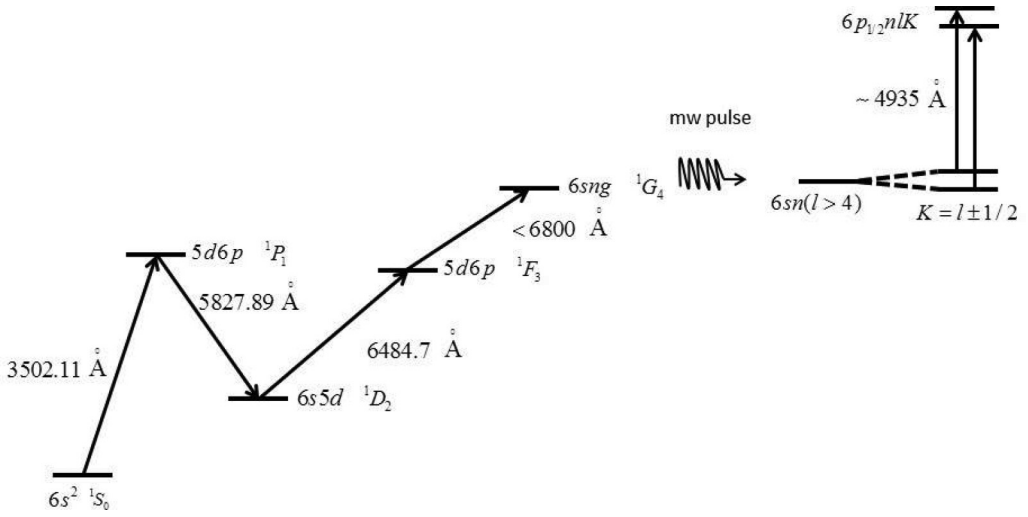

FIG. 4. Laser excitation scheme of the experiment.

III. EXPERIMENTAL APPROACH

We prepare $6sng$ barium Rydberg states by exciting neutral barium atoms in a beam with four laser pulses. The excitation scheme from the ground state $6s^2$ to the $6sng$ state is shown in Fig. 4. Photoions and electrons are produced, so the excitation is performed in a small electric field, less than 100 V/cm, to remove them.

As shown by the timing diagram of Fig. 5 after the four laser pulses, we turn off the electric field and wait 200 ns for any ringing from the electronics to dissipate. It is important that there be no stray electric field on the Rydberg atoms during the microwave pulse to avoid Stark shifts of our observed intervals. To drive the $6sng \rightarrow 6snh$ and $6sng \rightarrow 6sni$ transitions, we apply a single 1 μs pulse of microwaves; while for the $6sng \rightarrow 6snk$ transitions, we use a continuous radio-frequency (rf) field in addition to a 1 μs microwave pulse. When the microwave pulse ends, we immediately apply a ~493.5 nm frequency-doubled, dye-amplified diode laser pulse, which excites the $6sn\ell$ atoms to the autoionizing $6p_{1/2}n\ell$ states. The $6p_{1/2}n\ell$ atoms autoionize quickly, and we apply an electric field ramp to drive the resulting ions to the microchannel plate detector. The peak of the field ramp is high enough to ionize bound $6sn\ell$ atoms of $n > 16$, but the signal from bound-state atoms arrives 1 μs later than the signal from autoionizing atoms. The two signals are temporally well resolved, and we set the gate of the gated integrator on the autoionization signal. This excitation and detection cycle is repeated every 50 ms, and our signals are averaged over many laser shots.

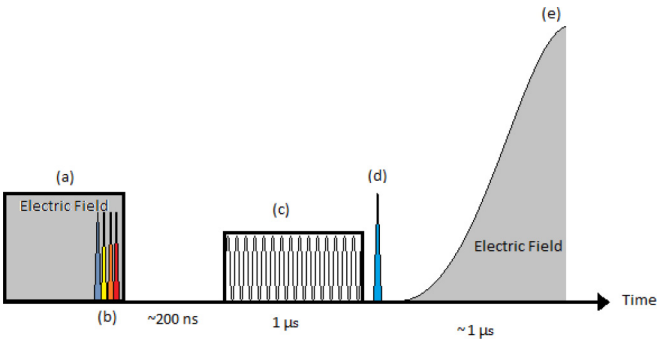

FIG. 5. (Color online) The timing sequence for the lasers, microwaves, and rf signals. (a) Small electric field to clear photoions. (b) Four laser pulses to drive the $6s^2 \rightarrow 6sng$ transition. (c) 1 μs microwave pulse. (d) ICE laser pulse (e) Electric field ramp.

IV. EXPERIMENTAL OBSERVATIONS

A. One-photon intervals

To obtain the single-photon intervals, we started from the known $6s18g$-$6s18h$ transition. We used a high microwave power at the $6s18g$-$6s18h$ resonance to equilibrate the populations, and we swept the diode laser frequency to find the frequency of the $6s18h \rightarrow 6p_{1/2}18h$ ICE transition. With the laser set to the ICE frequency we then attenuated the microwave power and scanned the microwave frequency to repeat the earlier measurements. To find the $6sng$-$6snh$ transitions of $n < 18$, we changed the diode laser frequency from its $n = 18$ value using Eq. (3) and scanned the microwave frequency at high power to find a small resonance signal. We then optimized the signal by adjusting the diode laser frequency with the microwave frequency set to the $6sng$-$6snh$ frequency. Once we found the optimal diode laser frequency, we performed our microwave scans at reduced microwave power.

Typical resonances, for $n = 15$, are shown in Fig. 6. There are two resonances, corresponding to the two possible values of K for the $6s15h$ state. The one-photon transition frequencies for $6sng$ to $6snh$, $15 \leqslant n \leqslant 18$, are shown in Table I.

TABLE I. ng-nh observed frequencies and K splittings.

n	$K = 9/2$ (MHz)	$K = 11/2$ (MHz)	K splitting (MHz)
18	40180.0(6)	41147.4(7)	967.4(9)
17	47367.4(6)	48547.2(6)	1179.8(8)
16	56489.4(6)	57959.0(5)	1469.6(8)
15	68185.8(5)	70063.6(5)	1877.8(7)

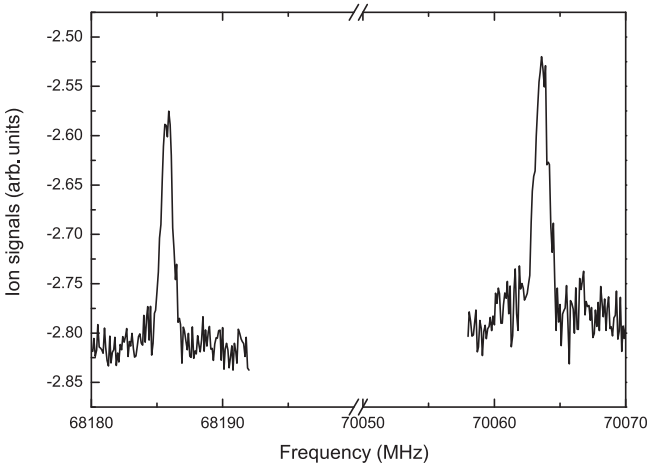

FIG. 6. The single-photon $6s15g \rightarrow 6s15h$ transitions. The two peaks are separated by the K splitting.

B. Two-photon intervals

The procedure used for the two-photon transitions from $6sng$ to $6sni$ was similar to that used for the one-photon transitions. Using the known $6s18g$-$6s18i$ transition frequencies we found the ICE wavelength for $6s18i$, which could then be adjusted for lower n using Eq. (3). The two-photon $6sng$-$6sni$ transition occurs via a virtual intermediate state, and there is a small but measurable ac Stark shift due to the microwave field. To obtain the unshifted intervals, we took measurements at multiple microwave powers and extrapolated our results to zero microwave power. With the available microwave power the maximum ac Stark shift was 1.65 MHz. The uncertainties are those given by the statistical fits to the power extrapolations. Typical two-photon resonances, for $n = 15$, are shown in Fig. 7. The two-photon transition frequencies for $6sng$ to $6sni$, $15 \leqslant n \leqslant 18$ are shown in Table II.

C. Three-photon intervals

We located the $6snk \rightarrow 6p_{1/2}nk$ ICE transitions in essentially the same manner used to find the $6snh \rightarrow 6p_{1/2}nh$ and $6sni \rightarrow 6p_{1/2}ni$ ICE transitions. We do not have enough microwave power to drive the three-photon $6sng$-$6snk$ transitions using a single microwave field. Instead, we use two frequencies. One is close to the two-photon $6sng$-$6sni$ microwave frequency, and the other is close to the $6sni$-$6snk$ frequency, which, for clarity, we term a radio frequency (rf), even though it can be as high as 8.3 GHz. In all cases, the rf frequency was fixed and the microwave frequency swept. We verified that if we changed the rf frequency the $6sng$-$6snk$ intervals were given by twice the microwave frequency plus the rf frequency, indicating that the resonance was due to two microwave photons and one rf photon.

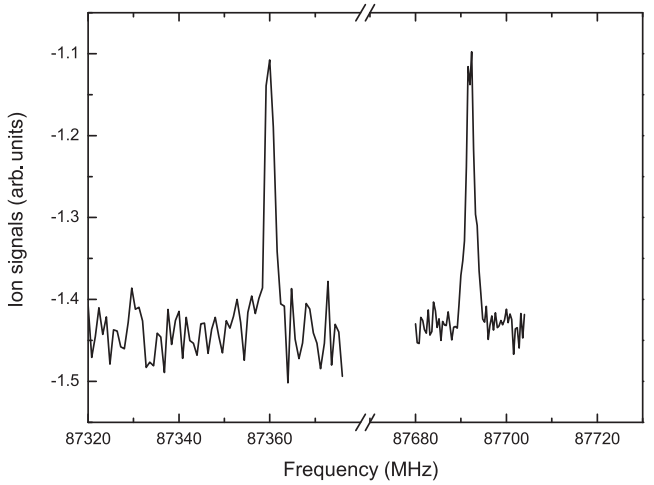

FIG. 7. The two-photon transitions $6s15g \rightarrow 6s15i$. The two resonances are separated by the K splitting of the $6s15i$ state.

TABLE II. ng-ni observed intervals and K splittings.

n	$K = 11/2$ (MHz)	$K = 13/2$ (MHz)	K splitting (MHz)
18	51422.9(3)	51654.6(3)	231.7(4)
17	60667.8(6)	60926.7(8)	258.9(10)
16	72375.6(3)	72669.2(3)	293.6(4)
15	87359.8(4)	87691.3(3)	331.5(5)

There are now two ac Stark shifts, due to the microwave and rf fields. We performed microwave frequency sweeps at different microwave powers and constant rf power, allowing us to extrapolate the observed resonance frequencies to zero microwave power for a given rf power. We repeated this procedure for several different rf powers to extrapolate to zero microwave and rf power. Our fit for the $6s17g \rightarrow 6s17k$, $K = 15/2$, transition is shown in Fig. 8. As expected, the rf power shift is more important since the rf field is nearly resonant with a one-photon transition. In Table III we give the measured intervals after extrapolation, as well as the approximate microwave and rf frequencies used. The uncertainties in our reported intervals correspond to the uncertainties of the power extrapolations.

V. CORE POLARIZATION ANALYSIS OF THE DATA

The adiabatic core polarization model of Mayer and Mayer provides an instructive starting point for the analysis. In it, the energy by which a Ba $6sn\ell$ Rydberg state lies below the hydrogenic energy of $-1/2n^2$ is given by [5]

$$W_{\mathrm{pol},n\ell} = -\tfrac{1}{2}\alpha_d \langle r^{-4}\rangle_{n\ell} - \tfrac{1}{2}\alpha_q \langle r^{-6}\rangle_{n\ell}, \tag{5}$$

where α_d and α_q are the dipole and quadrupole polarizabilities of the Ba^+ ionic core, and $\langle r^{-4}\rangle_{n\ell}$ and $\langle r^{-6}\rangle_{n\ell}$ are the expectation values of the squares of the $n\ell$ Rydberg electron's field and field gradient at the core. The model is termed adiabatic because it is based on the assumption that the Rydberg electron is slowly moving compared to the electrons in the core, providing an essentially static field.

For comparison to experimental data, it is convenient to use Edlen's form of Eq. (5) [7]:

$$W_{\mathrm{pol},n\ell} = -\alpha_d P_{n\ell} - \alpha_q P_{n\ell} Q_{n\ell}, \tag{6}$$

where

$$P_{n\ell} = R\langle r^{-4}\rangle_{n\ell}, \tag{7}$$

$$Q_{n\ell} = \frac{\langle r^{-6}\rangle_{n\ell}}{\langle r^{-4}\rangle_{n\ell}}, \tag{8}$$

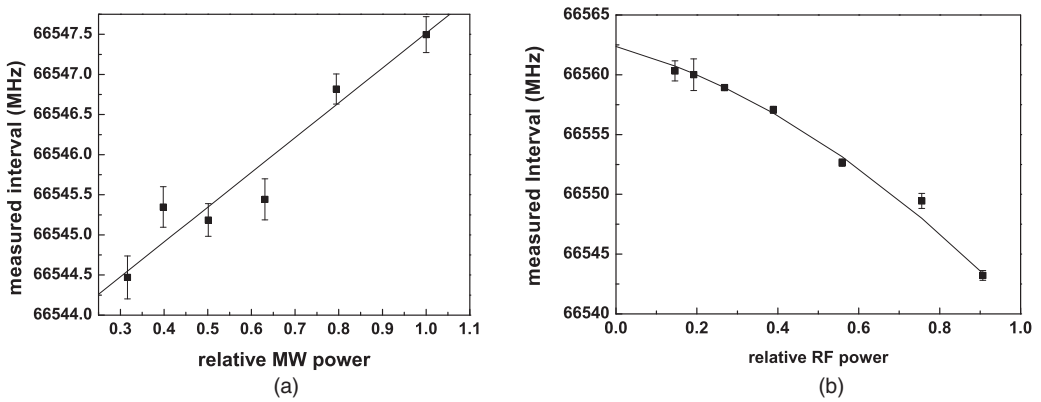

FIG. 8. The extrapolation of the three-photon $6s17g \rightarrow 6s17k$, $K = 15/2$, transition to zero power. (a) Resonances were recorded for multiple microwave powers at each rf power to determine the zero-microwave-power resonance frequency for each rf power. (b) These zero-microwave-power frequencies were then extrapolated to find the zero-power interval, assuming a linear plus quadratic rf power shift, as shown.

and R is the Rydberg constant for Ba; $R = 109\,736.88\ \mathrm{cm}^{-1}$. Experimentally, we observe the $\Delta\ell$ energy intervals $\Delta W_{\mathrm{pol},n\ell'\ell} = W_{\mathrm{pol},n\ell'} - W_{\mathrm{pol},n\ell}$ between Ba $6sn\ell$ and $6sn\ell'$ states of the same n, and we can express the observed intervals in terms of Eq. (6) using

$$\frac{\Delta W_{\mathrm{pol},n\ell'\ell}}{\Delta P_{n\ell\ell'}} = \alpha_d + \alpha_q \frac{\Delta PQ_{n\ell\ell'}}{\Delta P_{n\ell\ell'}}. \tag{9}$$

Here $\Delta P_{n\ell\ell'} = P_{n\ell} - P_{n\ell'}$, and $\Delta PQ_{n\ell\ell'} = P_{n\ell}Q_{n\ell} - P_{n\ell'}Q_{n\ell'}$. The $\Delta\ell$ intervals are largely determined by the dipole polarizability, and in Eq. (9) we have removed the variation due to the dipole polarizability by dividing by $\Delta P_{n\ell\ell'}$. Plotting the left-hand side of Eq. (9) vs $\Delta PQ_{n\ell\ell'}/\Delta P_{n\ell\ell'}$ yields a graph with intercept α_d and slope α_q. In Fig. 9, we have plotted Eq. (9) for the Ba $6sn\ell$ $\ell \rightarrow \ell + 1$ intervals of $\ell \geqslant 5$. The experimental intervals are taken from Gallagher *et al.* [10], Snow and Lundeen [12], and this work. The $\ell \rightarrow \ell + 1$ intervals of $\ell > 6$, $n = 17$ and 20, the high-ℓ intervals, at $\Delta PQ_{n\ell\ell'}/\Delta P_{n\ell\ell'} < 0.002$ fall on a line, as expected, but the $\ell = 6 \rightarrow \ell = 7$, *ni-nk*, intervals at $\Delta PQ_{n\ell\ell'}/\Delta P_{n\ell\ell'} \approx 0.0025$ lie distinctly above the line, and the $\ell = 5 \rightarrow \ell = 6$, *nh-ni*, intervals, at $\Delta PQ_{n\ell\ell'}/\Delta P_{n\ell\ell'} \approx 0.0053$, lie well below the line. The latter two sets of data are displaced from the line due to the breakdown of the adiabatic assumption implicit in Eq. (5).

Almost immediately after the appearance of the paper by Mayer and Mayer, van Vleck and Whitelaw [6] pointed out that Eq. (5) is valid only in the limiting case in which the excited states of the ionic core are far above its ground state. Furthermore, the polarization shifts are are not first-order shifts, as implied by Eq. (5), but second-order shifts. To understand their approach, it is useful to think of the Ba atom as consisting of an inert, but polarizable, Ba^{++} core and two valence electrons. In this case the dipole and quadrupole polarization shifts of the $6sn\ell$ state are due to the dipole and quadrupole couplings of the $6sn\ell$ state to the doubly excited $NLn\ell'$ states. Here NL is the state of Ba^{+}, and $n\ell'$ is the state of the Rydberg electron. The energy shifts are readily calculated in second-order perturbation theory by summing the contributions of all the coupled $NLn\ell'$ states, including continua. For example, the quadrupole polarization energy of the Ba $6s20i$ state comes from the quadrupole couplings to doubly excited Ba $Ndn\ell'$ states with $\ell' = 4$, 6, and 8, as shown schematically in Fig. 10. Summing over all the coupled $Ndn\ell'$ states yields the quadrupole polarization shift. As shown in Fig. 10 for the specific case of $N = 6$, Δ is the energy range spanned by the $n\ell'$ states associated with an Nd ion state, and Ω is the energy difference between the Ba^{+} $6s$ and Nd states. If $\Delta \ll \Omega$ for all N, the sum reduces to $\alpha_q \langle r^{-6} \rangle_{20i}/2$, as in Eq. (5). Thus, a more precise statement of the adiabatic requirement is $\Delta \ll \Omega$ for all NL. For the Ba $Ndn\ell'$ states of

TABLE III. *ng-nk* frequencies and intervals.

n	K	Approximate rf frequency (MHz)	Approximate microwave frequency (MHz)	Extrapolated interval (MHz)
18	13/2	4920	25750	56388.0(20)
	15/2	4640	25895	56424.5(30)
17	13/2	5750	30390	66521.1(12)
	15/2	5750	30400	66562.4(17)
16	13/2	7050	36125	79351.4(17)
	15/2	7050	36150	79393.0(20)
15	13/2	8300	43720	95739.1(20)
	15/2	8100	43875	95798.9(20)

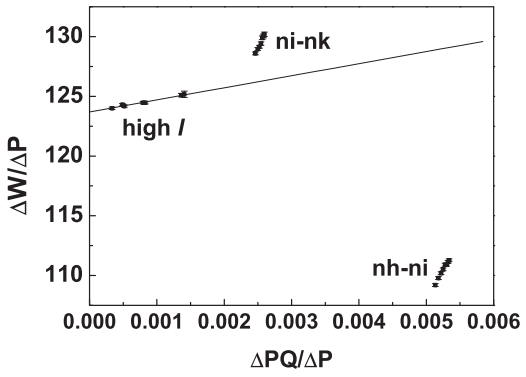

FIG. 9. The adiabatic plot of the measured $\Delta\ell$ intervals using Eq. (9).

$N > 5$ the adiabatic requirement is reasonably well satisfied, but for $N = 5$ it is not.

The most important quadrupole couplings by far are those between the $6s n\ell$ and $5dn'\ell'$ states. As an example we consider the $6s20i$ state, which is coupled to the $5dng$, $5dni$, and $5dn\ell$ states. These states are not energetically removed from the $6s20i$ state by the Ba^+ $6s$-$5d$ interval of $\sim$5000 cm^{-1}, as assumed in the adiabatic model, but by a range of energies comparable to the ion interval. In this case $\Delta \cong \Omega$, and the adiabatic model fails, as shown graphically in Fig. 9. Nonetheless, using hydrogenic wave functions it is straightforward to calculate the energy shift due to the quadrupole coupling to the $5dn\ell'$ states and compare it to that expected from the adiabatic model, yielding the ratio, or correction factor, k_q. Thus we can write the quadrupole polarization shift of the $6s20i$ states due to the $5dn\ell'$ states as $k_q\alpha'_q\langle r^{-6}\rangle_{20i}/2$, where α'_q is the part of the quadrupole polarizability due to the Ba^+ $5d$ state. An analogous procedure can be carried out for the dipole polarization shift, leading to the correction factor k_d. An important point to keep in mind is that k_d and k_q correct for the nonadiabatic effects in the dipole and quadrupole polarization energy shifts, respectively. They are not corrections to the polarizabilities. Thus, for example,

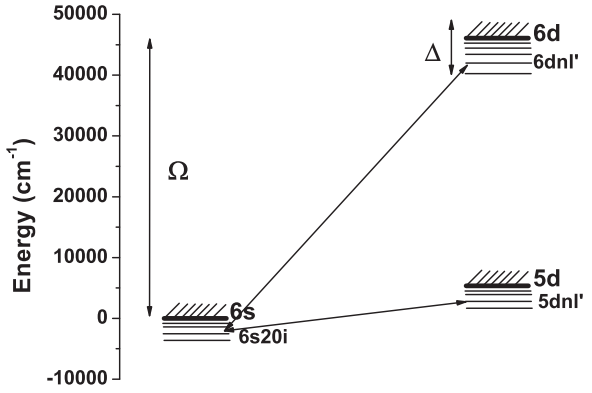

FIG. 10. Energy level diagram showing the quadrupole coupling of the $6s20i$ state to $Ndn\ell'$ states ($\ell' = 4$, 6, and 8). The Ba^+ $6s$ ground-state energy is set to zero. Δ is the energy spread of the $n\ell'$ states, and Ω is the $6s$-Nd ion energy spacing, shown here for $N = 6$. The adiabatic requirement $\Delta \ll \Omega$ is clearly not satisfied for $N = 5$.

the nonadiabatic effect in the dipole polarization energy affects both α_d and α_q.

With the realization that the polarization energy shifts are simply derived from second-order perturbation theory we can understand why the *ni-nk* and *nh-ni* intervals are displaced as they are in Fig. 9. A $6sni$ state has a very strong quadrupole interaction with the low-lying $5d5g$ state which is only $\sim$1000 cm^{-1} above the $6sni$ state. For this reason, the quadrupole polarization energy shift is greater than expected from the adiabatic model, and the *ni-nk* points lie above the line in Fig. 9. The *nh-ni* intervals lie below the line in Fig. 9 because the $6snh$ states have a strong quadrupole interaction with the $5d4f$ state which lies $\sim$1000 cm^{-1} below the $6s20h$ state. The quadrupole interaction shifts the $6s20h$ state up in energy, changing the sign of the quadrupole polarization shift.

The high-ℓ points in Fig. 9 at $\Delta PQ_{n\ell\ell'}/\Delta P_{n\ell\ell'} < 0.001$ fit a straight line fairly well, and we can extract values for α_d and α_q from the intercept and slope of the line through these points, which we term the apparent polarizabilities. The values we obtain are $\alpha_d^{\rm app} = 123.67(6)a_0^3$ and $\alpha_q^{\rm app} = 1047(63)a_0^5$. These values are too small, due to neglect of the nonadiabatic corrections, and for this reason we term the extracted values the apparent polarizabilities.

To extract the correct values of α_d and α_q for Ba^+ from the $\Delta\ell$ intervals of the Ba $6sn\ell$ states, we must account for the nonadiabatic effects, which are prominent in Fig. 9. There are several approaches, and we first describe our approach. We start by noting that the contributions to the Ba^+ $6s$ polarizabilities from Ba^+ states above the $6p$ and $5d$ states are essentially adiabatic, as are those from Ba^{2+}. We assume the nonadiabatic effects to arise only from the $6p$ and $5d$ states of Ba^+, as done by Snow and Lundeen [13]. Accordingly, we write the analog to Eq. (5) as

$$W_{{\rm pol},n\ell} = -\tfrac{1}{2}(\alpha'_d k_d + \alpha''_d)\langle r^{-4}\rangle_{n\ell} - \tfrac{1}{2}(\alpha'_q k_q + \alpha''_q)\langle r^{-6}\rangle_{n\ell}, \tag{10}$$

where α'_d is the part of the dipole polarizability due to the $6p$ state of the Ba^+ ion, α'_q is the part of the quadrupole polarizability due to the $5d$ state of the Ba^+ ion, α''_d is the part of the dipole polarizability due to the higher-p states of the Ba^+ ion and the dipole polarizability of Ba^{2+}, and α''_q is the part of the quadrupole polarizability due to the higher-d states of the Ba^+ ion and the quadrupole polarizability of Ba^{2+}. The nonadiabatic effects are taken into account by introducing the correction factors k_d and k_q [10,13]. In principle, the k_d and k_q factors completely eliminate the nonadiabatic effects. It is straightforward to calculate k_d and k_q if we assume the outer electron to be hydrogenic. Our calculated values of k_d are given in Table IV, and to three significant digits there is no n dependence. The n-dependent k_q values are presented in Table V.

If we define the quantities $P'_{n\ell}$ and $Q'_{n\ell}$ as follows:

$$P'_{n\ell} = k_d P_{n\ell} \tag{11}$$

and

$$Q'_{n\ell} = \frac{k_q}{k_d} Q_{n\ell}, \tag{12}$$

TABLE IV. k_d calculated values.

n	$\ell = 5$	$\ell = 6$	$\ell = 7$	$\ell = 8$	$\ell = 9$	$\ell = 10$	$\ell = 11$
15	0.955278	0.969324	0.979127				
16	0.955326	0.969248	0.978992				
17	0.955494	0.969194	0.978904	0.984568	0.987537	0.989361	
18	0.955404	0.969168	0.978870				
19	0.955470	0.969141	0.978841				
20	0.955510	0.969136	0.978841	0.981743	0.984323	0.985240	0.987553
21	0.955543	0.969128	0.978847				
22	0.955584	0.969126					
23	0.955619						

the energy difference between the ℓ states of the same n can be written as

$$\Delta W_{\mathrm{pol},n\ell'\ell} = \alpha_d' \Delta P'_{n\ell\ell'} + \alpha_d'' \Delta P_{n\ell\ell'} + \alpha_q' \Delta P' Q'_{n\ell\ell'} + \alpha_q'' \Delta P Q_{n\ell\ell'}, \quad (13)$$

where $\Delta W_{\mathrm{pol},n\ell'\ell}$, $\Delta P_{n\ell\ell'}$, and $\Delta P Q_{n\ell\ell'}$ are as defined earlier, $\Delta P'_{n\ell\ell'} = P'_{n\ell} - P'_{n\ell'}$ and $\Delta P' Q'_{n\ell\ell'} = P'_{n\ell} Q'_{n\ell} - P'_{n\ell'} Q'_{n\ell'}$. If we group the α_d'' and α_q'' terms with the observed energy intervals and divide Eq. (13) by $\Delta P'_{\ell\ell'}$, we obtain the following expression:

$$\frac{\Delta W_{\mathrm{pol},n\ell'\ell} - \alpha_d'' \Delta P_{n\ell\ell'} - \alpha_q'' \Delta P Q_{n\ell\ell'}}{\Delta P'_{n\ell\ell'}} = \alpha_d' + \alpha_q' \frac{\Delta P' Q'_{n\ell\ell'}}{\Delta P'_{n\ell\ell'}}, \quad (14)$$

which is the nonadiabatic analog of Eq. (9).

If we know α_d'' and α_q'', we can extract α_d' and α_q' from their linear relationship with the measured $\Delta\ell$ intervals, using the center of gravity of each $6sn\ell$ state. From Ref. [20], $\alpha_d'' = 10.15(53) a_0^3$ and $\alpha_q'' = 814(11) a_0^5$. Figure 11(a) shows the fit of the experimental data to Eq. (14) using our calculated $\Delta P_{n,\ell\ell'}$, $\Delta P Q_{n,\ell\ell'}$, $\Delta P'_{n,\ell\ell'}$, and $\Delta P' Q'_{n,\ell\ell'}$. In Fig. 11 and in all similar plots, for the *nh-ni* and *ni-nk* intervals n increases from 15 to 21 as $\Delta P' Q' / \Delta P'$ increases. Unlike in Fig. 9, the experimental data can be fitted reasonably well by a straight line, and from Fig. 11(a), we obtain $\alpha_d' = 114.47(7) a_0^3$ and $\alpha_q' = 1725(14) a_0^5$. While Fig. 11(a) is an enormous improvement over Fig. 9, the data clearly do not fit the model, as shown by the residuals in Fig. 11(b).

Due to the obvious systematic variations of the residuals, shown in Fig. 11(b), the uncertainties of the values of α_d' and α_q' are larger than the uncertainties from the fit. To understand these uncertainties we have fitted the data in other ways. The first is to remove the lower-ℓ intervals, which have larger nonadiabatic corrections, from the fit. In Fig. 12(a) we show the fit obtained by removing the *nh-ni* intervals from Fig. 11(a). The resulting values, $\alpha_d' = 114.66(12) a_0^3$ and $\alpha_q' = 1664(36) a_0^5$, are not very different from those extracted from Fig. 11(a). The residuals are shown in Fig. 12(b). There are several points to note about Fig. 12(b). First, we note that there is a discontinuity between $n = 18$ and $n = 19$ in the *ni-nk* points, which may be due to a perturbation of the energy levels, which we cannot hope to fit. Second, we believe the $n = 20$ $\ell = 7 \rightarrow \ell = 8$ and $\ell = 10 \rightarrow \ell = 11$ points to be in error. We shall return to this point. Finally, if the two $n = 20$ points and the discontinuity at $n = 18$ are ignored, the systematic variation of the residuals is essentially gone. If we remove the *ni-nk* intervals from Fig. 12(a), leaving only the high-ℓ intervals from Snow and Lundeen, we obtain the plot of Fig. 13, which yields $\alpha_d' = 115.08(16) a_0^3$ and $\alpha_q' = 1160(170) a_0^5$. With this restricted set of data the scatter is now clearly more important than any systematic variation. Inspection of the $\ell = 7 \rightarrow \ell = 8$ points of Fig. 13 shows why we believe the $n = 20$ points to be suspect. The two $\ell = 7 \rightarrow \ell = 8$ points by themselves imply an impossible negative quadrupole polarizability, as do the $\ell = 10 \rightarrow \ell = 11$ and either of the $\ell = 9 \rightarrow \ell = 10$ points.

An alternative approach is to fit the $\Delta\ell$ intervals for each n state separately, and in Fig. 14 we show the values of α_d' and α_q' extracted from the data shown in Fig. 11(a). Only for $n = 17$ and 20 are there more than two $\Delta\ell$ intervals, so only in those two cases can we show uncertainties for the fits. We expect that if we had more points the uncertainties of the other n states would be similar. If we disregard the obvious outliers at $n = 18$ and 21, there is no monotonic increase or decrease in the value of α_d', and the average value, $\alpha_d' = 114.51(2) a_0^3$, is similar to the value extracted from Fig. 11(a). The $n = 18$ intervals were measured in two different experiments, so we do not think the $n = 18$ points are displaced from the others due to an experimental problem, but for a physical reason. As already noted, the *ni-nk* residuals of Fig. 12(b) exhibit a discontinuity at $n = 18$, which might be a sign of a series perturbation. The $n = 21$ points in Fig. 14 probably reflect experimental error.

In contrast to the relatively constant values of α_d' shown in Fig. 14, the extracted values of α_q' show a clear n dependence, and we suspect that its origin lies in our calculation of k_q,

TABLE V. k_q calculated values.

n	$\ell = 5$	$\ell = 6$	$\ell = 7$
15	−0.982	1.439	1.032
16	−0.889	1.473	1.039
17	−0.818	1.503	1.044
18	−0.761	1.531	1.050
19	−0.715	1.555	1.054
20	−0.678	1.577	1.058
21	−0.647	1.596	1.061
22	−0.620	1.614	
23	−0.598		

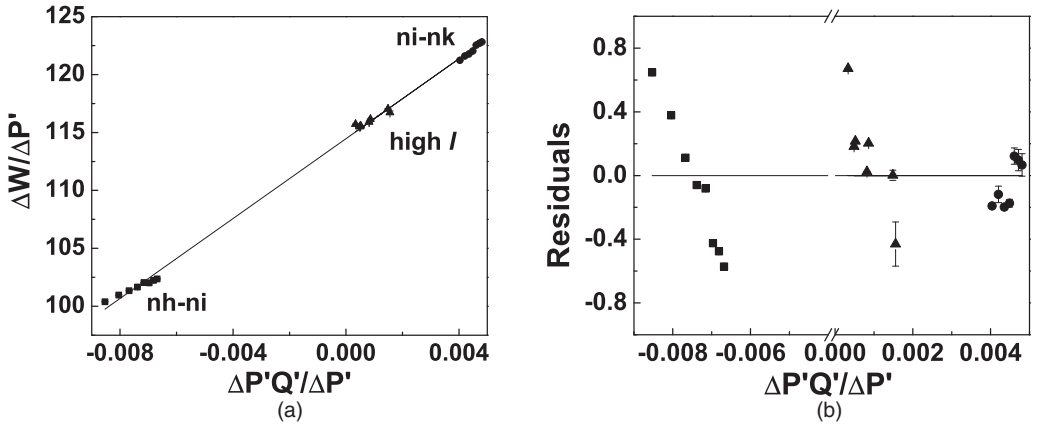

FIG. 11. (a) Graph of $(\Delta W_{\mathrm{pol},n\ell'\ell} - \alpha_d''\Delta P_{n\ell\ell'} - \alpha_q''\Delta P Q_{n\ell\ell'})/\Delta P'_{n\ell\ell'}$ vs $\Delta P' Q'_{n\ell\ell'}/\Delta P'_{n\ell\ell'}$. The symbols ■, ●, and ▲ are the data points presenting the *nh-ni*, *ni-nk*, and high-ℓ intervals, respectively. For the *nh-ni* and *ni-nk* intervals n increases monotonically from 15 to 21 as $\Delta P' Q'/\Delta P'$ increases. The high-ℓ intervals are for $n = 17$ and 20. The linear fit yields the y intercept and the slope, which are the values of α_d' and α_q', respectively. From the graph, we obtain $\alpha_d' = 114.47(7)a_0^3$ and $\alpha_q' = 1725(14)a_0^5$, and in (b) the plot displays the residuals relative to the fit, which is the zero line.

especially for $\ell = 5$. There are several sources of error in calculations of k_d and k_q. We have ignored the spin-orbit splittings of the Ba^+ $6p$ and $5d$ states, and we have assumed the outer electron to be hydrogenic. The latter assumption leads to incorrect energies, and, more important, incorrect wave functions. For this problem, matrix elements of inverse powers of r are required, which in turn requires wave functions accurate at small r. Unfortunately, there is no simple method to generate nonhydrogenic wave functions which are accurate at small r.

Irrespective of the source of the variation in α_q' seen in Fig. 14, it is clear that we cannot extract a value of α_q' from these data, and the value of α_d' is also suspect. Accordingly, we have fitted the *ni-nk* and higher-ℓ intervals of Fig. 12(a) for $n = 17$ and 20, the only n values for which we have more than one $\Delta\ell$ interval. For $n = 17$ we obtain $\alpha_d' = 114.62(5)a_0^3$ and $\alpha_q' = 1640(23)a_0^5$, and for $n = 20$ $\alpha_d' = 114.73(27)a_0^3$ and $\alpha_q' = 1650(120)a_0^5$. The $n = 17$ data lie almost perfectly on a straight line, while the $n = 20$ data are more scattered. The important point is that α_q' exhibits no n dependence. Thus we conclude that the fit of Fig. 12(a) provides the best values for α_d' and α_q'. The high-ℓ data shown in Fig. 13 exhibit no systematic problem, but the high-ℓ intervals are more susceptible to Stark shifts and are not as sensitive to the quadrupole polarizability as are the lower-ℓ intervals.

To account for possible systematic effects in the determination of α_d' and α_q' we increase their uncertainties from the fit shown in Fig. 12(a) to encompass the residuals shown in Fig. 12(b) except the two $n = 20$ points mentioned previously. The results are $\alpha_d' = 114.66(25)a_0^3$ and $\alpha_q' = 1664(50)$. Adding them to α_d'' and α_q'' we obtain the ionic Ba^+ dipole and quadrupole polarizabilities $\alpha_d = 124.81(25)a_0^3$ and $\alpha_q = 2478(50)a_0^5$, respectively.

It is useful to compare our values to those obtained from other measurements and theory. In Table VI we present the values obtained for α_d, and in Table VII, we present the values for α_q' and α_q. Our value for α_d agrees with the theoretical value to within the theoretical uncertainty, but our value for α_q is half the theoretical value. It is perhaps more interesting to compare the experimental results. Two methods have been

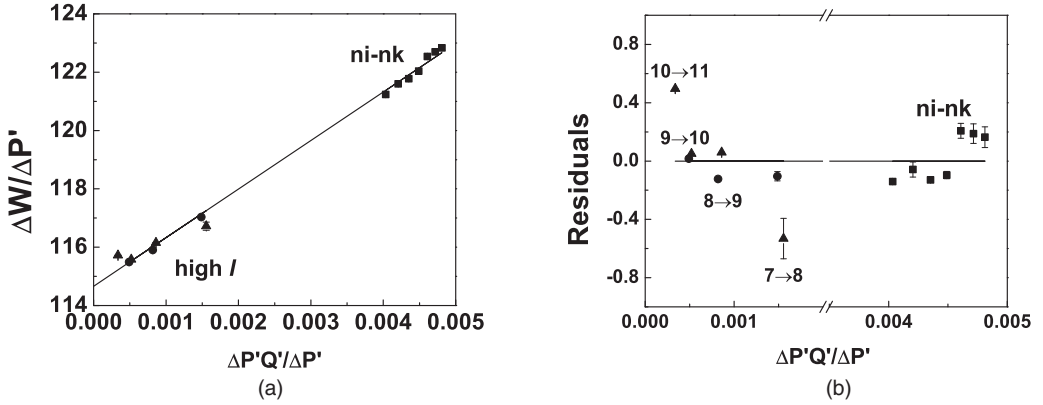

FIG. 12. (a) Plot obtained by removing the *nh-ni* intervals from the data in Fig. 11(a). For the *ni-nk* intervals n increases monotonically from 15 to 21 as $\Delta P' Q'/\Delta P'$ increases. The high-ℓ points are for $n = 17$ (●) and $n = 20$ (▲). From the graph, we obtain $\alpha_d' = 114.66(12)a_0^3$ and $\alpha_q' = 1664(36)a_0^5$. (b) The residuals of (a). There is far less systematic variation of the residuals than in Fig. 11(b).

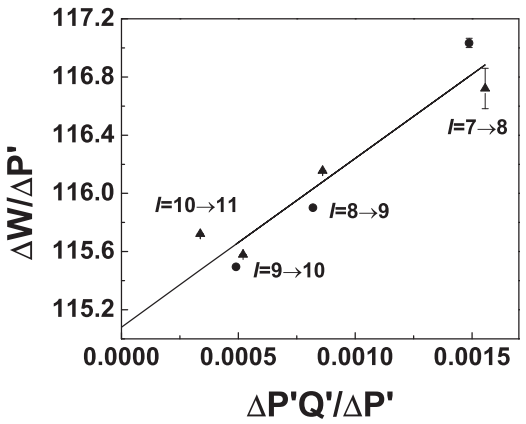

FIG. 13. Plot of high-ℓ intervals from Fig. 11(a) for $n = 17$ (•) and $n = 20$ (▲). From the graph, we obtain $\alpha_d' = 115.08(16)a_0^3$ and $\alpha_q' = 1160(170)a_0^5$.

used to extract the polarizabilities, polarization analysis of the $\Delta\ell$ intervals and analysis of the K splittings. Analysis of the K splittings yields the Ba^+ $6s$-$6p$ and $6s$-$5d$ radial matrix elements, from which α_d' and α_q' are easily computed. To the values of α_d' and α_q' given in Ref. [16] we have added the theoretical values $\alpha_d'' = 10.15a_0^3$ and $\alpha_q'' = 814a_0^5$ yielding the values of α_d and α_q given in Tables VI and VII. While it is possible to make good measurements of the K splittings, they arise completely from the nonadiabatic effects, and their analysis is much more complicated than a polarization analysis of $\Delta\ell$ intervals. For this reason, we choose to compare our results to those of Snow and Lundeen, Ref. [21].

Using essentially the same data as we have used here, Snow and Lundeen [21] arrived at a value of α_d distinctly smaller than ours and a value of α_q almost twice ours. To understand the origin of the differences it is useful to use four different methods to analyze the data. Specifically, we consider ignoring the nonadiabatic effects, using the adiabatic expansion method, introducing k_q and using the adiabatic expansion method to

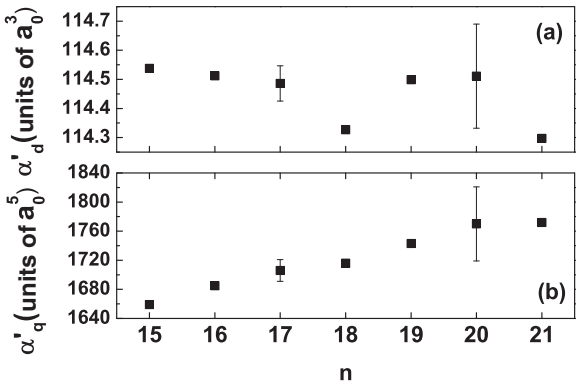

FIG. 14. Graph showing the values of (a) α_d' and (b) α_q' extracted from $\Delta\ell$ intervals for each n. Disregarding the obvious outliers at $n = 18$ and 21, there is no monotonic increase or decrease in the value of α_d', and the average value is $\alpha_d' = 114.51(2)a_0^3$. A value of α_q' cannot be extracted from (b). Only $n = 17$ and 20 have more than two data points (the nh-ni, ni-nk, and high-ℓ intervals), and therefore only their uncertainties can be shown.

TABLE VI. The Ba^+ $6s$ dipole polarizability (α_d) obtained from this work, and other theoretical and experimental results.

	α_d (units of a_0^3)
Core polarization	
This work	124.81(25)
Expt. [10]	125.5(10)
Expt. [13]	124.30(16)
Expt. [21]	123.88(5)
K splitting	
Expt. [16]	121.3(66)
Expt. [22]	123.88(5)
Theory [20]	124.15

account for nonadiabatic effects in the dipole polarization energy, and finally introducing both k_q and k_d. For simplicity, we label these methods I, II, III, and IV, respectively. Method III is similar to that used by Snow and Lundeen, and IV is similar to ours.

If we restrict our attention to only the high-ℓ intervals, it is not unreasonable to think that the data can be fitted by ignoring the nonadiabatic effects, method I, and using Eq. (9). The straight line through the high-ℓ points of Fig. 9 is precisely this fit. It yields $\alpha_d = \alpha_d^{\rm app} = 123.67a_0^3$ and $\alpha_q = \alpha_q^{\rm app} = 1047a_0^5$.

In the adiabatic expansion method, method II, the polarization energy of Eq. (5) is replaced by

$$W_{{\rm pol},n\ell} = -\tfrac{1}{2}\alpha_d\langle r^{-4}\rangle_{n\ell} - \tfrac{1}{2}(\alpha_q - 6\beta_1)\langle r^{-6}\rangle_{n\ell}\cdots, \quad (15)$$

where the ellipsis indicates terms containing expectation values of higher inverse powers of r. The most important difference, from our present point of view, is the presence of $6\beta_1$ in the $\langle r^{-6}\rangle$ term, which is due to the nonadiabatic effect in the dipole polarization energy. It appears in the same way as the quadrupole polarizability, and for Ba $\beta_1 = 605(25)a_0^5$ [21]. The higher inverse powers of r represent higher-order terms due to the nonadiabatic effect in the dipole polarization energy, the nonadiabatic effect in the quadrupole polarization energy, and higher multipole terms. As Snow and Lundeen have shown, these terms can be represented by higher-order terms in $\langle r^{-6}\rangle/\langle r^{-4}\rangle$, or equivalently, in $\Delta PQ/\Delta P$, so that the data points of Fig. 9 no longer need to be fitted by a straight line. Application of the adiabatic expansion method is based on the assumption that the expansion is convergent. Inspection of Fig. 9 suggests that very high-order terms in $\Delta PQ/\Delta P$ will be

TABLE VII. The Ba^+ $6s$ quadrupole polarizability (α_q) and the contribution of the Ba^+ $5d$ state (α_q') to it.

	α_q' (units of a_0^5)	α_q (units of a_0^5)
Core polarization		
This work	1664(50)	2478(50)
Expt. [10]		2050(100)
Expt. [21]	1524(8)	4420(250)
Expt. [13]	1828(88)	2462(361)
K splitting		
Expt. [16]	1562(93)	2376(93)
Expt. [22]	3606(250)	4420(250)
Theory [20]	3368(34)	4182(34)

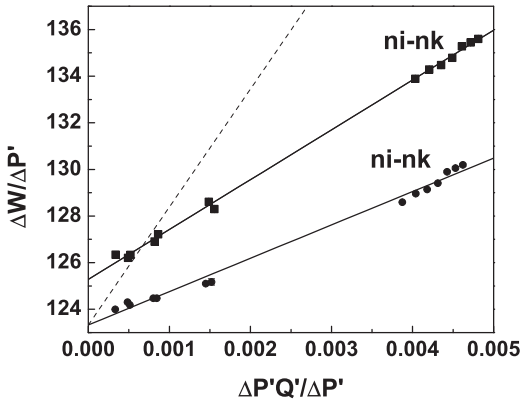

FIG. 15. Comparison between the use of method III to treat the ni-nk and the high-ℓ intervals (•) and method IV to treat the intervals (■). Here we assume that α_d'' and α_q'' both vanish. The introduction of k_q in method III removes the nonadiabatic effect in the quadrupole polarization energy, and all the data points fall on a line, unlike the plot of Fig. 9. The intercept of the fit line gives $\alpha_d = 123.33(11)a_0^3$. Adding $6\beta_1$ from the nonadiabatic correction to the dipole polarization energy to the slope of the fit line give the broken line, which has slope $\alpha_q = 5060a_0^5$. The introduction of k_d as well as k_q in method IV both raises the points and increases the slope of the fit line; the resulting intercept and slope are $\alpha_d = 125.28(8)a_0^3$ and $\alpha_q = 2138(24)a_0^5$.

required to fit the data, indicating that the adiabatic expansion is almost certainly not convergent in this case. However, it should be applicable if we again restrict our attention to the high-ℓ states. Fitting the high-ℓ data of Fig. 9 to the first two terms of Eq. (15) leads to $\alpha_d = \alpha_d^{\rm app} = 123.67a_0^3$ and $\alpha_q = \alpha_q^{\rm app} + 6\beta_1 = 4677a_0^5$.

The deviation of the factors k_d and k_q from unity is an indication of the severity of the nonadiabatic effects. Inspection of Tables IV and V shows that $0.955 < k_d < 0.990$ while k_q ranges from -0.0982 to 1.614, suggesting that the nonadiabatic effect in the quadrupole polarization energy is by far the worse problem. Accordingly, we treat the data using method III, treating the nonadiabatic effects in the quadrupole and dipole polarization energies by k_q and an adiabatic expansion, respectively. This approach is approximately that used by Snow and Lundeen. It differs in that Snow and Lundeen, and we as well, separated the polarizabilities into two parts, for example, $\alpha_q = \alpha_q' + \alpha_q''$. To display most clearly the effect of introducing first k_q and then k_d we here assume that α_d'' and α_q'' both vanish, so that $\alpha_d' = \alpha_d$ and $\alpha_q' = \alpha_q$. Since $\alpha_d' = 0.92\alpha_d$, this approximation is excellent for α_d, and it is not unreasonable for α_q. In Fig. 15 using solid circles (•) we use method III to plot the high-ℓ and ni-nk intervals using the values of k_q given in Table V. Since we are now introducing k_q, and later shall introduce k_d, as the horizontal and vertical axes, we use $\Delta P' Q'_{n\ell'\ell}/\Delta P'_{n\ell\ell}$ and $\Delta W_{{\rm pol},n\ell'\ell}/\Delta P'_{n\ell\ell'}$. From the definitions of P' and Q' it is evident that P and Q are simply the special cases of P' and Q' for $k_d = k_q = 1$. The dominant effect of the introduction of k_q is to move points horizontally on the plot, which removes the glaring problem due to the nonadiabatic effects, the seemingly random distribution of points in Fig. 9. Now in Fig. 15 the solid circles (•) all lie along a straight line. In method III the adiabatic expansion needs to account only for the nonadiabatic effect on the dipole polarization. Accordingly, we fit the solid circles (•) to

$$\frac{\Delta W_{{\rm pol},n\ell'\ell}}{\Delta P'_{n\ell\ell'}} = \alpha_d + (\alpha_q - 6\beta_1)\frac{\Delta P' Q'_{n\ell\ell'}}{\Delta P'_{n\ell\ell'}}. \qquad (16)$$

The intercept of the fit line is $\alpha_d = 123.33(11)a_0^3$, and the slope $s_q = 1430(35)a_0^5$. The quadrupole polarizability $\alpha_q = s_q + 6\beta_1 = 5060a_0^5$ is the slope of the broken line in Fig. 15.

To show the effect of using k_d as well as k_q, method IV, in Fig. 15 we also plot, as solid squares (■), the high-ℓ and ni-nk intervals. The introduction of k_d has two effects, both of which are evident in Fig. 15. First, it raises all the points by 1%–3%, since $k_d < 1$ and $\Delta P' < \Delta P$. The effect is to raise the value of α_d; $\alpha_d = 125.28(8)a_0^3$. Second, since k_d falls further below 1 as ℓ is decreased, the slope of the line through the points is increased. In this method the slope (of the line through the square points) is $\alpha_q = 2138(23)a_0^5$. The nonadiabatic effect in the dipole polarization energy on α_q is the difference between the slopes of the lines through the squares and circles in Fig. 15, $708a_0^5$, much less than $6\beta_1 = 3630a_0^5$.

In Table VIII we have collected the results from the four analyses and presented them together with the values of Snow and Lundeen and ourselves. Methods I, II, and III yield essentially the same value of α_d, which implies that the adiabatic expansion method, or a modification which does not introduce k_d, has almost no effect on the value of α_d extracted. These values are also very close to the value obtained by Snow and Lundeen. The introduction of k_d, in method IV, vertically displaces the points in Fig. 15 and increases the value of α_d extracted to very nearly match our value. The quadrupole polarizabilities extracted by methods II and III are both much larger than those obtained by methods I and IV, due to the inclusion of $6\beta_1$ in the extracted value. These values are close to the value obtained by Snow and Lundeen. Method IV yields a value of α_q similar to our value and much smaller than those of methods II and III. From Table VIII it is evident that the difference between the values of both α_d and α_q extracted by Snow and Lundeen and ourselves is due almost entirely to the treatment of the nonadiabatic effect in the dipole polarization.

TABLE VIII. The Ba^+ 6s dipole (α_d) and quadrupole polarizabilities (α_q) extracted from different methods of data analysis.

Analysis method	α_d (units of a_0^3)	α_q (units of a_0^5)
Method I: ignore nonadiabatic	123.67(6)	1047(63)
Method II: adiabatic expansion	123.67(6)	4680(160)
Method III: k_q and adiabatic expansion	123.33(11)	5060(150)
Method IV: k_d and k_q	125.28(8)	2138(23)
Snow and Lundeen [21]	123.88(5)	4420(250)
This work	124.81(25)	2478(50)

VI. CONCLUSION

We have demonstrated that ICE laser excitation to autoionizing states can be used to detect microwave transitions between high-angular-momentum Rydberg states of alkaline-earth-metal atoms, even though the ICE transitions are badly

overlapped. We have used this technique to measure $\Delta\ell$ intervals between Ba $6sn\ell$ states of $15 \leqslant n \leqslant 18$ and $5 \leqslant \ell \leqslant 7$. Combining these measurements with other measurements of Ba $\Delta\ell$ intervals, we have extracted the Ba^+ polarizabilities $\alpha_d = 124.81(25)a_0^3$ and $\alpha_q = 2478(50)a_0^5$. These values disagree with recently reported experimental values due to the difference in the treatment of the nonadiabatic effects. In principle, the model we have used exactly accounts for the nonadiabatic effects by the introduction of the correction factors k_d and k_q, which are calculated numerically. The calculations can be improved by better numerical techniques, the inclusion of spin-orbit coupling, and the use of nonhydrogenic wave functions where required. We hope this work will stimulate theoretical activity along these lines.

ACKNOWLEDGMENTS

This work has been supported by the U.S. Department of Energy, Office of Basic Energy Sciences. J.N. would like to thank the Thailand Research Fund (TRF) and the National Research University Project under the Office of the Higher Education Commission (CHE), Ministry of Education Grant (Grant No. MRG5680117) for its support. We are grateful to S. R. Lundeen for helpful discussions.

[1] M. Chwalla, J. Benhelm, K. Kim, G. Kirchmair, T. Monz, M. Riebe, P. Schindler, A. S. Villar, W. Hänsel, C. F. Roos, R. Blatt, M. Abgrall, G. Santarelli, G. D. Rovera, and Ph. Laurent, Phys. Rev. Lett. **102**, 023002 (2009).
[2] N. Huntemann, M. Okhapkin, B. Lipphardt, S. Weyers, Chr. Tamm, and E. Peik, Phys. Rev. Lett. **108**, 090801 (2012).
[3] B. Arora, M. S. Safronova, and C. W. Clark, Phys. Rev. A **76**, 064501 (2007).
[4] U. I. Safronova and M. S. Safronova, Phys. Rev. A **79**, 022512 (2009).
[5] J. E. Mayer and M. G. Mayer, Phys. Rev. **43**, 605 (1933).
[6] J. H. Van Vleck and N. G. Whitelaw, Phys. Rev. **44**, 551 (1933).
[7] B. Edlen, *Handbuch der Physik* (Springer, Berlin, 1964).
[8] S. R. Lundeen, Adv. At., Mol. Opt. Phys. **52**, 161 (2005).
[9] T. R. Gentile, B. J. Hughey, D. Kleppner, and T. W. Ducas, Phys. Rev. A **42**, 440 (1990).
[10] T. F. Gallagher, R. Kachru, and N. H. Tran, Phys. Rev. A **26**, 2611 (1982).
[11] J. Nunkaew, E. S. Shuman, and T. F. Gallagher, Phys. Rev. A **79**, 054501 (2009).
[12] E. L. Snow and S. R. Lundeen, Phys. Rev. A **77**, 052501 (2008).
[13] E. L. Snow, M. A. Gearba, R. A. Komara, S. R. Lundeen, and W. G. Sturrus, Phys. Rev. A **71**, 022510 (2005).
[14] W. E. Cooke, T. F. Gallagher, S. A. Edelstein, and R. M. Hill, Phys. Rev. Lett. **40**, 178 (1978).
[15] E. L. Snow, R. A. Komara, M. A. Gearba, and S. R. Lundeen, Phys. Rev. A **68**, 022510 (2003).
[16] E. S. Shuman and T. F. Gallagher, Phys. Rev. A **74**, 022502 (2006).
[17] W. E. Cooke and T. F. Gallagher, Opt. Lett. **4**, 173 (1979).
[18] J. Nunkaew and T. F. Gallagher, Phys. Rev. A **81**, 023417 (2010).
[19] R. R. Jones and T. F. Gallagher, Phys. Rev. A **38**, 2846 (1988).
[20] E. Iskrenova-Tchoukova and M. S. Safronova, Phys. Rev. A **78**, 012508 (2008).
[21] E. L. Snow and S. R. Lundeen, Phys. Rev. A **76**, 052505 (2007).
[22] Shannon L. Woods, S. R. Lundeen, and Erica L. Snow, Phys. Rev. A **80**, 042516 (2009).

Microwave spectroscopy of the calcium $4snf \rightarrow 4s(n+1)d$, $4sng$, $4snh$, $4sni$, and $4snk$ transitions

J. Nunkaew[1,*] and T. F. Gallagher[2]

[1]*Department of Physics and Materials Science, Faculty of Science, Chiang Mai University, Chiang Mai 50200, Thailand*

[2]*Department of Physics, University of Virginia, Charlottesville, Virginia 22904, USA*

(Received 27 January 2015; published 10 April 2015)

We observe the microwave transitions of calcium from the $4snf$ states to the $4s(n+1)d$, $4sng$, $4snh$, $4sni$, and $4snk$ states for $18 \leqslant n \leqslant 23$ using delayed field ionization as the state selective detection technique. The observed intervals between the $\ell \geqslant 5$ states can be analyzed to extract the Ca^+ ionic dipole (α_d) and quadrupole (α_q) polarizabilities using two nonadiabatic core polarization models. Using these two models we determine the ionic dipole and quadrupole polarizabilities to be $75.3a_0^3 < \alpha_d < 76.9a_0^3$ and $206a_0^5 < \alpha_q < 1590a_0^5$, respectively.

DOI: 10.1103/PhysRevA.91.042503 PACS number(s): 32.30.−r, 32.10.Dk, 32.80.Rm

I. INTRODUCTION

In recent years, much effort has been invested in developing a precise optical frequency standard, and a proposed candidate is the quadrupole $4s_{1/2} - 3d_{5/2}$ transition of the Ca^+ ion [1,2]. An additional attraction of Ca^+ is that it can be cooled by Doppler cooling to very low temperatures by using this transition in conjunction with the dipole allowed $3d_{5/2} - 3p_{3/2}$ transition [1]. The absolute frequency of the Ca^+ $4s_{1/2} - 3d_{5/2}$ transition has been measured with an uncertainty of 1 Hz, a fractional accuracy of one part in 10^{15}, which is within a factor of 3 of the fractional uncertainty of the present Cs clock [3]. While an optical transition provides a transition with a higher quality factor, the transition also has a much larger blackbody radiation (BBR) shift, and the BBR shift is one of the largest shifts in an optical clock. In the Ca^+ clock transition the BBR shift is calculated to be 0.4 Hz at room temperature, $T = 300$ K [1,2,4]. Since the BBR shift is unavoidable and scales as T^4 [5], it is essential to understand it well.

The BBR shift is proportional to the difference in the dipole polarizabilities α_d of the two ionic states of the clock transition. While it is possible to calculate the polarizabilities, due to the charge of the ion the polarizabilities are difficult to measure directly, and other approaches must be used to check the validity of the calculations. While measurements of oscillator strengths and lifetimes are often used, an alternative approach is one initially suggested by Mayer and Mayer, measuring the energy intervals between higher ℓ Rydberg states of the neutral atom [6]. Here ℓ is the orbital angular momentum of the Rydberg electron. The field and gradient from the Rydberg electron polarize the ionic core, depressing the energy levels below the hydrogenic energy of $-1/2n^2$, where n is the principal quantum number of the Rydberg electron. We use atomic units unless specified otherwise. Since an electron in a lower ℓ state comes closer to the ionic core, the polarization shift increases with decreasing ℓ. This approach is only valid if the Rydberg electron does not penetrate the ionic core, which is why it is limited to high ℓ states. The inner turning point of a Rydberg $n\ell$ atom is given by $r_\ell \cong \ell(\ell+1)/2$, and $r_\ell = 15a_0$ for $\ell = 5$. Since the Ca^+ $4s_{1/2}$ wave function is similar in size to the H $1s$ wave function, less than 0.02% of the ground-state probability distribution is found at radial distances beyond $r = 15a_0$, so it seems that Ca $4sn\ell$ states of $\ell \geqslant 5$ should be nonpenetrating states. Here r is the distance of the Rydberg electron from the ionic core.

Here we report measurements of the Ca $4snf - 4sng - 4snh - 4sni - 4snk$ intervals, made using a delayed field ionization approach. Our data show that the adiabatic model of Mayer and Mayer is inadequate, and we have fit our measurements to two core polarization models which take into account the nonadiabatic effects not considered in the approach of Mayer and Mayer. These analyses yield values for the dipole polarizability in reasonable agreement with the calculated value. However, the two values we extract for the quadrupole polarizability are much smaller and much larger than the calculated value. We have also measured the $4snf \rightarrow 4s(n+1)d$ intervals. These intervals, combined with high-resolution optical spectroscopy could allow a better determination of the Ca^+ polarizabilities. In the sections which follow we describe our approach, present our experimental results, and analyze them using several variants of core polarization analysis.

II. EXPERIMENTAL APPROACH

We excite neutral Ca atoms in a thermal beam from the ground state to a Rydberg state using three laser beams. The Ca beam intersects the laser beams at a 90° angle between two parallel horizontal copper plates separated by 1.2-cm-long ceramic standoffs. The laser beams are focused to 1 mm diameters where they intersect the Ca beam. Ground-state $4s^2$ atoms are excited to the $4s4p$, $4s4d$, and $4snf$ states by 422.791 nm, 732.816 nm, and ∼850 nm laser pulses, respectively, as shown in Fig. 1. The last laser is tunable over the range from 847 to 857 nm to excite the $4snf$ states of $18 \leqslant n \leqslant 23$. A 1-$\mu$s-long microwave pulse starts 50 ns after the last laser pulse to excite the $4snf$ state to the $4sng$ and $4snh$ states by the one-photon and two-photon transitions, respectively. The $4snf \rightarrow 4sni$ and $4snf \rightarrow 4snk$ transitions are the three-photon and four-photon transitions. To drive the three-photon and four-photon excitations, in addition to a 1 μs microwave pulse, we use a continuous wave (cw) radio frequency (rf) field of frequency between 3.5 and 5 GHz. The rf and microwave fields are generated by a Hewlett-Packard (HP) 8257D analog signal generator and 83620A synthesized sweep generator, respectively. The microwave sweep generator produces a cw output from 10 MHz to 20 GHz, which is

*jn8h@virginia.edu

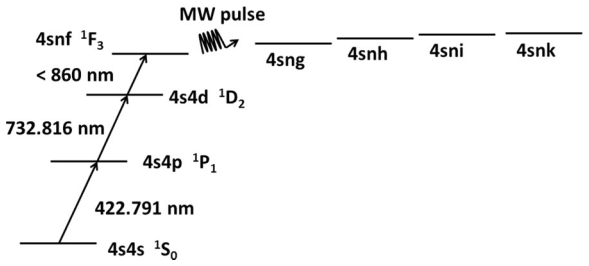

FIG. 1. Laser excitation scheme of the experiment.

formed into pulses by a General Microwave DM862D switch. The required microwave frequencies to drive the transitions range from 23 to 75 GHz. Therefore, several frequency multipliers, a Narda DBS 2640X220 active doubler, a Narda DBS 4060X410 active quadrupler, and a Pacific Millimeter V2W0 passive doubler, are used to multiply the synthesizer frequency to the desired frequency. The power output of the frequency multipliers ranges from 5 mW to 100 mW. The microwaves propagate through WR28 waveguide and a waveguide feedthrough to a WR28 horn inside the vacuum chamber. The cw rf propagates through a coaxial cable and a SMA feedthrough to the coaxial-to-waveguide adapter and is launched by a WR187 horn inside the chamber.

To discriminate between the $4snℓ$ states of $ℓ > 3$ and the $4snf$ state, we take advantage of the $ℓ$ dependence of the lifetimes of Ca Rydberg atoms. The higher angular momentum Rydberg states live longer than the lower ones [7,8], and we use the technique of delayed field ionization (DFI). The lifetime of the $4s25f$ state has been measured to be ∼2.5(5) μs [8], and using the n^3 scaling law we find that the lifetimes of the $4snf$ states of $18 \leqslant n \leqslant 23$ fall in the range from 0.9 to 1.9 μs. Therefore, if we wait long enough after the microwave pulse, more than 5 μs, atoms in the $4snf$ states decay significantly compared to atoms in the $4snℓ$ states of $ℓ > 3$. Typically, we apply a negative high voltage pulse to the bottom plate 8 to 10 μs after the microwave pulse to field ionize the surviving Rydberg atoms and drive the resulting electrons to the microchannel plate (MCP) detector. The timing of the experiment is shown in Fig. 2. Using this approach a large increase in the number of detected atoms is observed when the microwave field drives the transition from the $4snf$ state at resonance. To detect transitions from the $4snf$ states to the $4s(n+1)d$ states we take advantage of the fact that the lifetimes of the $4s(n+1)d$ states are an order of magnitude shorter than those of the $4snf$ states. A delay of only 2 μs

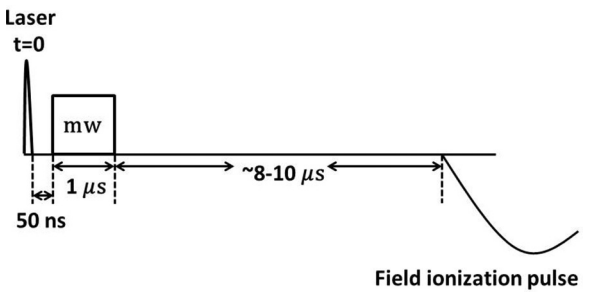

FIG. 2. Timing sequence of the experiment.

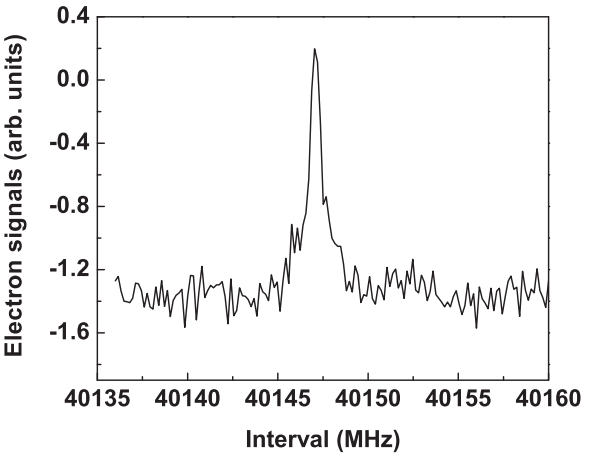

FIG. 3. One-photon $4s22f \rightarrow 4s22g$ resonance. The linewidth of the resonance is ∼1 MHz which is a transform limited linewidth of a 1 μs microwave pulse.

is used, and a decrease in signal is observed at resonance. Frequency shifts due to the stray electric field are minimized by observing the microwave resonance with different bias voltages on the plates and fitting the resonant frequencies to a quadratic bias voltage dependence. We then set the bias voltage to the minimum frequency shift. In this experiment, the frequency shift due to the stray electric field is in all cases less than 1 MHz. The experiment is repeated every 50 ms, and the signals are averaged over many laser shots.

III. EXPERIMENTAL OBSERVATIONS

A. One-photon $4snf \rightarrow 4sng$ intervals

For the one-photon transition, $4snf \rightarrow 4sng$, the microwave power was attenuated until the power broadening was eliminated. We observed one resonant peak for each n. Since the optical excitation is to the $4snf$ $^1F_3$ state we assign the states we observe in the microwave transitions as $^1G_4$ states. A typical resonance is shown in Fig. 3, and the observed intervals are given in Table I. We did not attempt to eliminate the Earth's magnetic field. In the Earth's magnetic field one might expect linewidths of ∼2–3 MHz. However, the typical linewidth of a $^1F_3 - {}^1G_4$ resonance is ∼1 MHz, the transform limited linewidth of a 1 μs microwave pulse. The narrow linewidths occur because the one-photon transitions are between the two singlet states, which have the same Landé g_j factors. Hence all the $\Delta m_j = 0$ transitions occur at the same frequency, resulting in the narrow lines [9].

TABLE I. $nf - ng$ observed frequencies.

n	Observed frequency (MHz)
18	72891.40(1)
19	62222.19(1)
20	53150.84(2)
21	46053.01(25)
22	40147.03(1)
23	35462.65(5)

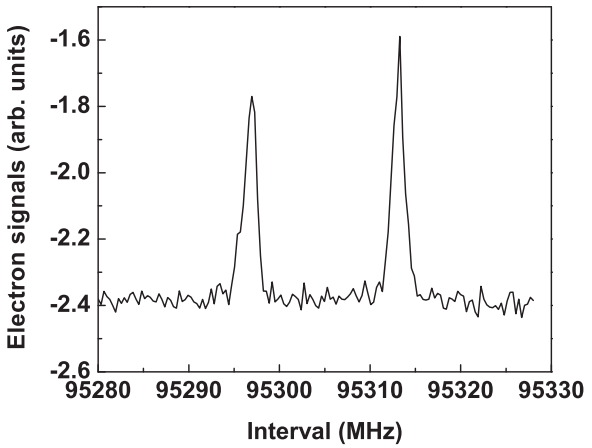

FIG. 4. Two-photon $4s18f \rightarrow 4s18h$ resonances. The two resonances are separated by the K splitting of the $4s18h$ state.

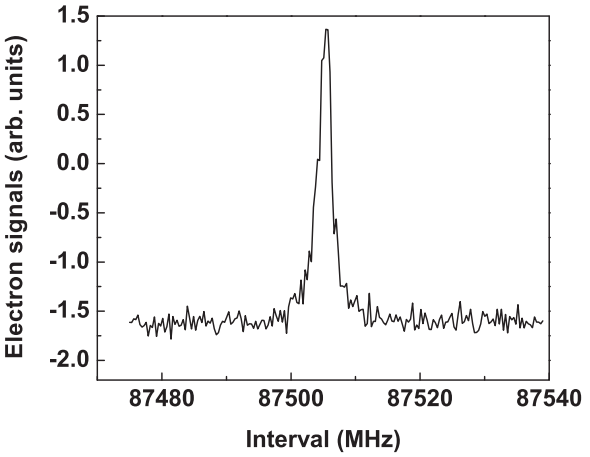

FIG. 5. Three-photon $4s19f \rightarrow 4s19i$ resonance at relative microwave power 0.63 and at relative rf power 1.0. The K splitting of the $4s19i$ states cannot be resolved due to the Earth's magnetic-field broadening.

B. Two-photon $4snf \rightarrow 4snh$ intervals

For the two-photon transition, $4snf \rightarrow 4snh$, we observed two resonant peaks for each n suggesting that the higher ℓ states, $\ell \geqslant 5$, are not singlets and triplets. The states are described by coupling the total angular momentum of the core $\vec{j}_c$ to the orbital angular momentum $\vec{\ell}$ of the Rydberg electron to form $\vec{K}$. Explicitly,

$$\vec{K} = \vec{j}_c + \vec{\ell}. \tag{1}$$

The splitting between the two K levels is due to the indirect spin orbit splitting [10,11]. We ignore the spin of the Rydberg electron. For the Ca $4sn\ell$ states, $j_c = 1/2$; therefore, $K = \ell \pm 1/2$. Hence, for each ℓ state we observe two transitions from the $4snf$ to the $4sn\ell$ states, corresponding to $K = \ell + 1/2$ and $K = \ell - 1/2$. To correct for the small ac Stark shift due to the microwave field, 1.8 MHz at the highest power we used, the resonances were observed at different microwave powers, and the resonance frequencies were extrapolated linearly to zero microwave power to obtain unshifted $4snf - 4snh$ intervals. Typical resonances for the two-photon transitions are shown in Fig. 4, and the observed intervals are given in Table II. The typical linewidth of the resonances is 2–3 MHz. The linewidth is due to the Earth's magnetic field since the $4snh$ states are no longer singlets and triplets.

C. Three-photon $4snf \rightarrow 4sni$ intervals

For the three-photon transitions, a single microwave field does not have enough power to drive the three-photon $4snf \rightarrow 4sni$ transitions. Therefore, the three-photon transitions were driven by using two microwave photons and one rf photon. The rf frequency of 3.5–5 GHz frequency was fixed near the $4snh - 4sni$ frequency, and the microwave frequency was swept. We verified that the observed resonances were indeed the $4snf \rightarrow 4sni$ transitions by varying the rf frequency within ±5 MHz and sweeping the microwave frequency for each rf frequency. For each rf frequency, the $4snf \rightarrow 4sni$ interval, given by twice the microwave frequency plus the rf frequency, was approximately constant, with only a slight difference in frequency due to the ac Stark shift. A typical three-photon resonance is shown in Fig. 5. In Fig. 5, we do not see the K splitting, because the K splitting in the $4sni$ states is not resolvable. Since most of the K splitting is from the dipole term, we can estimate the K splitting in the $4sni$ states using the adiabatic dipole term of Eqs. (37) and (38a) and ignoring the quadrupole term of Eq. (38b) of Ref. [10]. Explicitly,

$$K_{n\ell} = \frac{2(2\ell+1)\Delta_{4p}\langle r^{-6}\rangle_{n\ell}\langle 4s|r|4p\rangle^2}{9(W_{4s} - W_{4p})^3}, \tag{2}$$

where Δ_{4p} is the fine-structure splitting of the Ca^+ $4p$ state, $\langle r^{-6}\rangle_{n\ell}$ is the expectation value of $1/r^6$ of the $n\ell$ Rydberg state, $\langle 4s|r|4p\rangle$ is the Ca^+ radial matrix element, W_{4s} is the energy of the Ca^+ $4s$ state, and W_{4p} is the energy of the Ca^+ $4p$ state. Since we have measured the K splitting in the $4snh$ states, we can use Eq. (2) to estimate the K splitting in the $4sni$ states. The ratio between the K splitting in the $4sni$ and $4snh$ states is the ratio $\langle r^{-6}\rangle_{ni}/\langle r^{-6}\rangle_{nh} = 0.2$. Therefore, the K splitting in the $4sni$ states varies from 4 to 2 MHz as n increases from 18 to 23, which is not resolvable in our experiment due to the Earth's magnetic field.

In the three-photon transitions there are both rf and microwave power shifts. To eliminate the ac Stark shift from both fields, we observed the resonances at different rf and microwave powers. For a given microwave power, we observed resonances at different rf powers. We extrapolated the observed frequencies linearly to obtain the resonance frequency at zero

TABLE II. $nf - nh$ observed intervals and nh K splittings.

n	$K = 9/2$ (MHz)	$K = 11/2$ (MHz)	K splitting (MHz)
18	95296.36(6)	95312.53(9)	16.17(11)
19	81300.49(6)	81314.41(3)	13.92(7)
20	69905.16(18)	69917.62(13)	12.46(22)
21	60536.07(10)	60546.51(9)	10.44(13)
22	52761.38(96)	52770.12(12)	8.74(97)
23	46261.65(18)	46269.19(5)	7.54(19)

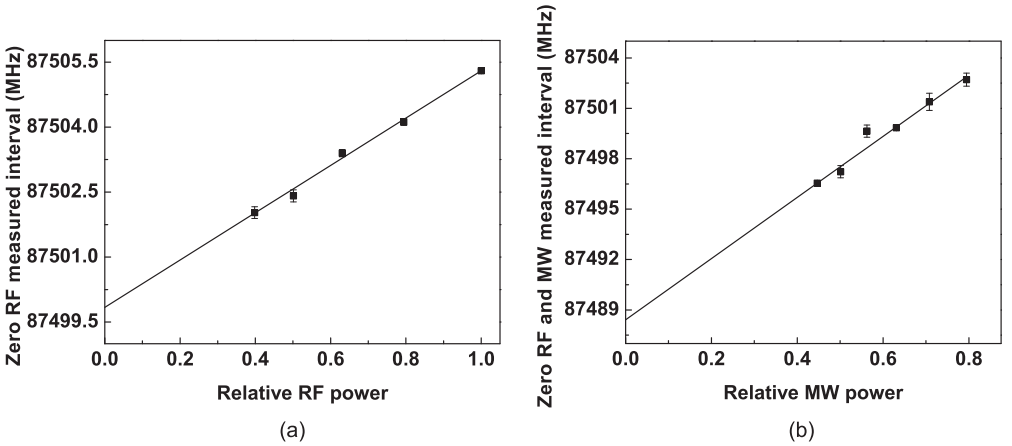

FIG. 6. Extrapolation of the three-photon $4s19f \rightarrow 4s19i$ transition to zero rf and microwave powers. (a) At relative microwave power 0.63, resonances were observed at different rf powers to obtain the resonance frequency at zero rf power. (b) Several zero rf power resonances were obtained at different microwave powers and extrapolated to zero rf and microwave powers.

rf power for a given microwave power. We repeated the same procedure for several microwave powers. The resonance frequencies at zero rf power of several microwave powers were extrapolated to obtain the resonance frequencies at zero rf and microwave powers. A typical resonance is shown in Fig. 6, typical power extrapolations are shown in Fig. 5, and the unshifted intervals are given in Table III.

D. Four-photon $4snf \rightarrow 4snk$ intervals

The $4snf \rightarrow 4snk$ four-photon transitions were excited using two microwave photons and two rf photons. The rf frequency was fixed near the $4snh \rightarrow 4snk$ resonance, while the microwave frequency was swept in the vicinity of the $4snf \rightarrow 4snh$ resonance. Similar to the three-photon excitation, we verified that the observed resonances were the $4snf \rightarrow 4snk$ transitions by varying the rf frequency within ± 5 MHz and sweeping the microwave frequency for each rf frequency. For each rf frequency, the $4snf \rightarrow 4snk$ interval was given by twice the microwave frequency plus twice the rf frequency and was approximately constant. We eliminated the ac Stark shifts using the process discussed for the three-photon transitions. Typical signals for four-photon transitions are shown in Fig. 7, and the unshifted intervals are given in Table IV. Using Eq. (2), we estimate the K splitting in the $4snk$ states to be on the order of 1 MHz for $18 \leqslant n \leqslant 20$, which cannot be resolved in this experiment.

TABLE III. $nf - ni$ observed intervals.

n	Observed frequency (MHz)
18	102558.95(54)
19	87488.41(40)
20	75223.05(15)
21	65141.32(78)
22	56766.61(69)
23	49771.37(26)

E. One-photon $4snf \rightarrow 4s(n+1)d$ intervals

We have observed the $4snf \rightarrow 4s(n+1)d$ transitions for $n = 19$, 20, and 21. In this region the $4snd\ ^1D_2$ Rydberg states are perturbed by their interaction with the $3d^2\ ^1D_2$ state [12]. The perturbation results in shorter lifetimes and rapidly changing quantum defects. For $19 \leqslant n \leqslant 21$ the $4snd\ ^1D_2$ states lie close enough in energy to the $4snf\ ^1F_3$ states that the $4snf \rightarrow 4s(n+1)d$ frequencies are within the microwave frequency range that we can generate. A typical resonance is shown in Fig. 8, and the observed intervals are presented in Table V.

IV. DATA ANALYSIS

We analyze the measured $\Delta\ell$ intervals using several variants of the core polarization model. First, we use the core polarization model as originally introduced by Mayer and Mayer [6]. In the high angular momentum $4sn\ell$ Rydberg states of $\ell > 4$, the Rydberg $n\ell$ electron is assumed to be in a hydrogenic $n\ell$ state which does not penetrate the Ca^+ core.

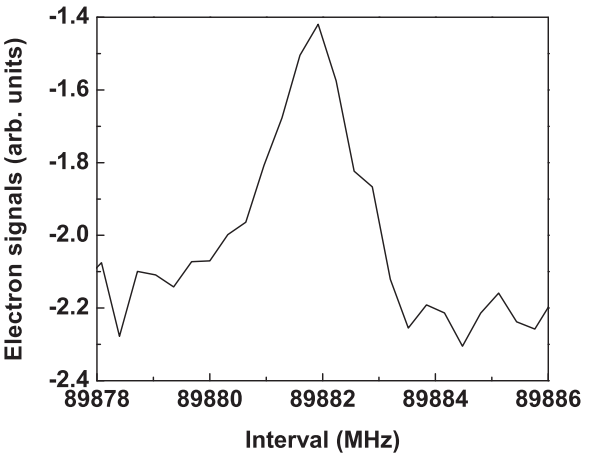

FIG. 7. Four-photon $4s19f \rightarrow 4s19k$ resonance at 0.178 relative microwave power and 0.794 relative rf power. The K splitting of the $4s19k$ states is on the order of 1 MHz and cannot be resolved.

TABLE IV. $nf - nk$ observed intervals.

n	Observed frequency (MHz)
18	105362.90(52)
19	89879.91(7)
20	77278.61(15)

TABLE V. $nf - (n+1)d$ observed intervals.

n	Observed frequency (MHz)
19	84377.04(4)
20	49143.13(12)
21	24542.36(4)

Furthermore, the Rydberg electron is assumed to move slowly compared to the electrons in the ionic core. Thus we term this model the adiabatic core polarization model. The presence of the Rydberg electron leads to a quasistatic electric field and gradient at the Ca^+ core, and, due to the dipole and quadrupole polarizabilities of the core, the energy levels of the Ca $4s n\ell$ states are depressed below the hydrogenic energy, $-1/2n^2$. The polarization energy shift is given by [6]

$$W_{\mathrm{pol},n\ell} = -\tfrac{1}{2}\alpha_d \langle r^{-4}\rangle_{n\ell} - \tfrac{1}{2}\alpha_q \langle r^{-6}\rangle_{n\ell}, \tag{3}$$

where α_d and α_q are the dipole and quadrupole polarizabilities of the Ca^+ $4s$ core, and $\langle r^{-4}\rangle_{n\ell}$ and $\langle r^{-6}\rangle_{n\ell}$ are the expectation values of the squares of the $n\ell$ Rydberg electron's field and field gradient at the core. Since the Rydberg electron is assumed to be in a hydrogenic state, analytic expressions exist for these expectation values. We can write Eq. (3) in Edlen's experimentally convenient form as [13]

$$W_{\mathrm{pol},n\ell} = -\alpha_d P_{n\ell} - \alpha_q P Q_{n\ell}, \tag{4}$$

where

$$P_{n\ell} = R_{\mathrm{Ca}} \langle r^{-4}\rangle_{n\ell} \tag{5}$$

and

$$Q_{n\ell} = \frac{\langle r^{-6}\rangle_{n\ell}}{\langle r^{-4}\rangle_{n\ell}}. \tag{6}$$

Here R_{Ca} is the Rydberg constant for Ca, $R_{\mathrm{Ca}} = 109\,735.81\ \mathrm{cm}^{-1}$. Since we measure the intervals between the $4sn\ell$ and $4sn(\ell+1)$, $\ell > 3$, states of the same n, we express the difference between the core polarization energies of $4sn\ell$ and $4sn(\ell+1)$ states of the same n as follows:

$$\frac{\Delta W_{\mathrm{pol},n\ell'\ell}}{\Delta P_{n\ell\ell'}} = \alpha_d + \alpha_q \frac{\Delta P Q_{n\ell\ell'}}{\Delta P_{n\ell\ell'}}, \tag{7}$$

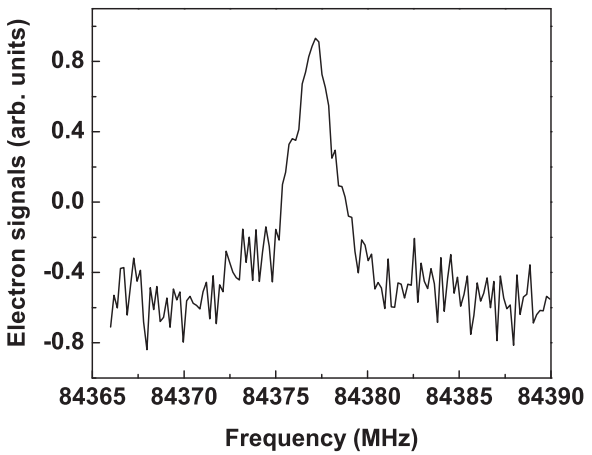

FIG. 8. One-photon $4s19f \rightarrow 4s20d$ resonance.

where $\Delta W_{\mathrm{pol},n\ell'\ell} = W_{\mathrm{pol},n\ell'} - W_{\mathrm{pol},n\ell}$, $\Delta P_{n\ell\ell'} = P_{n\ell} - P_{n\ell'}$, and $\Delta P Q_{n\ell\ell'} = P_{n\ell} Q_{n\ell} - P_{n\ell'} Q_{n\ell'}$. $\Delta P_{n\ell\ell'}$ and $\Delta P Q_{n\ell\ell'}$ are easily calculated, and $\Delta W_{\mathrm{pol},n\ell'\ell}$ is the measured $4sn\ell - 4sn\ell'$ interval. Figure 9 shows the graph of $\frac{\Delta W_{\mathrm{pol},n\ell'\ell}}{\Delta P_{n\ell\ell'}}$ versus $\frac{\Delta P Q_{n\ell\ell'}}{\Delta P_{n\ell\ell'}}$ using the measured $nh - ni$ (▲) and $ni - nk$ (■) intervals. For the $4snh$ states in which the $K = 9/2$ and $11/2$ states are resolved, we use the centers of gravity in our calculation. As suggested by Eq. (7), by plotting $\frac{\Delta W_{\mathrm{pol},n\ell'\ell}}{\Delta P_{n\ell\ell'}}$ versus $\frac{\Delta P Q_{n\ell\ell'}}{\Delta P_{n\ell\ell'}}$, the values of dipole and quadrupole polarizabilities can be extracted from the y intercept and slope of a line through the data points, as shown in Fig. 9. The resulting Ca^+ $4s$ dipole and quadrupole polarizabilities are $\alpha_d = 75.32(4)a_0^3$ and $\alpha_q = -257(8)a_0^5$, respectively. In this, its simplest form, the adiabatic core polarization model yields a negative quadrupole polarizability, which is impossible.

van Vleck and Whitelaw pointed out that the polarization energy shift of Eq. (3) is a limiting case of a second-order shift due to the higher multipole terms in the Coulomb interaction between the Rydberg $n\ell$ electron and the ion core [14]. For example, the dipole polarization energy of a Ca $4sn\ell$ state comes from the dipole coupling to $Npn'(\ell \pm 1)$ and $Np\epsilon(\ell \pm 1)$ bound and continuum states, as shown in Fig. 10. By considering only the two valence electrons we are implicitly ignoring inner-shell excited states of Ca, which amounts to ignoring the contribution of the Ca^{++} polarizability to the Ca^+ polarizability. The shift due to the higher lying $Npn'(\ell \pm 1)$ and $Np\epsilon(\ell \pm 1)$ states is readily calculated in second-order perturbation theory by summing over N and n', and integrating

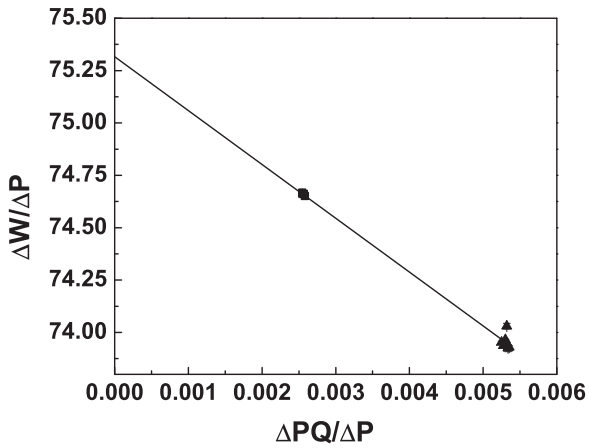

FIG. 9. Adiabatic plot of the measured $nh - ni$ (▲) and $ni - nk$ (■) intervals using Eq. (7). There are three data points for the $ni - nk$ (■) intervals, $18 \leqslant n \leqslant 20$, and six data points for the $nh - ni$ (▲) intervals, $18 \leqslant n \leqslant 23$. A fit to the straight line yields the y intercept and slope, which are α_d and α_q, respectively. The resulting fit values are $\alpha_d = 75.32(4)a_0^3$ and $\alpha_q = -257(8)a_0^5$.

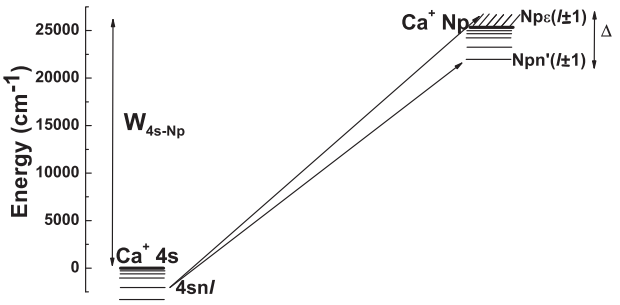

FIG. 10. Energy levels of the Rydberg states converging to the Ca^+ $4s$ and Np states and the continua associated with the latter. A $4sn\ell$ Rydberg state is dipole coupled to $Npn'(\ell \pm 1)$ states which span an energy range Δ. If $\Delta \ll W_{4s-Np}$ the adiabatic approximation is valid.

over ϵ. The sum over n' and the integral over ϵ span an energy range Δ, as shown by Fig. 10. If

$$\Delta \ll W_{4s-Np}, \tag{8}$$

for all N, the result of Mayer and Mayer is recovered. For example, the dipole polarization energy shift is given by the dipole term of Eq. (3). Equation (8) is a more precise statement of the adiabatic condition. For alkali-metal atoms, in which the excited states of the ion are all at high energies, the requirement of Eq. (8) is easily met, and the adiabatic approximation works well. For alkaline-earth atoms this requirement is not met, and the adiabatic approximation fails, as is evident in Fig. 9.

To correct for the nonadiabatic effects and extract the core polarizabilities from the $\Delta\ell$ intervals there are two approaches we can take. One is the adiabatic expansion method, which can be viewed as an expansion in powers of Δ/W_{4s-Np}. The attraction of this approach is that we are only calculating the corrections to the analytic shifts obtained using hydrogenic expectation values. The potential problem is convergence of the expansion. The alternative approach is the direct numerical calculation of the hydrogenic matrix elements for the dipole and quadrupole interactions, as exemplified in Fig. 10. This approach is in principle exact, but since the entire energy shift is calculated numerically, small errors are important.

In the adiabatic expansion approach the higher-order terms in the expansion appear as expectation values of higher inverse powers of r. If the expansion is to converge, these terms should become smaller with increasing order. While this condition is met for the high ℓ states, it is not for the $4snh$ states. In the nonadiabatic correction to the dipole polarization energy the $\langle r^{-8}\rangle_{n\ell}$ term is larger than the $\langle r^{-6}\rangle_{n\ell}$ term. In short, the expansion is nonconvergent, and we cannot use this method to analyze our data. However, using the leading correction term for the dipole polarization energy provides a bound for the polarizabilities. The leading term in the correction to the dipole polarization energy has a $\langle r^{-6}\rangle_{n\ell}$ dependence and is thus indistinguishable from the quadrupole polarization energy. With the inclusion of this term, Eq. (7) becomes

$$\frac{\Delta W_{\mathrm{pol},n\ell\ell'}}{\Delta P_{n\ell\ell'}} = \alpha_d + (\alpha_q - 6\beta_1)\frac{\Delta PQ_{n\ell\ell'}}{\Delta P_{n\ell\ell'}}, \tag{9}$$

where $\beta_1 \cong 0.95\alpha_d/(2W_{4p-4s})$ [15]. The numerical factor of 0.95 comes from the fact that 5% of α_d comes from higher-lying np states of Ca^+ and Ca^{++} [16]. We calculate $6\beta_1$ to be $1850(40)a_0^5$. Including the leading term in the adiabatic expansion simply raises the value of α_q by $6\beta_1$, yielding $\alpha_q = 1590(40)a_0^5$. The value of α_d is unchanged. Since the $6\beta_1$ correction term in Eq. (9) overcorrects for the nonadiabatic effect, these values are lower and upper bounds to α_d and α_q, respectively.

TABLE VI. k_d calculated values.

n	$\ell = 5$	$\ell = 6$	$\ell = 7$
18	0.956528	0.972293	0.982680
19	0.956518	0.972178	0.982543
20	0.956500	0.972111	0.982437
21	0.956437	0.972033	
22	0.956453	0.971906	
23	0.956423	0.971892	

The alternative approach is the direct calculation of the multipole interactions, as shown in Fig. 10 for the dipole interaction. As an approximation we assume that all the dipole and quadrupole polarization energies of the Ca $4sn\ell$ states come from the couplings to the Ca $4pn'\ell'$ and $3dn'\ell'$ states. For both the dipole and quadrupole shifts, we find the ratio of the explicitly calculated shift to that predicted by the adiabatic model. These ratios, the nonadiabatic factors k_d and k_q, are then used to correct the adiabatic model. Explicitly, we rewrite Eq. (3) as

$$W_{\mathrm{pol},n\ell} = -\tfrac{1}{2}k_d\alpha_d\langle r^{-4}\rangle_{n\ell} - \tfrac{1}{2}k_q\alpha_q\langle r^{-6}\rangle_{n\ell}. \tag{10}$$

The nonadiabatic factors k_d and k_q are defined in Eqs. (17.25) and (17.26) of Ref. [17]. Both are calculated numerically using a Numerov algorithm to calculate hydrogenic wave functions. The calculated values of k_d and k_q are given in Tables VI and VII, respectively. There are sum rules for the sums of the squares of the matrix elements [14], and using them we estimate the percentage uncertainties in k_d and k_q to be 0.3% for both values. As shown in Table VI, to three significant digits, there is no n dependence in k_d. As shown in Table VII, to four significant digits, there is n dependence in k_q for $\ell = 5$ and $\ell = 6$ but not for $\ell = 7$. We can express Eq. (10) in Edlen's form as follows:

$$W_{\mathrm{pol},n\ell} = -\alpha_d P'_{n\ell} - \alpha_q P' Q'_{n\ell}, \tag{11}$$

where

$$P'_{n\ell} = k_d P \tag{12}$$

TABLE VII. k_q calculated values.

n	$\ell = 5$	$\ell = 6$	$\ell = 7$
18	0.9780	0.9273	0.9376
19	0.9797	0.9277	0.9376
20	0.9812	0.9284	0.9376
21	0.9824	0.9284	
22	0.9835	0.9287	
23	0.9845	0.9292	

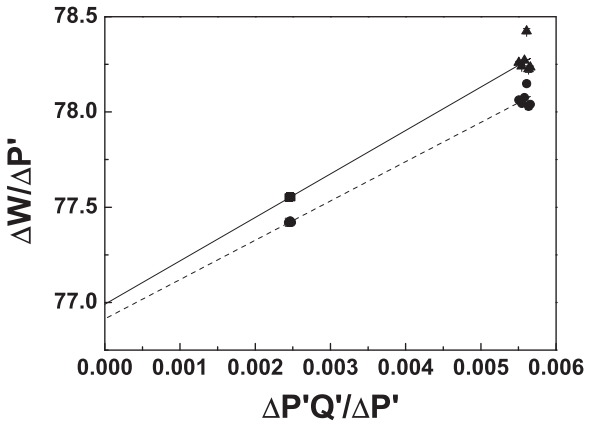

FIG. 11. Nonadiabatic plot of the measured $nh - ni$ (▲) and $ni - nk$ (■) intervals using Eq. (14). There are three data points for the $ni - nk$ (■) intervals, $18 \leqslant n \leqslant 20$, and six data points for the $nh - ni$ (▲) intervals, $18 \leqslant n \leqslant 23$. A linear fit (solid line) gives values for the y intercept and slope of $76.99(7)a_0^3$ and $228(12)a_0^5$, respectively. When we take into account the overcorrection of k_d, we obtain the data points (•) and the lower fit line (broken line), which leads to our final values of $\alpha_d = 76.91(5)a_0^3$ and $\alpha_q = 206(9)a_0^5$.

and

$$Q'_{n\ell} = \frac{k_q}{k_d} Q_{n\ell}. \tag{13}$$

Hence the difference between the core polarization energy of $4sn\ell$ and $4sn\ell'$ of the same n is

$$\frac{\Delta W_{\mathrm{pol},n\ell'\ell}}{\Delta P'_{n\ell\ell'}} = \alpha_d + \alpha_q \frac{\Delta P' Q'_{n\ell\ell'}}{\Delta P'_{n\ell\ell'}}, \tag{14}$$

where $\Delta W_{\mathrm{pol},n\ell'\ell}$ is defined in Eq. (7), $\Delta P'_{n\ell\ell'} = P'_{n\ell} - P'_{n\ell'}$, and $\Delta P' Q'_{n\ell\ell'} = P'_{n\ell} Q'_{n\ell} - P'_{n\ell'} Q'_{n\ell'}$.

We plot $\frac{\Delta W_{\mathrm{pol},n\ell'\ell}}{\Delta P'_{n\ell\ell'}}$ versus $\frac{\Delta P' Q'_{n\ell\ell'}}{\Delta P'_{n\ell\ell'}}$ in Fig. 11 using the $nh - ni$ (▲) and $ni - nk$ (■) measured intervals. From Fig. 11, the intercept and slope of the graph yield fit values of $\alpha_d = 76.99(7)a_0^3$ and $\alpha_q = 228(12)a_0^5$, respectively, shown by the solid line.

At this point it is useful to compare Figs. 9 and 11, in particular the points on the solid line in Fig. 11. There is almost no difference in the horizontal positions of the data points but a large difference in their vertical positions, leading to very different values for α_q. The difference in the vertical positions comes from substituting $\Delta P'$ for ΔP, i.e., introducing k_d, the nonadiabatic correction to the dipole polarization energy. The small difference in the horizontal positions of the points in the two graphs indicates that the introduction of k_q, the nonadiabatic correction for the quadrupole polarization energy, has a negligible effect for these $\Delta\ell$ intervals. The uncertainties in the fit in Fig. 11 do not reflect the uncertainty in the calculation of k_d. When it is taken into account the values we obtain are $\alpha_d = 77.0(3)a_0^3$ and $\alpha_q = 228(12)a_0^5$.

We now return to our assumption that the polarization shifts are due entirely to the couplings to the $4pn'\ell'$ and $3dn'\ell'$ states. This assumption is equivalent to assuming the Ca^+ polarizabilities arise entirely from the Ca^+ $4p$ and $3d$ states. The calculations of Safronova and Safronova indicate that 95% of α_d is due to the $4p$ state, and 58% of α_q is due to the $3d$ state [16]. Thus in k_d and k_q we have overcorrected. Inspecting Figs. 9 and 11 we can see that the overcorrection due to k_q is insignificant, but that due to k_d is important. Accordingly, we have reduced the correction due to k_d by 5%, resulting in the broken line in Fig. 11. This modification leads to the values $\alpha_d = 76.91(5)a_0^3$ and $\alpha_q = 206(9)a_0^5$. When the uncertainty in the calculation of k_d is taken into account the values we obtain are $\alpha_d = 76.9(3)a_0^3$ and $\alpha_q = 206(9)a_0^5$. As we shall discuss shortly, we believe these values to be upper and lower bounds to α_d and α_q.

TABLE VIII. Ca^+ $4s$ dipole polarizability (α_d) obtained from this work and other theoretical and experimental results.

	α_d (a_0^3)
This work$_{ae}$	75.32(4)
This work$_{dc}$	76.9(3)
Expt. [8]	87(2)
Expt. [18]	75.3(4)
Expt. [19]	70.89(15)
Theory [16]	76.1(5)
Theory [21]	73.0(1.5)
Theory [20]	75.49

V. DISCUSSION

Tables VIII and IX show values of α_d and α_q from this work and other experimental and theoretical work. The uncertainties for our values represent the uncertainties from the fits of the data to the two models. The values labeled $_{ae}$ are from the adiabatic expansion method, Eq. (9), and the values labeled $_{dc}$ are from the direct calculation method, Eq. (14). There are three experimental results for α_d to which we can compare ours. The value of Ref. [8] is based on the measurement of the $4snf \rightarrow 4sng$ intervals. The analysis of these data relied heavily on a more complex theoretical model, which was probably inadequate to represent the $4sng$ states. The value of α_d given in Ref. [18] was obtained by assuming that the $4snh$ quantum defects arise solely from the dipole polarizability and applying the adiabatic core polarization model. Since the quadrupole polarizability is small and the nonadiabatic effect on the dipole polarization cancels its effect to some extent, this approach yields a value for α_d close to the value we obtained from Fig. 9. In Ref. [19] lifetime measurements of the Ca^+ $4p_j$ states were used to obtain the oscillator strengths of the $4s - 4p_j$ transitions, taking into account the small branching ratios for decay to the $3d_j$ states. The oscillator strengths of the $4s - 4p_j$ transitions were then used to calculate the value

TABLE IX. Ca^+ $4s$ quadrupole polarizability (α_q) obtained from this work and other theoretical results.

	α_q (a_0^5)
This work$_{ae}$	1590(40)
This work$_{dc}$	206(9)
Theory [16]	871(4)
Theory [20]	875.1

of α_d. The resulting value of α_d is too small due to the neglect of higher-lying Ca^+ Np states and the dipole polarizability of Ca^{++}, but when this omission is taken into account it is consistent with our value for α_d. The theoretical values for α_d from Refs. [16] and [20] fall within our experimental bounds given in Eq. (15), while the theoretical value of Ref. [21] is clearly outside the bounds.

As shown in Table IX, our value for α_q obtained by the adiabatic expansion method is twice the theoretical value, and the value obtained by the direct calculation method is a factor of 4 smaller than the theoretical value. Since a large fraction, two-thirds, of the quadrupole polarizability is due to the Ca^+ $3d$ states, an alternative check of the calculated quadrupole polarizability is the lifetime of the Ca^+ $3d$ state, which decays by quadrupole radiation. The measured lifetime is in good agreement with the calculated lifetime, supporting the validity of the calculation of α_q. It is worth noting that if the value of k_d for the $4snh$ states is reduced to 98.35% of the current k_d value we would obtain $\alpha_d = 75.3(1)a_0^3$ and $\alpha_q = 878(15)a_0^5$, in excellent agreement with the recent theoretical values. In view of the sensitivity of the direct calculation approach to the numerical calculations of k_d and the large discrepancy between our value of α_q and the theoretical values, we view the direct calculation values of Tables VIII and IX as upper and lower bounds for α_d and α_q, respectively. As a consequence, we report bounds for α_d and α_q. Explicitly,

$$75.3a_0^3 < \alpha_d < 76.9a_0^3 \tag{15}$$

and

$$206a_0^5 < \alpha_q < 1590a_0^5. \tag{16}$$

Our ability to specify α_d and α_q is limited by our confidence in the core polarization models. Two experimental avenues can be explored to minimize this problem. The first is measuring higher ℓ intervals in which the nonadiabatic corrections are not as large, as done by Lundeen *et al.* for other atoms [22]. The second is high-resolution laser spectroscopy of the Ca $4snd$ $^1D_2$ states. Absolute measurements of their energies, good to 10 MHz, would locate the $4snd$ levels relative to the hydrogenic $n\ell$ levels. The microwave measurements reported here could then be used to locate the Ca $4sn\ell$ levels relative to the H $n\ell$ levels, and the present data could then be analyzed in terms of the displacements of the energies from the hydrogenic levels, instead of the differences in the displacements. The $4snh$ states could be dropped from the analysis, substantially reducing the uncertainty due to the nonadiabatic corrections.

Making measurements involving higher ℓ states should minimize the nonadiabatic effects, allowing a better determination of the polarizabilities. However, it is not obvious that the discrepancy between the theoretical and experimental values will disappear. Intervals between the high ℓ Ba $6sn\ell$ levels have been measured, but the value of α_q extracted by the direct calculation method is a factor of 2 smaller than the theoretical value, a similar discrepancy to that reported here for Ca [23]. Determining the source of these discrepancies is a worthy theoretical challenge.

VI. CONCLUSION

We have measured $\Delta\ell$ intervals of Ca $4snf \rightarrow 4sn\ell$, $18 \leqslant n \leqslant 23$, and $4 \leqslant \ell \leqslant 7$ using a microwave and rf resonance approach. We have used these measurements to place bounds on the Ca^+ dipole and quadrupole polarizabilities. The Ca^+ $4s$ dipole and quadrupole polarizabilities are $75.3a_0^3 < \alpha_d < 76.9a_0^3$ and $206a_0^5 < \alpha_q < 1590a_0^5$. The Ca^+ $4s$ dipole polarizability agrees well with recent theoretical values. However, we are not able to place tight bounds on the Ca^+ $4s$ quadrupole polarizability due to uncertainties in the core polarization analyses. We hope this work will motivate theoretical work to reexamine the problem of core polarization analysis and, more generally, the source of the discrepancy between the experimental and theoretical values of α_q.

ACKNOWLEDGMENTS

This work has been supported by the U.S. Department of Energy, Office of Basic Energy Sciences. J.N. would like to thank DPST Research Grant No. 030/2557, Thailand Research Fund (TRF) Grant No. MRG5680117, and CMU Junior Research Fellowship Program for their supports. It is a pleasure to acknowledge F. S. Niyaz for assistance in the measurements, M. Safronova for pointing out the paucity of measurements for Ca, and S. R. Lundeen for many insightful discussions.

[1] R. J. Hendricks, J. L. Sorensen, C. Champenois, M. Knoop, and M. Drewsen, Phys. Rev. A **77**, 021401(R) (2008).
[2] M. Kajita, Y. Li, K. Matsubara, K. Hayasaka, and M. Hosokawa, Phys. Rev. A **72**, 043404 (2005).
[3] M. Chwalla, J. Benhelm, K. Kim, G. Kirchmair, T. Monz, M. Riebe, P. Schindler, A. S. Villar, W. Hänsel, C. F. Roos, R. Blatt, M. Abgrall, G. Santarelli, G. D. Rovera, and Ph. Laurent, Phys. Rev. Lett. **102**, 023002 (2009).
[4] B. Arora, M. S. Safronova, and C. W. Clark, Phys. Rev. A **76**, 064501 (2007).
[5] T. F. Gallagher and W. E. Cooke, Phys. Rev. Lett. **42**, 835 (1979).
[6] J. E. Mayer and M. G. Mayer, Phys. Rev. **43**, 605 (1933).
[7] U. I. Safronova and M. S. Safronova, Phys. Rev. A **79**, 022512 (2009).
[8] A. G. Vaidyanathan, W. P. Spencer, J. R. Rubbmark, H. Kuiper, C. Fabre, D. Kleppner, and T. W. Ducas, Phys. Rev. A **26**, 3346 (1982).
[9] E. S. Shuman, J. Nunkaew, and T. F. Gallagher, Phys. Rev. A **75**, 044501 (2007).
[10] E. S. Shuman and T. F. Gallagher, Phys. Rev. A **74**, 022502 (2006).
[11] E. L. Snow, R. A. Komara, M. A. Gearba, and S. R. Lundeen, Phys. Rev. A **68**, 022510 (2003).
[12] T. R. Gentile, B. J. Hughey, D. Kleppner, and T. W. Ducas, Phys. Rev. A **42**, 440 (1990).

[13] B. Edlen, *Handbuch der Physik* (Springer, Berlin, 1964).
[14] J. H. Van Vleck and N. G. Whitelaw, Phys. Rev. **44**, 551 (1933).
[15] E. L. Snow and S. R. Lundeen, Phys. Rev. A **76**, 052505 (2007).
[16] M. S. Safronova and U. I. Safronova, Phys. Rev. A **83**, 012503 (2011).
[17] T. F. Gallagher, *Rydberg Atoms* (Cambridge University Press, Cambridge, England, 1994).
[18] E. S. Chang, J. Phys. B **16**, L539 (1983).
[19] C. E. Theodosiou, L. J. Curtis, and C. A. Nicolaides, Phys. Rev. A **52**, 3677 (1995).
[20] J. Mitroy and J. Y. Zhang, Eur. Phys. J. D **46**, 415 (2008).
[21] B. K. Sahoo, B. P. Das, and D. Mukherjee, Phys. Rev. A **79**, 052511 (2009).
[22] S. R. Lundeen, in *Advances in Atomic, Molecular, and Optical Physics*, edited by P. R. Berman and C. C. Lin (Academic Press, New York, 2005), Vol. 52.
[23] E. G. Kim, J. Nunkaew, and T. F. Gallagher, Phys. Rev. A **89**, 062503 (2014).